

# **Photon energy provision for shape memory induced self-healing polymers**

Von der Fakultät für Mathematik, Informatik und Naturwissenschaften der RWTH Aachen University zur Erlangung des akademischen Grades einer Doktorin der Naturwissenschaften genehmigte Dissertation

vorgelegt von

**M.Sc. Elizaveta Selezneva**

aus

*Orekhovo-Zuevo, Russische Föderation*

Berichter:

Universitätsprofessor Dr. rer. nat. Martin Möller  
Universitätsprofessor Dr. rer. nat. Walter Richtering

Tag der mündlichen Prüfung: *09.10.2024*



*„Природа весьма проста; что этому противоречит, должно быть отвергнуто.“*

*Mikhail Vasilyevich Lomonosov  
(polymath, scientist and writer)*

---

The herein presented work was carried out at the DWI – Leibniz Institute for Interactive Materials e.V. and the RWTH Aachen University from June 2019 until May 2022 under the supervision of Prof. Dr. Martin Möller.

Chapters and extracts of this work have been or will be published in the following articles:

**Selezneva E.V.**, Bakirov A.V., Sedush N.G., Bystrova A.V., Chvalun S.N., Demco D., Möller M., How Shape Memory Effects can Contribute to Improved Self-Healing Properties in Polymer Materials, *Macromolecules* **2021**, 54, 5, 2506–2517

**Selezneva E.V.**, Rahimi K., Rieder S., Spatz J., Möller M., Composite Material and Shielding Against Electromagnetic Radiation, U.S. Patent Application 20230292480, filed May 28, 2021, published September 14, 2023.

**Selezneva E. V.**, Graf R., Bakirov A. V., Demco D. E., Chvalun S. N., Moeller M. Structure and Dynamics of Poly(Ethylene-Co Methacrylic Acid) Ionomer Blends with Rubbery EPDM. *Macromol. Rapid Commun.* **2023**, *Submitted*.

S. Schweizerhof, **E. Selezneva**, I. Georgius, M. Maaßen, M. v. Dongen, A. Mourran, A. Pich, M. Möller, “How to transcribe the enigma of the Lycurgus Cup to polymer films to earmark products against forgery”, **2023**, *in preparation*.

**Selezneva E.V.**, Bakirov A.V., Sedush N.G., Chvalun S.N., Demco D., Möller M., How Shape Memory Effects can Contribute to Improved Self-Healing Properties in Polymer Materials, *IUPAC-MACRO2020+ The 48th World Polymer Congress* May 16-20, **2021** Jeju, Korea

---

# EIDESSTATTLICHE ERKLÄRUNG

**Elizaveta Selezneva** erklärt hiermit, dass diese Dissertation und die darin dargelegten Inhalte die eigenen sind und selbstständig, als Ergebnis der eigenen originären Forschung, generiert wurden.

Hiermit erkläre ich an Eides statt

1. Diese Arbeit wurde vollständig oder größtenteils in der Phase als Doktorand dieser Fakultät und Universität angefertigt;
2. Sofern irgendein Bestandteil dieser Dissertation zuvor für einen akademischen Abschluss oder eine andere Qualifikation an dieser oder einer anderen Institution verwendet wurde, wurde dies klar angezeigt;
3. Wenn immer andere eigene- oder Veröffentlichungen Dritter herangezogen wurden, wurden diese klar benannt;
4. Wenn aus anderen eigenen- oder Veröffentlichungen Dritter zitiert wurde, wurde stets die Quelle hierfür angegeben. Diese Dissertation ist vollständig meine eigene Arbeit, mit der Ausnahme solcher Zitate;
5. Alle wesentlichen Quellen von Unterstützung wurden benannt;
6. Wenn immer ein Teil dieser Dissertation auf der Zusammenarbeit mit anderen basiert, wurde von mir klar gekennzeichnet, was von anderen und was von mir selbst erarbeitet wurde;
7. Ein Teil oder Teile dieser Arbeit wurden zuvor veröffentlicht und zwar in:
  - Selezneva E.V. et al., *Macromolecules* 54, 2506–2517 (2021).
  - Selezneva E.V. et al., U.S. Patent Application US 20230292480 (2023).
  - Selezneva E.V. et al., IUPAC-MACRO 2020+, Jeju, Korea (2021).

Datum:

Unterschrift:

---

# ABSTRACT

This research focuses on self-healing polymer materials, addressing challenges, such as large-scale defect repair. We introduce ionomer–rubber blends, featuring three types of cross-links: covalent links within a rubber network, ionic group clusters, and crystalline domains in the ionomer.

Self-healing relies on two structural memory types tied to deformation and defect-induced stresses. After damage macroscopic shape memory effects come into play, mending larger-scale fractures with annealing at elevated temperatures. At the same time reorganization of ionic clusters facilitates microscopic healing of defects ranging from millimeters to centimeters.

The study also explores the production and photothermal healing of hybrid films, using a self-healing rubber-ionomer blend with plasmonic nanoparticles. Through co-precipitation and hot pressing, we create versatile optical imprint composite materials. Effective plasmonic filler concentrations are established, enabling rapid photothermal repair of scratches and damages while preserving the sample's shape. Self-healing ionomer and metal fiber composites were prepared through various methods, evaluating percolation thresholds and corrosion resistance. We achieve homogeneous fiber distribution, confirm self-healing through induction heating, and leverage metal fibers magnetic properties.

Described materials can repair damage at both small and large scales, demonstrating the potential for enhancing the durability of composite materials in various applications. Additionally, the study explores the use of plasmonic nanoparticles and fiber fillers for non-invasive heating, which can further trigger the self-healing process and broaden the scope of potential applications in areas such as electronic equipment shielding and stealth technology.

---

**Keywords:** self-healing polymers; shape-memory effect; ionomer–rubber blends; plasmonic nanoparticles; photothermal healing.

---

# ZUSAMMENFASSUNG

Diese Arbeit befasst sich mit selbstheilenden Polymerwerkstoffen und adressiert dabei insbesondere die Herausforderung der Reparatur großflächiger Defekte. Dafür werden Ionomer-Kautschuk-Blends entwickelt, die drei Arten von Vernetzungen vereinen: kovalente Bindungen im Kautschuknetzwerk, ionische Cluster sowie kristalline Domänen im Ionomer.

Die Selbstheilung beruht auf zwei Strukturereinerungen, die mit durch Verformung bzw. durch Defekte induzierten Spannungen verknüpft sind. Nach einer Beschädigung greifen makroskopische Formgedächtniseffekte ein, die durch Tempern bei erhöhten Temperaturen größere Risse schließen. Gleichzeitig ermöglicht die Reorganisation der ionischen Cluster eine mikroskopische Heilung von Defekten im Millimeter- bis Zentimeterbereich.

Darüber hinaus werden Hybridfilme untersucht, die durch Einbettung plasmonischer Nanopartikel in das selbstheilende Kautschuk-Ionomer-Blend entstehen. Mittels Ko-Fällung und Heißpressen werden vielseitig optisch strukturierbare Verbundmaterialien hergestellt. Optimierte Füllstoffkonzentrationen erlauben eine schnelle photothermische Reparatur von Kratzern und Beschädigungen, ohne die Form des Bauteils zu verändern. Ferner werden selbstheilende Ionomer-Komposite mit Metallfasern über verschiedene Herstellungsrouten entwickelt; deren Perkolationsschwellen und Korrosionsbeständigkeit werden bestimmt. Eine homogene Faserverteilung, die Bestätigung der Selbstheilung durch Induktionserwärmung sowie die Nutzung der magnetischen Eigenschaften der Fasern werden gezeigt.

Die beschriebenen Materialien können Schäden sowohl im Mikro- als auch im Makrobereich reparieren und demonstrieren damit ihr Potenzial zur Lebensdauerverlängerung von Verbundwerkstoffen in vielfältigen

---

Anwendungen. Zudem eröffnet der Einsatz plasmonischer Nanopartikel und Faserfüllstoffe einen nicht-invasiven Erhitzungsweg, der den Selbstheilungsprozess auslösen kann und Anwendungsfelder wie Abschirmung elektronischer Geräte oder Stealth-Technologien erweitert.

**Schlagwörter:** selbstheilende Polymere; Formgedächtniseffekt; Ionomer-Kautschuk-Blends; plasmonische Nanopartikel; photothermische Heilung.

---

# Table of Contents

<b>EIDESSTATTLICHE ERKLÄRUNG</b> .....	<b>4</b>
<b>ABSTRACT</b> .....	<b>5</b>
<b>ZUSAMMENFASSUNG</b> .....	<b>7</b>
<b>LIST OF ABBREVIATIONS</b> .....	<b>13</b>
<b>1. INTRODUCTION</b> .....	<b>15</b>
1.1. Motivation .....	15
1.2. Scope of the thesis.....	19
1.3. References .....	20
<b>2. LITERATURE OVERVIEW</b> .....	<b>21</b>
2.1. Self-healing materials.....	21
2.1.1. Classification, physical and chemical aspects of self-healing .....	23
2.1.2. Supramolecular non-covalent interaction-based self-healing .....	27
2.1.3 Combination of self-healing properties with shape memory .....	32
2.2. Plasmonic nanoparticles .....	38
2.2.1. Production of plasmonic nanoparticles .....	39
2.2.2. Plasmon resonance .....	43
2.2.3. Application of plasmonic nanoparticles.....	45

---

2.3 Polymer based fibre composites.....	46
2.3.1. Mechanism of polymer-based EMI shielding materials with three-dimensional conductive networks .....	47
2.3.2. Internal heating in polymer-based Metal fibres composites .....	50
2.4. References .....	53
<b>3. TRIPLE NETWORK SYSTEMS FROM COMMERCIALY AVAILABLE POLYMERS .....</b>	<b>58</b>
3.1. Introduction .....	58
3.2. Results and discussion.....	62
3.2.1. Obtaining of multicomponent materials capable of multiscale damage healing .....	62
3.2.2. Investigation of the obtained samples by different physical methods .....	65
3.2.3. Assessment of the efficiency of the self-healing processes in the obtained specimens.....	80
3.3. Conclusions .....	86
3.4. Supporting information .....	88
3.5. Acknowledgements .....	94
3.6. References .....	95
<b>4. SELF-HEALING COMPOSITE MATERIALS WITH PLASMONIC NANOPARTICLES .....</b>	<b>96</b>

---

4.1. Introduction .....	96
4.2. Results and discussion.....	99
4.2.1 Synthesis of functional plasmonic nanoparticles and their stabilization .....	99
4.2.2 Study of methods of introducing plasmonic nanoparticles into polymer matrices. Determination of effective concentrations and modes of external exposure.....	100
4.2.3 Investigation of the healing process of polymer composites with plasmonic nanoparticles .....	111
4.3. Conclusions .....	118
4.4. Supporting information .....	119
4.5. Acknowledgements .....	127
4.6. References .....	128
<b>5. METAL FIBRE-FILLED COMPOSITE MATERIALS.....</b>	<b>130</b>
5.1. Introduction .....	130
5.2. Results and discussion.....	136
5.2.1. composite materials based on polymer matrices and fibre fillers of different chemical nature.....	136
5.2.2. Determination of effective concentrations and properties of the obtained samples .....	140

---

5.2.3 Internal heating of polymer composites containing metal fibres and their self-healing properties.....	146
5.3. Conclusions .....	151
5.4. Supporting information .....	152
5.5. Acknowledgements .....	156
5.6. References .....	157
<b>CONCLUSIONS.....</b>	<b>158</b>
<b>ACKNOWLEDGEMENTS.....</b>	<b>159</b>
<b>RESUME .....</b>	<b>160</b>

---

## LIST OF ABBREVIATIONS

IR - infrared

AuNR – gold nanorods

AuNPs - gold nanoparticles

LaB6 - lanthanum hexaboride

Tg – glass transition temperature

Tm – melting temperature

MWCNTs - multi-wall carbon nanotubes

CFs - carbonfibres

PEMAA - poly(ethylene-co-methacrylic acid)

ATRP - addition-fragmentation chain transfer-free radical polymerization

PDMAEA - poly(2-(dimethylamino)ethyl acrylate)

PCEA - poly(2-carboxyethylacrylate)

XSBR - carboxylated styrene–butadiene rubber

SMP - shape memory polymer

SME - shape memory effect

SMASH - shape memory assisted self-healing

PCL - poly( $\epsilon$ -caprolactone)

UV light - ultraviolet light

PL - Polylactide

POSS - polysilsesquioxane

PU - polyurethane

NPs - nanoparticles

CTAB - cetyltrimethylammonium bromide

EG - ethylene glycol

SPR - surface plasmon resonance

LSPR - longitudinal surface plasmon resonance

TSPR - transverse surface plasmon resonance

---

NIR – near infrared  
FRC - fibre-reinforced composites  
MF - metal fibres  
EMI - electromagnetic interference  
SE - shielding effectiveness"  
Ag NWs - Silver nanowires  
SBS - styrene-butadiene-styrene block copolymer  
DC - direct current  
EPDM - ethylene propylene diene monomer rubber  
PE - polyethylene  
DCP - dicumylperoxid  
MAS - Magic-Angle-Spinning  
NMR - Nuclear Magnetic Resonance  
DSC - Differential Scanning Calorimetry  
SAXS - Small Angle X-Ray Scattering  
WAXS - Wide Angle X-Ray Scattering  
LSPR - localized surface plasmon resonance  
PEG - polyethylene glycol  
MP - milling produced  
PP - plasma produced  
DCM - dichloromethane  
TEM - Transmission electron microscopy  
SEM - Scanning electron microscopy  
PSU - polysulfon  
LED - Light Emitting Diode  
UV-Vis - UltraViolet-Visible Spectroscopy  
SEBS - Styrene-Ethylene-Butadiene-Styrene  
micro CT - Microcomputed tomography

---

# 1. INTRODUCTION

## 1.1. Motivation

Although inspired by healing processes in living organisms, self-healing polymer materials are distinguished by the fact that the healing must be generated by the material itself. In living systems, healing is typically affected by genetically programmed actions, directed mass transport and metabolic conversions. Compared to such systems, concepts for self-healing polymers focus entirely on the components of the material, their respective properties, and structural composition. Within this context it is helpful to recall two fundamental aspects of a healing process: (i) it must selectively restore the original state, and (ii) it will need an energy input, just like the damage has been generated by an energy driven impact. The first point refers to the confusion between the terms self-healing and gluing. In the case of gluing there is no internal memory of the damage inside of the material and adhesion occurs between every surface including nondamaged ones. In case of self-healing, the defect remembers that it was caused by damage and only the fresh surfaces created by the cut are activated for adhesion with each other. This effect was demonstrated in the work of Leibler.<sup>1</sup> New surfaces are generated when a sample of their rubber was cut in two pieces. Damage is transforming the new surfaces, created by the cut, into a metastable state of energy. The excess energy is released when the surfaces are rejoined, or when slow relaxation processes take place. Remarkably, the relaxation (maximum waiting time for mending) was reported to be more than one week at ambient temperature, while the healing time to recover the original cohesion was less than two hours. Hence, the distinction between gluing and healing has been based on two relaxation paths diverging in their characteristic times: energy relaxation by healing and energy relaxation by ageing of the newly generated surfaces. We may call this a memory effect, as the defect, which caused new surface to be created, remembers that it was generated by damage.

---

This consideration sheds a particular light on the fact that many authors distinguish between autonomous and non-autonomous self-healing mechanisms. In *autonomous* self-healing systems the impulse to start any restoration processes is in the damage itself, and the material is able to partially or fully restore its original characteristics without any additional external influence.<sup>2,3</sup> The fracturing caused change in the internal energy is sufficient for healing. *Non-autonomous* self-healing mechanisms require external initiation, such as elevated temperature<sup>4</sup>, light<sup>5,6</sup>, pH changes<sup>7</sup>, or other stimuli.<sup>8</sup> In non-autonomous self-healing, the healing can be promoted by energy introduced from the outside and a slow relaxation process can be accelerated at the same time, e.g., by interdiffusion of polymer chains. While in the first case, the discrimination between gluing or welding and self-healing is obvious, the second case will require some defect-focused selectivity of the energy harvesting process, e.g., if an encapsulated chemical reactant is only released or activated at the place of the fracture.<sup>9</sup>

The discussion that self-healing of a material requires a defect localized input of energy, e.g. by structural relaxation, raises the question how to affect and optimize this energy input. Two important aspects can be identified (i) the defect caused stresses and the corresponding raise in energy might not be sufficient to cause healing; (ii) non-healing relaxation paths must be omitted. The second point requires that relaxation should take place only at the moment when healing is possible, i.e., at contact and at conditions that favour healing. This leads us to the concept of activated healing, where an energy input from outside is employed at the appropriate time and conditions and in order to improve the driving energy for healing. The examples where chemical reactants are released by the defect causing event, e.g. breakage of capsules, uses harvesting of chemical energy at the moment when the defect is generated. Although this might not be the very best moment, it has the important advantage that the action is localized to the defect.

---

This thesis focuses on energy harvesting processes that are based on electromagnetic irradiation that allows to heat the material from inside. For self-healing, this internal heating must get linked to defect localized stress relaxation. Otherwise, the heating would either be inefficient or change the material as a whole.

One way to harvest energy for the purpose of internal heating addressed in this thesis uses the incorporation of plasmonic nanoparticles. These plasmonic particles convert IR-radiation to heat. Another way is based on the incorporation of microscopic  $\mu$ -metal fibres that can convert microwaves to heat and inductive heating at lower frequencies. Nanoparticles can effectively convert IR-light energy into heat due to surface plasmon resonance, achieved by coupling of the electromagnetic waves with electron charge oscillations of the metal conduction band electrons.<sup>10</sup> Within the metal fibres, eddy currents caused by the alternating magnetic field and corresponding hysteretic losses lead to an effective heat generation.<sup>11</sup>

Another important aspect for self-healing materials concerns the macroscopic shape recovery. Ideally, this should not be affected by handling, e.g. by pressing the cut parts together, but by autonomous contraction. This demands shape memory abilities. Classically, a shape memory material is programmed to undergo a shape transformation from state A to state B where both are not damaged. For polymer materials this can be achieved by double networks, which combine covalent and noncovalent thermoreversible crosslinks.<sup>12</sup> When such a double network material is strained and arrested in this strained state by the noncovalent crosslinks, the covalent network will store elastic energy. For a shape memory assisted self-healing, materials with stored elastic energy may be helpful to promote autonomous self-healing.<sup>13,14</sup>

---

Shape memory actions can span distances up to centimetres or even more, while the healing action that causes reconstitution of a cohesive conjunction concerns molecular interdiffusion, i.e. length scales in the nanometre regime. Structural relaxation is a common driving force in both cases. Taking into account that the relaxation is controlled by temperature and should take place only at the moment when healing is possible, temperature activation presents a key for the development of advanced self-healing materials that combine shape recovery and cohesive healing in a controlled way.

Based on these considerations this thesis deals with three questions:

- a) the design of a material that combines shape recovery with cohesive healing
- b) the design of materials that heat up from inside, when exposed to electromagnetic radiation
- c) the design of a material in which all three effects can be consolidated to yield advanced self-healing properties, where an energy input from outside is employed at the appropriate time and conditions in order to improve the driving energy for healing.

---

## 1.2. Scope of the thesis

**Chapter 2** comprises the state of art literature on self-healing materials with focus on the intrinsic self-healing mechanism, supramolecular noncovalent interaction based self-healing systems, including hydrogen bonding or ionic interaction, and shape memory assisted self-healing materials. Furthermore, optical and photothermal properties of gold nanorods (AuNRs), lanthanum hexaboride nanoparticles ( $\text{LaB}_6$ ) and their applications, in particular the use as photothermally-active components in composite materials. In addition, metal fibre composite preparation and application are investigated, including electromagnetic shielding and induction heating.

**Chapter 3** deals with realization of the triple network self-healing materials from a combination of commercially available polymers, namely a commercial ionomer and a copolymer of ethylene and propylene containing ethylidene norbornene for radical crosslinking.

In **Chapter 4**, functional plasmonic nanoparticles were synthesised. Their introduction into polymer compositions with a self-healing effect, as well as determination of the effective concentrations and modes of external exposure have been performed. Additionally, study of the kinetics of the healing process was conducted.

In **Chapter 5** composite materials based on polymer matrices and fibre fillers of various chemical nature were prepared. Comparative studies of the properties of the obtained compositions have been conducted and assessment of the kinetics of their healing under the influence of induction heating were explored.

---

### 1.3. References

- [1] Cordier, P., Tournilhac, F., Soulié-Ziakovic, C. & Leibler, L. *Nature* 451, 977–980 **2008**.
- [2] Li, C. H., Wang, C., Keplinger, C., *et al.* *Nat. Chem.* 8, 618–624 **2016**.
- [3] D’Elia, E., Eslava, S., Miranda, M., Georgiou, T. K. & Saiz, E. *Sci. Rep.* 6, 1–11 **2016**.
- [4] Huang, L., Jiang, R., Wu, J., *et al.* *Adv. Mater.* 29, 1–6 **2017**.
- [5] Lu, L. & Li, G. *ACS Appl. Mater. Interfaces* 8, 14812–14823 **2016**.
- [6] Gao, L., He, J., Hu, J. & Wang, C. *ACS Appl. Mater. Interfaces* 7, 25546–25552 **2015**.
- [7] Zhao, C., Qazvini, N. T., Sadati, M., *et al.* *ACS Appl. Mater. Interfaces* 11, 8749–8762 **2019**.
- [8] Wu, S., Li, J., Zhang, G., *et al.* *ACS Appl. Mater. Interfaces* 9, 3040–3049 **2017**.
- [9] Blaiszik, B. J., Kramer, S. L. B., Olugebefola, S. C., *et al.* *Annu. Rev. Mater. Res.* 40, 179–211 **2010**.
- [10] Xavier, J., Vincent, S., Meder, F. & Vollmer, F. *Nanophotonics* 7, 1–38 **2018**.
- [11] Rudolf, R., Mitschang, P. & Neitzel, M. *Compos. Part A Appl. Sci. Manuf.* **2000**
- [12] Liu, C., Qin, H. & Mather, P. T. *J. Mater. Chem.* 17, 1543–1558 **2007**.
- [13] Fan, L. F., Huang, Y. N., Rong, M. Z. & Zhang, M. Q. *Express Polym. Lett.* **2020**
- [14] Wang, S. & Urban, M. W. *Nat. Rev. Mater.* 5, 562–583 **2020**.

---

## 2. LITERATURE OVERVIEW

### 2.1. Self-healing materials

In the Roman Empire, 2000 years ago – probably without planning – the first structures using self-healing material “opus caementicium” were created and still can be observed today. The chemical background for the self-healing function could not be less trivial or ingenious at the same time: concrete-bound alkaline residues are dissolved out by penetrating water and react with the carbon dioxide present in air to form calcium carbonate, also popularly called limestone, thus the solidification process is closing the damaged area by calcination.<sup>1</sup>

Self-healing materials are able to restore their original characteristics (i.e. shape, mechanical properties, optical appearance) after a damage resulted by an external force. This mechanism is also crucial for life, examples of self-healing in biology are numerous<sup>2</sup>. They include repair at the molecular level as well as macroscopic tissue. At the molecular level an example is represented by titin. This protein functions as molecular spring in muscle.<sup>3</sup> Under mechanical stretching, individually folded domains unfold (Figure 1a-d), and when the stress is released, the domains refold.<sup>4</sup> Furthermore, folding of each domain is defined by collections of supramolecular interactions, which are broken under stress and reformed when the mechanical stress disappears.

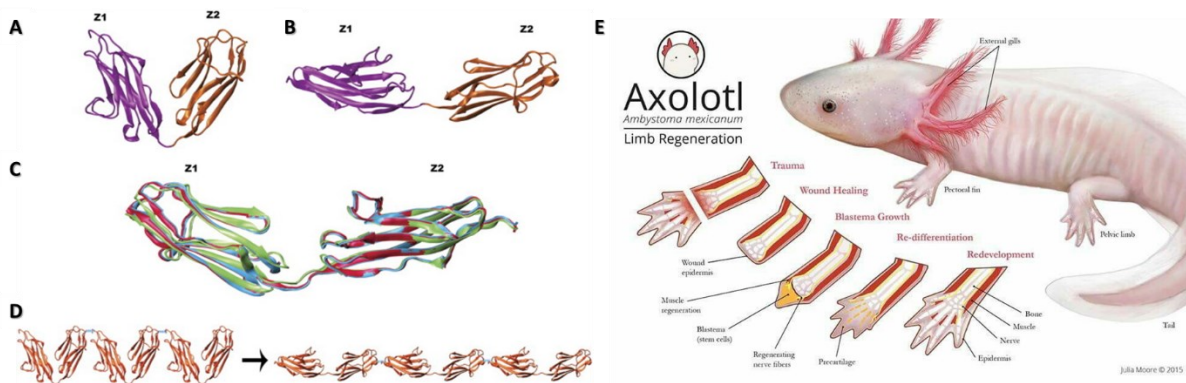


**Figure 1.** Crystal structures of the N-terminal region of titin in relaxed (a) and stretched state (b), which is comprised of tandem Z1 (purple) and Z2 (orange); NMR-RDC models of the experimentally observed semi-extended domains (c) and elasticity of the tertiary structure of titin (d).<sup>4</sup> Illustration of limbs reconstruction of Axolotl (Mexican salamander) (e).<sup>5</sup>

Living organisms have the capability to self-heal damages occurring throughout the entire biological system. In human bodies or animals, for instance, a broken bone or a skin wound heals automatically due to a combination of various processes like (i) chemotaxis, i.e., the movement of cells due to concentration gradient, (ii) neovascularization, (iii) synthesis of extracellular matrix proteins, and (iv) scar remodeling. An exceptional and outstanding example of self-healing on different levels of hierarchy is demonstrated by the *Axolotl* or *Mexican salamander* (*Ambystoma mexicanum*), shown in Figure 1e. This organism has the aptitude to reconstruct whole limbs and also parts of other complex organs like brain.<sup>6</sup>

Currently, a lot of attention is focused on artificial self-healing materials, with the growing need for sustainable development.<sup>7,8</sup> To preserve the properties and functions of materials for their entire life cycle, several chemical and physical approaches based on reversible or irreversible covalent bonds,<sup>9–11</sup> dynamic supramolecular chemistry<sup>12,13</sup> and self-healing using shape memory<sup>14</sup> were used to achieve self-healing materials and coatings.

This literature overview discusses the basics of the healing process, as well as its qualitative characteristics. The main objective is to present a report on the recent

---

progress made in the production and study of the properties of polymeric materials with an *intrinsic* self-healing mechanism, including the rearrangement of polymer chains on the surface of the damage, and/or supramolecular binding. In this case, of great interest are the systems, which exhibit the property of shape memory, to facilitate the healing process and to allow the restoration of large damages, including a distortion of the initial shape of the material.

Discussing and analysing the construction of materials, the underlying mechanisms and chemical compositions involved in various methods developed for these systems, we lay the foundation for creation of a simple system that combines excellent mechanical properties with the shape memory induced self-healing. We hope that this review will motivate new research and additional interest in this area.

### **2.1.1. Classification, physical and chemical aspects of self-healing**

Self-healing materials, depending on the mechanism of triggering of the self-healing processes, can be divided into two different classes: *autonomous* and *non-autonomous*. In *autonomous* self-healing systems, the impulse to start any restoration processes is in the damage itself, and the material is able to partially or fully restore its original characteristics without any additional external influence.<sup>15,16</sup> *Non-autonomous* self-healing mechanisms require external initiation, such as elevated temperature,<sup>17</sup> light,<sup>18,19</sup> pH changes,<sup>20</sup> or other stimuli.<sup>21</sup>

The self-healing mechanisms of artificial materials are divided into *extrinsic* and *intrinsic*. The main difference for self-healing between these two types of materials is the chemical nature of this mechanism.

---

*Extrinsic* self-healing occurs under the influence of embedded healing agents, usually in the form of closed capsules that open when a crack forms,<sup>22,23</sup> or incorporated into a polymer matrix through microchannels.<sup>24,25</sup>

For the *intrinsic* healing polymers, healing ability is inwardly connected to the (chemically or compositionally tuned) architecture of a polymer matrix. Those polymer materials are capable to repair the damage by temporarily increasing the mobility of the polymer chains, leading to the flow of the material in the damaged area and followed by restoration of the bonds strength and the recovery of the local viscosity upon the removal of the stimuli, as represented in Figure 2. This mobility can be caused by the external stimuli (e.g. temperature), and requires the presence of (i) dynamic covalent chemistry, which allows reversible breaking and creation of covalent bonds,<sup>26</sup> or (ii) reversible noncovalent interactions, such as weak covalent bonds,<sup>27,28</sup> noncovalent reversible bonding,<sup>29</sup> such as hydrogen bonds, metal/ligand complexes<sup>30</sup> or electrostatic interactions in ionomers.

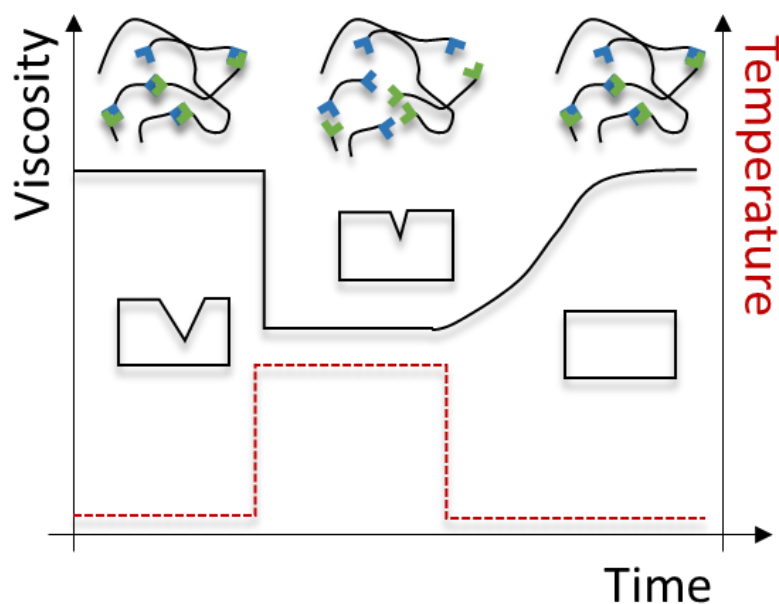


**Figure 2.** Representation of the intrinsic healing concepts. A drop in viscosity upon heating is caused by temporary network mobility, which lead to the sealing of a damage by material flow. Upon cooling the initial properties are restored.<sup>31</sup>

A four-steps mechanism, which makes it possible to decipher the complexity of strength recovery at the newly formed polymer/polymer interface and to explain the operating principle of many self-healing concepts, which are closely related to molecular mutual diffusion at glass transition temperature ( $T_g$ ) or higher, was proposed.<sup>27,32–34</sup> At this temperature, the polymer segments are sufficiently mobile to provide an effective self-healing process. Self-healing of a crack involves five stages: rearrangements of the segments of the polymer chains on the surface, surface approaching, wetting, diffusion, and randomization (Figure 3). Surface rearrangements occur mainly due to the mobility of the polymer chains and can be described by the free volume or voids concept.<sup>8,29</sup> This relatively simple model at its main stages is applicable as a universal mechanism for almost all self-healing concepts.<sup>35</sup>

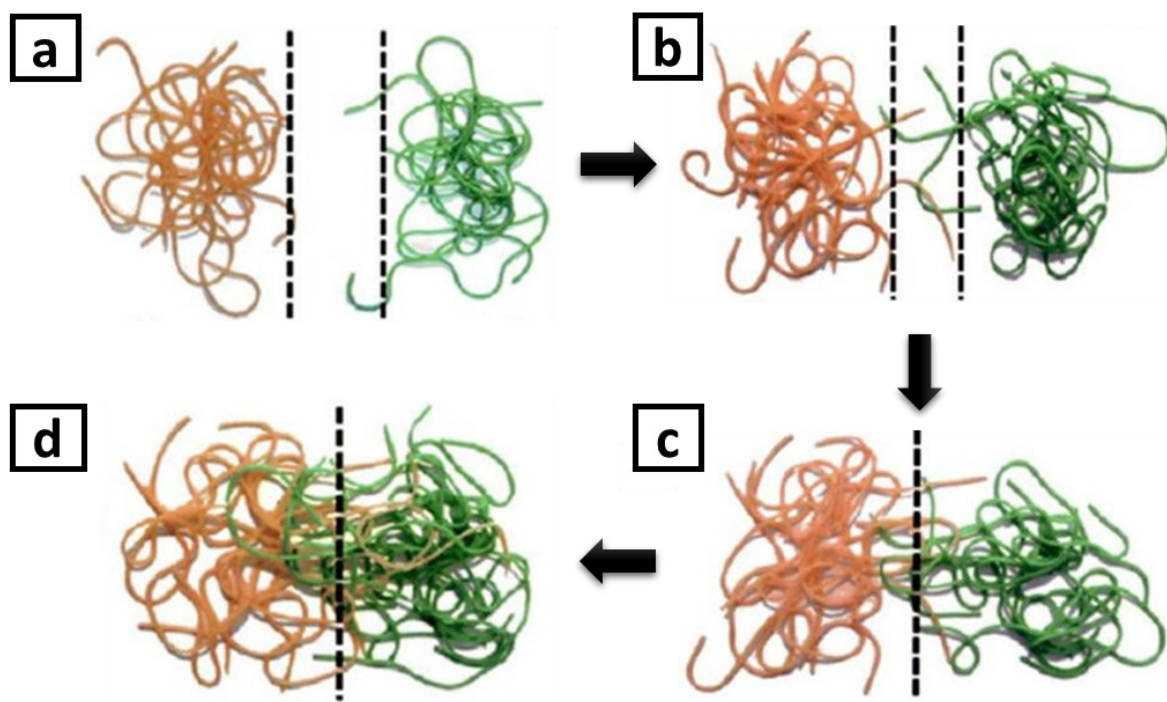


**Figure 3.** Stages of self-healing mechanism: surface rearrangement; surface approach (a); wetting (b); diffusion (c); randomization (d)<sup>27</sup>

Before the system is disturbed by the formation of a defect, it is completely stable. With the generation of the defects, there is an increase in the internal energy and entropy increment of the material, which indicate the metastable state of the

---

thermodynamic equilibrium. External infusions of energy make it possible to overcome the energy barrier and minimize the Gibbs free energy for the self-healing of the defects<sup>11,36</sup> and subsequent restoration of the material performance.<sup>37</sup>

Most of the materials which have excellent mechanical properties are based on covalent bonds, forming a cross-linked network; however, these materials do not offer the ability of self-healing. Strong covalent bond can induce shape memory, but not easy-to-repair.<sup>38</sup> However, the introduction of dynamic non-covalent bonds, which are weaker but reversible, can solve the problem of combination of the good mechanical properties with self-healing ability, which is excellent in practical applications.

Upon damage, chemical bonds are broken, and notably reversible non-covalent bonds are much easier to break than covalent bonds. The new interface which arises after the crack is formed, contains many broken bonds, which are able to be bind again with another polymer moiety, thus closing the gap and healing the damaged site.<sup>39</sup> However, the relaxation time of the non-covalent bonds is limited, and without the surface contact inside the crack, the rearrangement and rebounding will occur on the same fragment and the self-healing ability of the new interface will be lost.

For the self-healing to take place, it is crucial that the crack surfaces are brought together in close contact and fixed in this position while the rearrangement of the dynamic bonds will take place.<sup>40</sup>

Thus, in this review we will focus mainly on the intrinsic mechanisms of self-healing, with usage of reversible binding, both in combination with other types of bonds and in itself.

---

### 2.1.2. Supramolecular non-covalent interaction-based self-healing

Permanently crosslinked materials with great mechanical properties are unfavourable for the design of materials with dynamic properties. There is growing interest in the realization of adaptive properties by introduction of dynamic covalent or non-covalent bonds in polymer networks.<sup>11</sup> Dynamic covalent bonds, which have a high bond strength compared to supramolecular bonds, can be activated by suitable external stimulation.

A large number of supramolecular self-healing materials have been described in recent decades. Depending on the type of noncovalent bond involved in self-healing, these materials can be divided into the following categories: self-healing materials using hydrogen bonding,<sup>41</sup> self-healing materials via  $\pi$ - $\pi$  stacking interaction,<sup>42</sup> self-healing materials through metal-ligand interaction<sup>43-45</sup> and self-healing materials through ionomer ionic cluster formation.<sup>46-48</sup> Technically, this classification is not accurate, since many systems intentionally or unknowingly combine more than one type of non-covalent interaction in one material.

The dynamic nature of hydrogen bonding enables its widespread use to produce supramolecular polymer materials that are able to respond to and repair mechanical damage. In most cases, however, pure self-healing materials based on hydrogen bonds are elastomers, the mechanical properties of which are not completely satisfactory. Composites can be a good way of preparing the material, which combine self-healing and good mechanical properties.

Guadagno *et al* describe<sup>49</sup> the hydrogen bonding moieties that have been covalently linked to multi-wall carbon nanotubes (MWCNTs). The functionalized MWCNTs, embedded in a rubber-toughened epoxy formulation, lead to the formation of reversible bridges between nanotubes through the matrix, due to strong attractive interactions between the rubber phase, finely dispersed in the

---

matrix, and MWCNT walls. Healing efficiencies of the self-healing composite have been studied for the epoxy formulation with nanotubes (functionalized with barbituric acid and thymine groups) content 0.5% wt. For both functional groups, healing efficiencies higher than 50% have been found.

Wang *et al.*<sup>50</sup> designed new self-healing composites by hydrogen bonding interaction between carbonfibres (CFs), grafted with 1-[3-(trimethoxysilyl)proxy]urea and hyperbranched polymers obtained by interaction of a dimer acid and diethylenetriamin. Composites obtained exhibited many desirable characteristics compared to pure CFs, such as a better elasticity and mechanical stability, lower healing temperatures, and higher self-healing efficiencies (reaching 100% of the original tensile strength at room temperature for 60 min, indicating a stable healing performance). This is due to the reinforcement of the composite with nanofibres combined with reversible hydrogen bonding.

Xian Feng *et al.*<sup>51</sup> synthesized magnetic elastomer from 2-methoxyethyl acrylate, N,N-dimethylacrylamide, Fe<sub>3</sub>O<sub>4</sub> and N,N,N',N'-tetramethyldiamine as a catalyst. In this composite, Fe<sub>3</sub>O<sub>4</sub> nanoparticles, decorated/functionalized with hydrogen and carboxyl groups, easily form hydrogen bonds with the carbonyl group of the polymer chains of the main matrix. It was also elucidated that under the influence of entropic interactions between the particles and polymer matrix, the nanoparticles migrate to the fractured surfaces, which highly increased the density of the hydrogen bonds and promoted self-healing performance when the surfaces of the crack were brought together.

However, not only introduction of evenly distributed nanostructures into the polymer matrixes containing hydrogen bonds can be used for the improvement of the mechanical properties. Yan Song *et al.*<sup>52</sup> developed a system with hierarchical hydrogen bonding moieties (single, double, quadruple) in polymer backbones,

---

which allow to obtain materials featured with supertoughness ( $345 \text{ MJ m}^{-3}$ ) and high tensile strength (44 MPa) after self-healing (Figure 4).

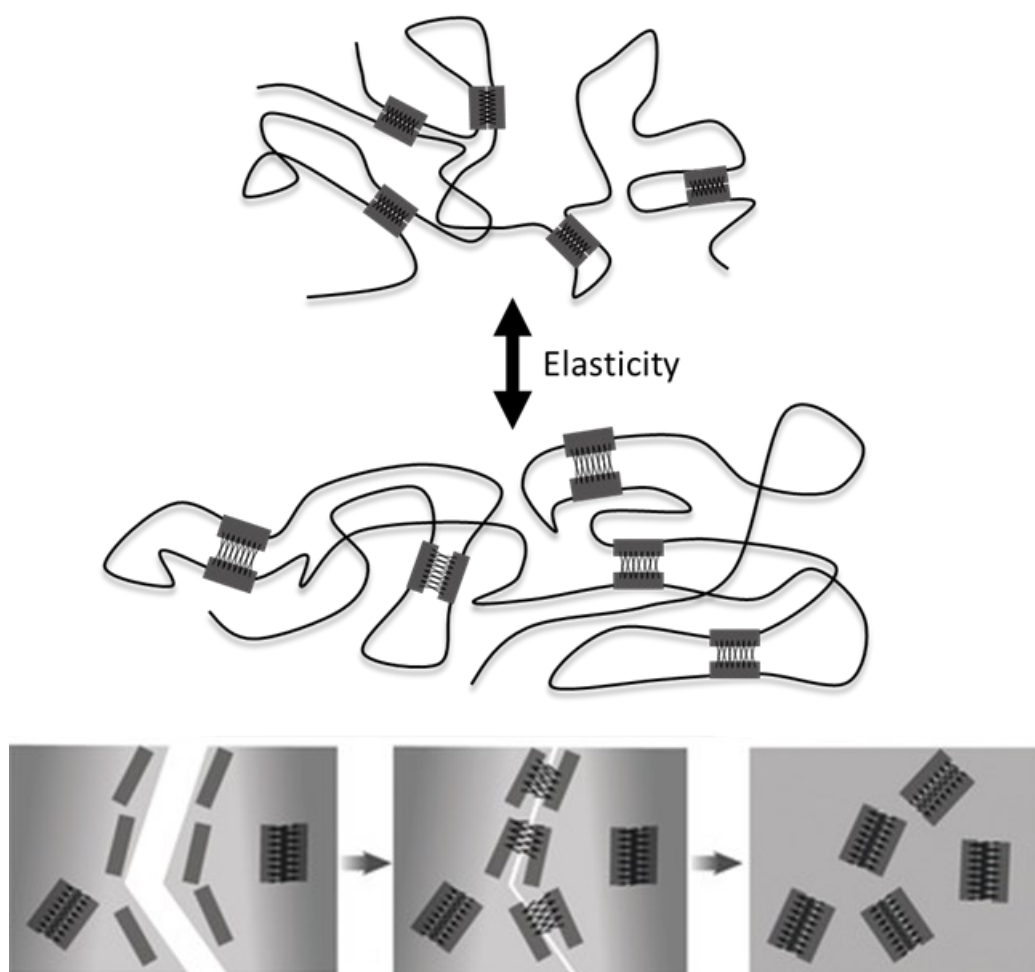


**Figure 4.** Schematic illustration of the self-healing and self-recovery process of an elastomer by the dynamic reformation of a modular structure consisting of hierarchical hydrogen bonds.<sup>52</sup>

The rigid domain, which contains hierarchical H-bonds of urethane, urea and 2-ureido-4[1H]-pyrimidinone, leads to a strong network structure with improved mechanical properties, which is at the same time dynamic for efficient self-healing. In addition, curable hierarchical hydrogen bonded polymers exhibit excellent reducibility and high energy dissipation due to the strong interaction between the polymer chains.

Ionomers are defined as polymers containing a relatively low amount of ionic groups (up to 10 to 15 mole %), which are capable of forming clusters.<sup>53</sup>

---

One of the most common type of ionomers, which demonstrates self-healing ability is poly(ethylene-co-methacrylic acid) (PEMAA) copolymer partially neutralized by sodium or zinc ions. It was previously shown that this type of ionomer exhibits the ability to self-heal after a projectile puncture.<sup>54</sup> There was a quick healing of the hole with a diameter of several mm, almost instantly and without external intervention. During the rupture, energy was transferred to the ionomer material, heating it to a melt state. The ionic regions maintained their intermolecular ionic interactions and generated elastic recovery and flowed to heal the damage.

Partially neutralized PEMA copolymer with commercial name Surlyn is able to present self-healing, as well as shape memory properties.<sup>55,56</sup> In many cases, different compositions based on Surlyn are used for the study of their self-healing and shape memory properties, such as nanocomposites based on Surlyn reinforced with different amount of silica nanoparticles,<sup>56</sup> or carbon nanotubes, which increase mechanical response of the material while maintaining self-healing properties.<sup>57,58</sup> However, apart from Surlyn, other types of materials, containing ionic dynamic bonding have been studied.<sup>54,59,60</sup>

Voorhaar *et al.*<sup>61</sup> investigated the properties of mixtures of oppositely charged triblock copolymers. Oligomeric ABA-type triblock copolymers were synthesized by reversible addition-fragmentation chain transfer-free radical polymerization (ATRP). As a middle block, poly(n-butylacrylate) was chosen. As charged outer blocks and precursors for the negatively and positively charged blocks, poly(2-(dimethylamino)ethyl acrylate) (PDMAEA) and poly(2-carboxyethylacrylate) (PCEA) were selected respectively (Figure 5). These materials showed phase separation while remaining strong electrostatic attraction within the charged domains, which allows it to self-heal after cut with an efficiency of 97 %.

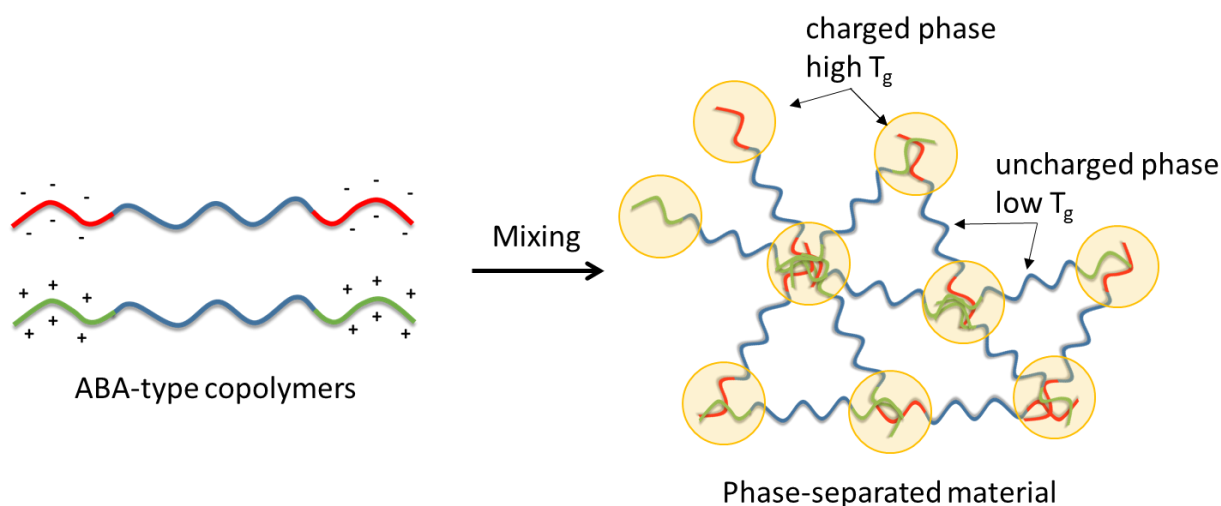


**Figure 5.** Schematic representation of the phase-separated supramolecular materials based on the combination of the oppositely charged triblock copolymers.<sup>61</sup>

New healable materials, containing non-covalent ionic bonding can also be obtained by modification of the rubbers.<sup>62,63</sup> Xu *et al.*<sup>64</sup> obtained an ionic crosslinked natural rubber via the polymerization of zinc dimethacrylate. Wherein, the reversibility of newly formed ionic associations made it possible to introduce self-healing property into the material.

Modified by imidazole isoprene–isobutylene copolymers, which have strong ionic association mediated cross-linking, also showed the ability to self-heal after damage.<sup>65</sup> Rearrangement of the ionic clusters increase the adhesion between the two cut pieces, and intrinsic mobility of the isobutylene chains ensures relocation of unassociated ionic groups.

Synthesis and properties of the ionomeric form of carboxylated styrene–butadiene rubber (XSBR) obtained by the reaction between carboxyl groups of XSBR and zinc stearate were described by Mukhopadhyay *et al.*<sup>66</sup> Association of Zn<sup>2+</sup> ions led to the formation of an ionic cross-linked network, which gave excellent properties to XSBR. In the dynamic mechanical analysis, an additional phase transition was observed, which is linked to the self-association of the ionic cross-links in the ionomers. The healing efficiency of the XSBR/Zn stearate material

---

was quantified to 68%. At the same time, the loss in tensile strength after healing event occurred was minimal.

From the point of view of industrial rubber applications, however, in most of the cases, rubbers with reversible noncovalent crosslinking network cannot withstand higher workloads in order to meet the requirements of the routine applications.<sup>67,68</sup> Another kind of ionic bonding – salt-bonding might be of interest,<sup>63,65</sup> since it is characterized by strong electrostatic interaction, which leads to hindrance in the mobility of ambient rubber chains and, at the same time, acts as reinforcing agent.<sup>69</sup>

### **2.1.3 Combination of self-healing properties with shape memory**

Another way to improve the mechanical properties of self-healing materials based on reversible non-covalent bindings is to provide a shape memory effect, either by introduction of additional covalent bonds or by using a shape memory polymer (SMP) as a component of the polymer mixture.

Intrinsic self-healing of polymer materials, which was described previously, in most cases is achieved by reversible intermolecular interactions. However, when the cracks formed are wide, which leads to a large distance between the newly appeared fractured surfaces on the opposite sides of the crack, the desired healing effect will not take place, because the molecular chains and functional groups are too far apart. This situation is very common, and to solve the problem of closing the crack and establishing of the interactions across the interface, shape memory effect (SME) has been introduced.

Two-component polymers, containing a hard/soft segmental structure, showed a thermally induced shape memory effect.<sup>70</sup> The soft segment can change its

---

stiffness significantly under glass transition or melting, while the hard segment maintains its elasticity in this temperature range. In the reference<sup>71</sup> authors investigated self-healing effects in commercially available polytetrafluoroethylene and the influence of the glass transition and the melting transition on the shape recovery performance. It was discovered, that upon heating above glass transition range, it is possible to recover the initial shape of the sample only partially, and for the full shape recovery heating to over the melting point is required.

It should be noted, that for thermally induced SMPs, shape recovery is largely dependent on the storage energy of the entropic elasticity of the polymer chains upon deformation. It is necessary for the polymers to be moderately crosslinked in order to dissipate the storage energy of elasticity, which leads to suppression of the viscous flow of macromolecular chains above the glass transition temperatures.<sup>72</sup>

However, due to the high density of the covalent bonds, these systems are rigid and receptive to mechanical damage. By inclusion of some dynamic reversible chemical functions in the main matrix, systems that are able to exhibit self-healing properties in combination with shape memory were obtained. Among them disulphide,<sup>9</sup> hindered urea,<sup>73</sup> and alkoxyamine<sup>74</sup> groups that have flexible bonding units.

By combination of shape memory polymers with different types of physical reversible bonding, new types of self-healing materials have been developed. This concept was called shape memory assisted self-healing (SMASH) and has been demonstrated in several different approaches.

The general concept is shown in Figure 6. Typical damage in the polymer material involves the creation of new free surface. In extreme cases, parts of the material can even be permanently removed from the coating, leaving an empty space. The

---

main advantage of SMASH is that the closing of the crack minimizes the treatment required, therefore, making it possible to heal large cracks and cavities.

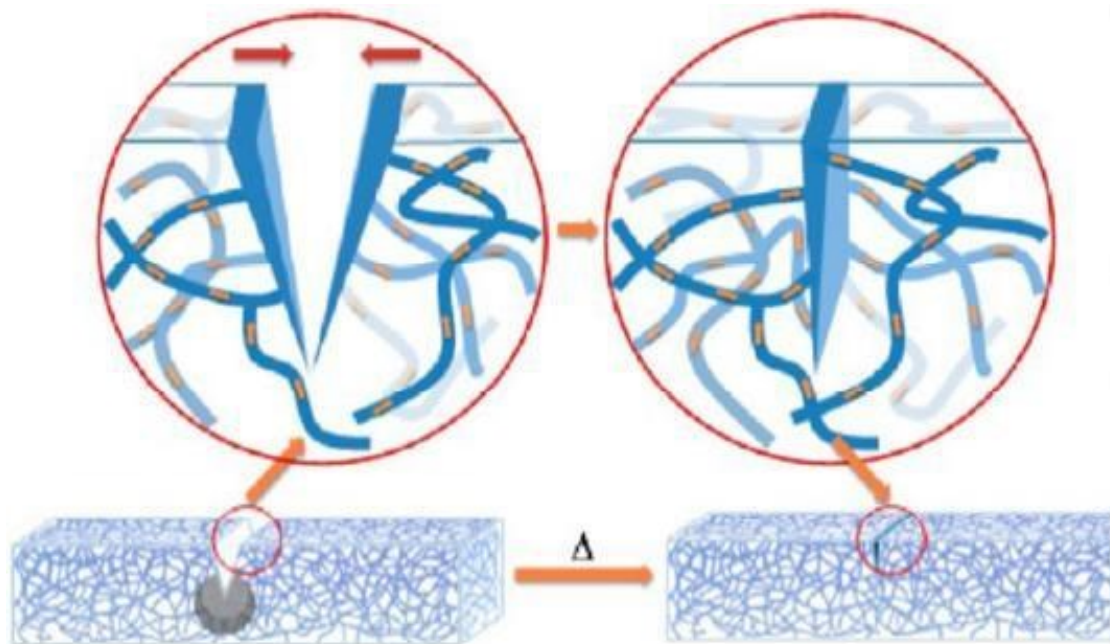


**Figure 6.** Schematic representation of a shape memory assisted self-healing material<sup>75</sup>

Introduction of chemical crosslinks into the polymer matrix allows the SME to take place. For example, by mixing of linear poly( $\epsilon$ -caprolactone) (l-PCL) with a cross-linked poly( $\epsilon$ -caprolactone) network (n-PCL), polymer blends exhibiting shape memory assisted self-healing were obtained and discussed in the reference.<sup>76</sup> Samples with  $\geq 25$  wt % of l-PCL exhibit complete healing, thanks to the shape memory effect induced by n-PCL. This effect closes the crack and causes the surfaces to rebound through re-entanglement of the l-PCL healing component within the polymer matrix.

One of the examples of the combination of shape memory matrix with physical bonding was discussed by Yuan and colleagues.<sup>77</sup> A self-healing polymer was synthesized, containing reversible as well as permanent covalent crosslinks, created by interaction of poly(propylene glycol) with boroxine and epoxy

---

respectively. An interesting feature is that it is possible to tune the properties of the materials upon dehydration and wetting from stiff to ultrasoft rubber.

Lai *et al.*<sup>78</sup> designed a material which contains weak hydrogen bonds, formed by interaction of carboxy groups along the polydimethylsiloxane chain, previously crosslinked into a three-dimensional network by poly(ethylene glycol)diglycidyl units. Chemical crosslinks maintain the permanent shape of the material and its resilience, while the weak hydrogen bonds, due to their dynamic nature can rearrange themselves at rising temperature, causing self-healing of the damage. A rheological study of the material obtained demonstrated its ability to move from viscous state into elastic at 37 °C, making it possible to trigger shape memory and self-healing effects at body temperature.

Wang *et al.*<sup>43</sup> implemented the concept of integrating self-healing and triple shape memory effect (ability to maintain initial, and two programmed shapes) into a single component material by introducing metal–ligand bonds into the molecular structure of intrinsic shape memory polymer. Poly(n-butylacrylate-co-methylmethacrylate) bearing a 2,6-bis(10-methylbenzimidazolyl)pyridine ligand side group, which is dynamically crosslinked by the metal salt zinc trifluoromethanesulfonate was synthesized, and showed quick healing rate with the efficiency close to 90 % under 4 min light irradiation or 25 min thermal treatment. The SMASH effect has been achieved by metal–ligand bond reformation on the crack surface and polymer chain diffusion under the liquefying of the material upon the action of temperature or light. The microphase separation, due to incompatibility of metal–ligand clusters and polymer matrix, lead to the formation of dispersed hard-domain nanospheres which enable the triple shape memory effect.

Throughout the years, various approaches have been developed to introduce shape memory property to the self-healing materials. For example, elastic fibres can be

---

incorporated into a polymer matrix, which after deformation compress the boundaries of the damaged region of the polymer, thus allowing the flattened surfaces to cure the defect by the relaxation of the unbound bonds on the surface of the crack<sup>75</sup>. In this case, self-healing is initiated by heating the damaged material to a temperature that exceeds both the temperature of the liquefaction of the fibres (melting temperature) and glass transition temperature of the poly( $\epsilon$ -caprolactone) matrix. Two events occur simultaneously: (1) the restoration of the matrix, which releases the accumulated deformation energy in the plastic zone and closes the crack, thus making the surface of the crack spatially closed, and (2) the melting and flowing of the thermoplastic to repair the crack.

Another type of reinforced polymer composite with shape memory and self-healing properties was invented. In the references<sup>79-81</sup> shape memory alloys in the form of thin wires were successfully integrated into the polymer matrix to provide a variety of potential effects.

Disulfide bonds, which become dynamic under the action of heat, UV light, or redox conditions can be used as dynamic bonding in combination with shape memory polymers.<sup>82,83</sup> The reversible nature of these bonds leads to the quick restoration of the mechanical properties after damage, while the shape memory effect acts as an additional recreational force that speeds up the entire healing process.

Kobayashi and colleagues<sup>84</sup> implemented a system containing two independent non-covalent interactions: hydrogen bonds and metal-ligand interactions. The material was prepared by introduction of the metal ion ( $\text{Fe}^{2+}$ ) into a bipyridine - poly(valerolactone) - polylactide - pyrimidone copolymer (bpy-PVL-PLA-UPy). The material obtained showed the ability to self-heal a scratch on the surface upon storing under 50 °C for 30 min. A comparison of metal-free and metal-containing

---

copolymers showed an increase in self-healing properties with the introduction of a metal-ligand interaction.

The shape memory study was conducted on the initial bpy-PVL-PLA-UPy film, which showed triple shape memory properties. First and second temporary shapes were programmed by temperature upon melting of the PVL part at 70 °C and subsequently cooling it to room temperature. The third shape was programmed by immersion of the bent polymer film into a 1 M Fe(BF)<sub>4</sub> EtOH solution for 3 h. Herein, the colour change indicated the formation of a metal-ligand complex of [Fe(bpy)<sub>3</sub>]<sup>2+</sup>. Upon immersion of the bent film into 1 M EtOH solution for 3 hours, the material returned to its previous shape because of the dissociation of [Fe(bpy)<sub>3</sub>]<sup>2+</sup>. The initial shape of the film was subsequently restored upon heating above melting temperature of the PVL block.

This study showed that the introduction of the two widely distributed non-covalent interactions resulted in the multi-functional and multi-responsive material, which demonstrates both self-healing and shape memory effects.

In the reference<sup>85</sup>, by introduction of double-decker polysilsesquioxane (POSS) and hindered urea bonds into the main chains of linear segmented polyurethane (PU), organic-inorganic linear segmented poly(urea urethanes) (PUUs) were synthesized, exhibiting both self-healing and shape memory properties.

Microdomains, formed by POSS-POSS interaction, provide strong physical crosslinking networks across the whole material, thereby ensuring the shape memory effect, while dynamic and reversible covalent urea bonding provide self-healing properties. The authors found that the introduction of POSS cages into the PUs matrix does not impair self-healing at room temperature. At the same time, samples showed shape restoration under small deformation.

---

## 2.2. Plasmonic nanoparticles

Nanotechnology has been a growing area of research in natural sciences since the early 1990s with nanoparticles (NPs) showing recently the fastest growth. These nanoscopic particles with sizes of 1 to 100 nm have distinct physicochemical properties based on their composition, size, form, and surrounding dielectric constant.<sup>86</sup> Nanoscale plasmonic particles can alter incoming light with regard to their adjustable shape and chemical composition.<sup>87</sup> Examples include plasmonic NPs produced from metals, such as copper,<sup>88</sup> aluminum,<sup>89</sup> metal oxides,<sup>90</sup> titanium nitride,<sup>91</sup> lanthanum hexaboride (LaB<sub>6</sub>).<sup>92</sup> NPs from gold (AuNPs),<sup>93,94</sup> silver,<sup>95</sup> platinum<sup>96</sup> and composites became attractive due to their simple and continuously improved bottom-up synthesis routes and outstanding physical and chemical properties.

Plasmon resonance in plasmonic nanoparticles has been the focus of considerable research efforts over the past two decades. There are several applications for plasmon absorption and scattering, ranging from sensing over photothermal effects to cell imaging. Furthermore, plasmon-enhanced phenomena are very attractive for a variety of applications, such as Raman spectroscopy of nearby analytes, catalysis or solar energy conversion. Furthermore, plasmon excitation is engaged in a number of complex physical processes, including nonlinear optics, optical trapping, magneto-plasmonics and optical activity.

Here, we present a general introduction of the area, with a focus of specific examples of plasmonic nanoparticles, such as gold nanorods (AuNR) and lanthanum hexaboride (LaB<sub>6</sub>). Then, we discuss methods of preparation and the most recent applications of plasmon resonance in plasmonic nanoparticles.

---

### 2.2.1. Production of plasmonic nanoparticles

To begin with, we discuss synthesis of AuNRs. The formation of nonspherical nanoparticles in an isotropic medium is an atypical phenomenon, which can, for example, be related to spontaneous aggregation of almost spherical nuclei. In order to obtain purposely non-spherical colloidal metal particles, it is necessary to create artificially anisotropic growth conditions. There are currently several methods for the synthesis of NRs:

- “hard template” synthesis;<sup>97</sup>
- the seedless growth method;<sup>98–100</sup>
- seed-mediated growth procedure;<sup>101</sup>
- photochemical synthesis.<sup>102</sup>

The production of nonspherical NR by seed-mediated growth in micellar media (ionic surfactant solutions) is probably the oldest and therefore the most elaborated synthetic route at the moment. Since under certain conditions aqueous surfactant solutions are capable of forming nonspherical micelles, they can serve as matrices for the production of nonspherical NR. The most popular surfactant used for this purpose is cetyltrimethylammonium bromide (CTAB).<sup>101</sup> By selecting in a certain way the synthesis conditions, it is possible to obtain NRs with different geometrical parameters.

Such a synthesis option was proposed by K. J. Murphys scientific group. It consists of pre-production of a seed solution by reduction of chloroauric acid ( $\text{HAuCl}_4$ ) with sodium borohydride ( $\text{NaBH}_4$ ) in the presence of sodium citrate, which stabilizes the seeds. Introduction of the obtained seeds into a solution containing  $\text{HAuCl}_4$ , CTAB and ascorbic acid lead to the formation of the AuNR.<sup>103,104</sup>

---

The mechanism of NR growth is not fully understood. One possible explanation is that nucleated particles, after being added to the growth solution, adsorb surfactant molecules and become incorporated into anisotropic micelles whose size depends on the surfactant concentration and the ionic strength of the solution; the reduction of chloroauric acid on the nuclei leads to the formation of NRs with geometry determined by micelle anisotropy. According to another assumption, surfactant molecules are predominantly adsorbed on the side faces of the growing NRs to form a bilayer, thus diffusion growth is possible only at the ends; this mechanism is called the "zipping" mechanism.<sup>105,106</sup>

There is also the assumption that rod-like growth of nanoparticles is caused by the fact that surfactant micelles containing gold chloride ions collide with micelles containing seeds predominantly at their ends because of uneven charge distribution on the micelle surface (high density of negative charge in case of micelles of the first type and positive charge in case of micelles of the second type is concentrated at the ends), which is confirmed by theoretical calculations of the potential gradient for the ellipsoid.<sup>107</sup>

Figure 8 depicts three additional plausible mechanisms that were examined and proposed to support anisotropic AuNR growth: (I) the CTAB-Br-Ag<sup>+</sup> complex for blocking the side facets as face-specific capping agents;<sup>109–111</sup> (II) anisometric CTAB micelles as "soft templates";<sup>98,112</sup> and (III) the creation of a "poisonous" silver sub-monolayer that hinders further crystal growth at the rod sides as a consequence of the silver under-potential deposition process.<sup>113,114</sup> Numerous pieces of evidence have been gathered to support each of the hypothesized processes depicted in Figure 8; nonetheless, it is not implausible for all three mechanisms to operate concurrently, which impedes a definitive mechanistic explanation.<sup>108</sup>

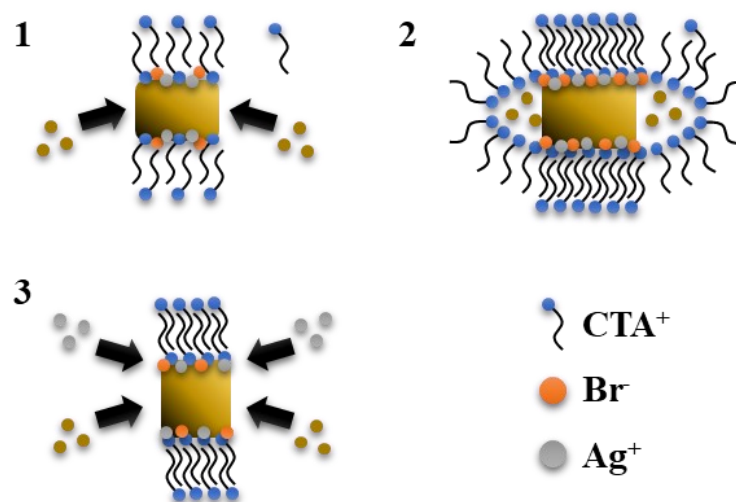


**Figure 8.** Proposed mechanisms for explaining the role of silver ions and CTAB during AuNR growth: (I) CTAB-Br-Ag<sup>+</sup> as face-specific capping agent, (II) anisometric CTAB micelles as 'soft template' and (III) silver under-potential deposition (UDP). Adapted from Ref.<sup>108</sup>

Only a few methods are developed to synthesize LaB<sub>6</sub> nanoparticles.<sup>115</sup> The practicable methods for the preparation of LaB<sub>6</sub> are including:

- solid state synthesis;<sup>116–119</sup>
- autoclave;<sup>120</sup>
- chemical vapour deposition;<sup>121</sup>
- milling process;<sup>122,123</sup>
- induction plasma technology<sup>124</sup>

Here we will focus on the two methods of LaB<sub>6</sub> preparation: milling and plasma production. Grinding makes coarse powders smaller and more uniform in size. Conventional grinding methods including ball-milling or planetary milling were effective, however could not provide desired particle size in nanoscale. A stirred bead milling process for grinding and dispersing LaB<sub>6</sub> coarse powders by using very small grinding beads was described.<sup>125</sup> LaB<sub>6</sub> may also be processed by milling to create NPs with a mean size of 110 nm in ethanol, 1-methoxy-2-propanol, and ethylene glycol without affecting its fundamental features. Common technique for nanoscale LaB<sub>6</sub> particles production are grinding processes using ethylene glycol (EG) and ZrO<sub>2</sub> grinding media (Figure 9b).<sup>124</sup>

Induction thermal plasma has been used for production of high-quality nanoparticles. This technique basically consists of heating and melting of feed particles followed by cooling under controlled conditions (Figure 9a).

When compared to milled  $\text{LaB}_6$ , highly pure  $\text{LaB}_6$  NPs produced by plasma deposition exhibit markedly different absorption behaviour, morphology and photo-thermal characteristics. First, unlike milled NPs, which are arbitrarily formed, plasma-powder has a blue tint and is spherical and partly cubic in structure.<sup>124</sup> The principal absorption peak strongly shifted to shorter wavelengths, from 1032 to 808 nm at the same concentration, which is explained by the fact that plasma-powder particles are smaller than 80 nm in diameter (Figure 9c).<sup>126,127</sup>

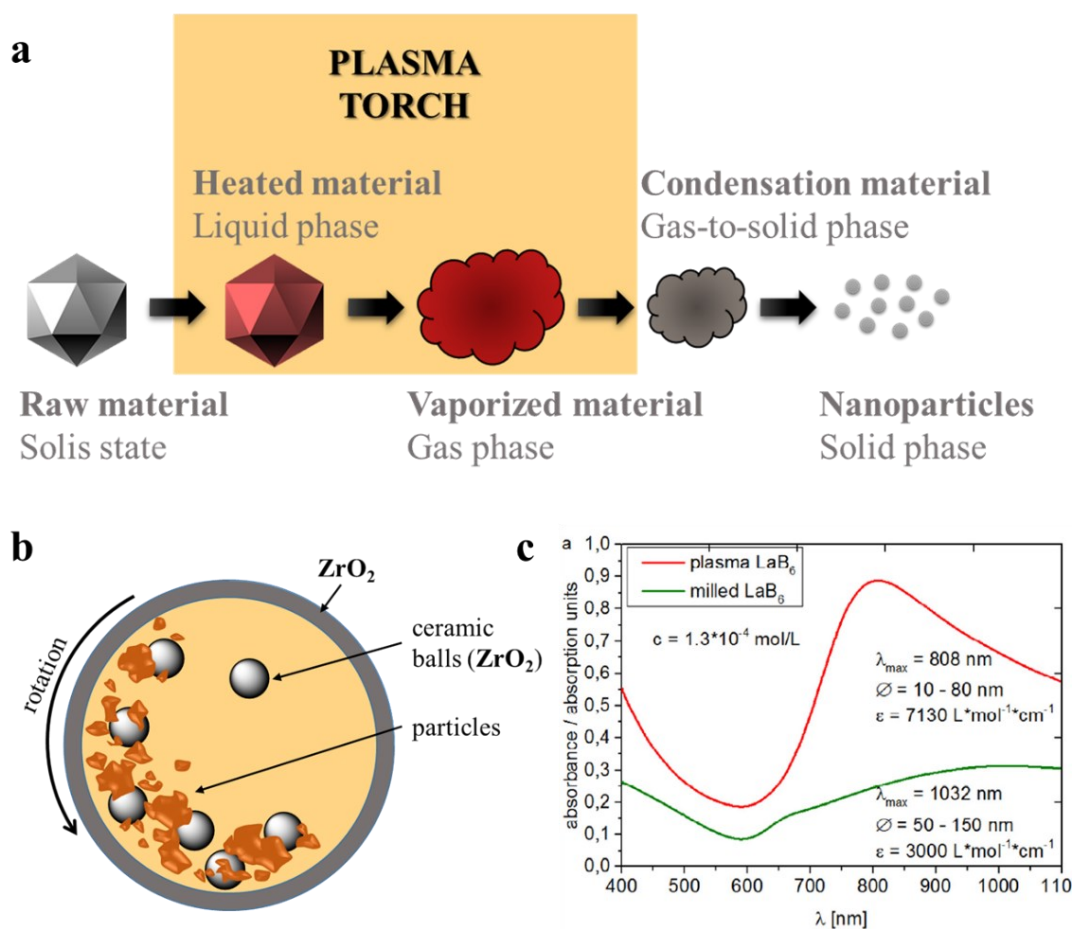


**Figure 9.** (a) schematic illustration of induction plasma technology for nanoparticles production; (b)  $\text{LaB}_6$  milling production; (c) absorbance spectra of mixed plasma-powder and milled  $\text{LaB}_6$  NPs in ethylene glycol.

---

### 2.2.2. Plasmon resonance

Gold NPs in general might be referred to as plasmonic nanoheaters owing to their effective conversion of light energy into heat.<sup>128</sup> Their extraordinarily high light-photon absorption efficiency ( $Q_{\text{abs}}$ ) at or around the surface plasmon resonance frequency is the cause of their photothermal light-to-heat conversion.<sup>129</sup> The photoexcitation of the conduction band electrons, which is the primary cause of this dissipative heating effect, is a rapid and multistage photophysical energy exchange process.<sup>130–132</sup> Factors, which strongly influence the photothermal characteristics, as well as the corresponding temperature profiles are: light intensity,<sup>133</sup> particle geometry<sup>134</sup> and type of the light source (pulsed or continuous wave).<sup>130,134</sup> Additionally, the dispersion of NPs and their interaction with the polymer matrix, especially concerning morphology, have been of particular interest when dispersing NPs into polymers to create polymer composites.<sup>135–137</sup>

Due to their asymmetrical design, AuNRs show a faint transverse surface plasmon resonance (SPR) at 530 nm that overlaps with the SPR of gold nanoparticles (AuNPs), as well as a stronger, red-shifted longitudinal SPR. Light polarized either perpendicular to the length of the AuNR, or longitudinally along the length of the AuNR, respectively, excites the longitudinal (LSPR) or transverse SPR (TSPR) (Figure 10). The longitudinal SPR's wavelength is more than 530 nm and is linearly related to the AuNRs' aspect ratio.<sup>138,139</sup> While the longitudinal plasmon mode is highly tuneable by varying the rod length, the transverse plasmon mode is somewhat insensitive to geometry.<sup>140</sup> As a result, the SPR also greatly influences the optical and visual qualities, and as the SPR increases, spherical to more elongated particle dispersions exhibit a wider color range.<sup>107,141</sup>

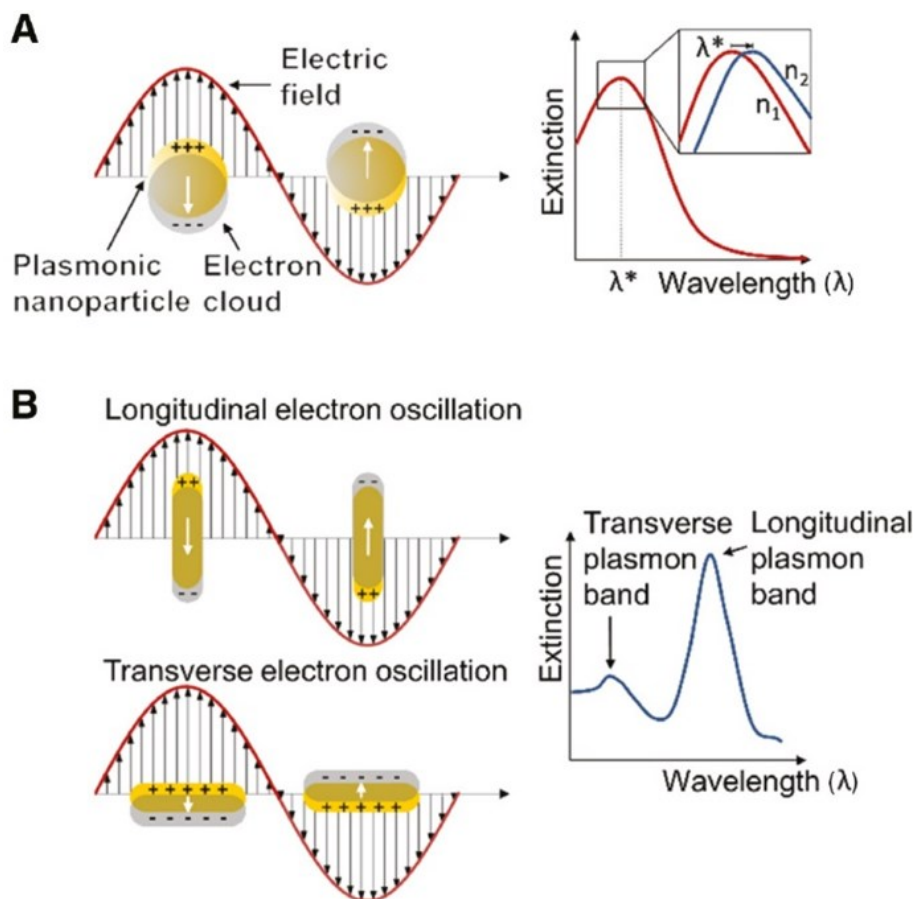


**Figure 10.** Optical absorption spectrum and SPRs of plasmonic nanoparticles (A) or AuNRs (B). The plasmon peak positions at 511 nm and 804 nm refer to the plasmon modes perpendicular and along the long axis of the rod, respectively.<sup>142</sup>

Furthermore, due to the anisotropic nature of Au nanorods, they may be formed into a variety of superstructures with varying geometries, resulting in even richer plasmonic characteristics.<sup>143</sup> As a consequence, LSPRs in Au nanorods have received a lot of attention during the past decade.<sup>107,141</sup>

The chemical environment affects the SPR wavelength and intensity in nanoparticles polymer composites. The LSPR undergoes a spectrum red-shift due to an increase of polarization charges around the rod with an increase in the dielectric constant or refractive index of the material surrounding the AuNRs.<sup>144-</sup>

---

### 2.2.3. Application of plasmonic nanoparticles

Surface modification of AuNPs with sulphur-bearing and functional ligands, such as thiol end-functionalized polyethylene glycol derivatives,<sup>147–149</sup> is a common, required procedure before use in biological systems.<sup>150</sup> AuNPs contain a broad spectrum of functional ligands, making them a promising multifunctional platform material for biomedical applications.<sup>151,152</sup> Hybrid AuNPs are used for biochemical sensing,<sup>153,154</sup> imaging,<sup>155,156</sup> tumour-targeted drug delivery<sup>157,158</sup> and radiation cancer treatment.<sup>159</sup> AuNRs may be modified and used similarly<sup>107,160</sup> and have gotten a lot of interest because of their intriguing potential in biomedical technologies, plasmon-enhanced spectroscopies, optical and optoelectronic devices.<sup>161</sup>

Noble-metal NPs may be heated locally and remotely using photothermal heating, which has practical uses in surface treatment, medication administration, curing, and processing of polymers, among others.<sup>162</sup>

Through the insertion of plasmonic nanoparticles into the solid matrix, photothermal heating has been used to accomplish local heating, giving the possibility to thermally treat a portion of a sample while leaving the rest unaltered.<sup>19,162–165</sup> Regarding the stimulus that starts the healing process, light exhibits a number of benefits: since light can travel a long way, it is simple to activate devices remotely; it is also possible to send a light beam precisely to a chosen region for local healing; and it is conceivable to manage light-triggered activities "on demand" by turning on or off the excitation light.<sup>166</sup>

Photothermal triggering of shape recovery in shape-memory-polymer (SMP) composites with embedded plasmonic nanoparticles (NPs) is of great interest.<sup>167–</sup>

---

LaB<sub>6</sub> is a perfect candidate for use as a thermionic emitter, such as long-life cathodes,<sup>173</sup> an electron source in high-resolution electron microscopes,<sup>174</sup> or in lithography devices.<sup>175</sup> Because LaB<sub>6</sub> nanoparticles are relatively cheap, easy-to-prepare, and possess better NIR photothermal conversion properties than Au nanoparticles, they could be used as novel and effective NIR photothermal conversion material.

### **2.3 Polymer based fibre composites**

Polymer-based fibre-reinforced composites (FRC) is a major class of high-performance materials, possessing many useful qualities, such as low density, excellent strength-weight ratio and fatigue strength, which allow them to be widely used in industry, for instance in the field of aircraft, space, automotive, chemical processing equipment, biomedical devices or marine infrastructure. FRC are potentially good in a wide range of various engineering fields, combining the protection of metal fibres (MF) from corrosion with low density and low metal content in comparison with conventional metallic and ceramic composites.<sup>176–180</sup> However, design and production of such composites, as well as tunability of mechanical, physical, and thermal properties for each unique application still requires careful development from industrial and academic research institutions. Hence, a significant intensification in research on the production and adjustment of the properties of FRC was observed in the last few decades.

The primary cause of FRP composite failure is delamination between the interface area and the matrix's poor fracture toughness.<sup>180–182</sup> When micro- or nanoscale damages develop while the material is being used, FRP composites tend to delaminate. The materials fail catastrophically as a result of the propagating damages. The virtually imperceptible fractures may be repaired. Therefore, there is a great need for micro- or nano-level fractures in FRP-laminated composites to

---

self-heal while they are still under development and therefore can hardly be repaired externally.

Apart from self-healing and the mentioned mechanical properties, FRP are often used for electromagnetic shielding. Electronic devices and high-frequency electromagnetic waves are being more widely used as the 5G age dawns, bringing immense ease to people's lives but also introducing new risks of electromagnetic interference (EMI). For both electrical components and humans, 5G radiation poses a major danger to their regular functioning.<sup>183–185</sup> The need for new EMI shielding materials is thus becoming more pressing than ever.<sup>186–188</sup>

Most polymers show only little or no intrinsic conductivity. Overall, it can be argued that polymer matrices are typical electric insulators. However, when they are packed/loaded with various types of fillers in the form of particles, flakes, fibers, sheets etc., such composites play an important role among the materials able to offer electromagnetic shielding. The type of polymer may affect the dispersion and distribution of fillers as well as the construction of a filler network structure inside the polymer matrices, which increases the shielding efficiency even though they are electric insulators and do not contribute to shielding.

This chapter provides a short overview of the shielding mechanism and use of FRP composites as EMI shielding materials, as well as a concept of metal/polymer composites for self-healing and the ways of its preparation. This chapter also covers various test techniques for evaluating the healing behaviour and the electromagnetic shielding effectiveness.

### **2.3.1. Mechanism of polymer-based EMI shielding materials with three-dimensional conductive networks**

EMI shielding materials made of polymers and polymer composites benefit a wide range of high-tech applications, including flexible electronic wearables, radars

and military aircraft. They exhibit excellent EMI shielding properties because of their thermal stability, mechanical strength and light weightness.<sup>189–191</sup>

The term "shielding effectiveness" (SE) refers to a metric that gauges how well a material blocks electromagnetic waves of a certain frequency as they travel through it. The potential interactions of electromagnetic waves with materials are shown in Figure 11. A portion of the incident power ( $P_I$ ) of electromagnetic waves that reach a material's surface is reflected ( $P_R$ ), while a portion is transmitted ( $P_T$ ) via the shielding material. The remaining portion is absorbed ( $P_A$ ) and lost as thermal energy.

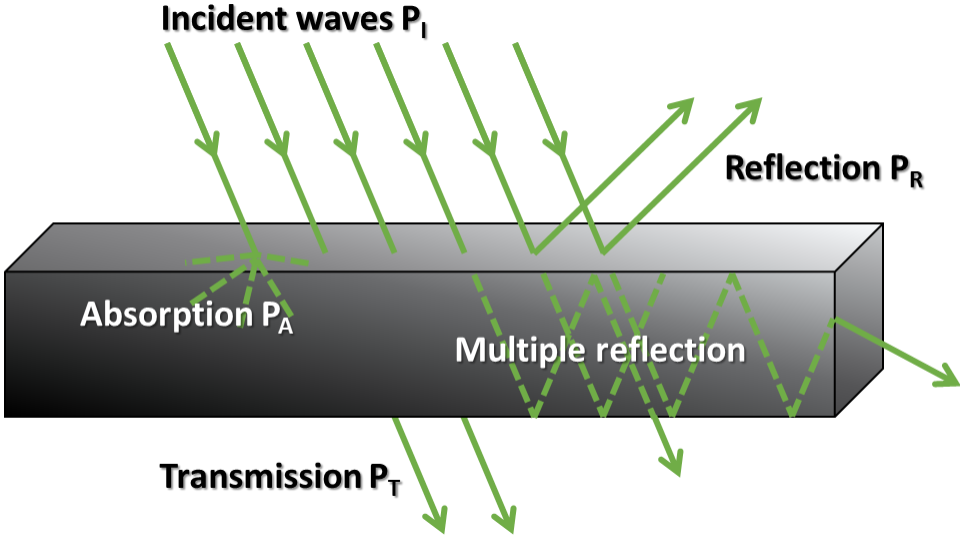


**Figure 11:** Schematic diagram of incident, reflected and transmitted power and electro-magnetic field intensities when an EM wave is incident on a 3D material

Therefore, the total attenuation, which corresponds to shielding efficiency, is caused by three distinct processes: reflection, absorption, and numerous internal reflections (eq. 1).

$$AE = 10 \log \frac{P_E}{P_T} = AE_{Reflection} + AE_{Absorption} + AE_{Multiple} \tag{1}$$

The primary mechanism of EMI shielding is reflection. Reflection loss ( $SE_{Reflection}$ ) is related to the relative impedance mismatch between the surface of

---

the shielding material and the EM waves. The magnitude of the reflection loss is proportional to the ratio of conductivity ( $\sigma$ ) and permeability ( $\mu$ ) of the material. A secondary mechanism of EMI shielding is absorption. The amplitude of the EM wave decreases exponentially inside the material as it passes through it. Thus, absorption loss results from ohmic losses and heating of the material due to the currents induced in the medium. The absorption loss ( $SE_{\text{Absorption}}$ ) in decibels (dB) depends on conductivity ( $\sigma$ ), permeability ( $\mu$ ) and sample thickness ( $d$ ). For thinner materials, radiation is trapped between two boundaries due to multiple reflection, i.e. EM waves reflect from the second boundary, come back to first boundary and are re-reflected from the first to second boundary, and so on, as shown in Figure 11.  $SE_{\text{Multiple}}$  reflection depends on  $d$  and is closely related to absorption. Hence, multiple reflection plays an important role for porous structures, high surface area, disciplinable internal structures and low-density materials with complimentary permeability.

Due to their greater conductivity, 3D conductive networks cause substantial eddy current loss and other electrical losses when electromagnetic waves penetrate them.<sup>192</sup> Regional capacitive structures may emerge between fillers with varying electrical conductivities, as well as between fillers and matrix, resulting in space charge buildup, rearrangement, and interfacial polarization in alternating electromagnetic fields. Multiple reflection and scattering in 3D conductive networks lengthen the transmission route of electromagnetic waves, boosting their reabsorption and dissipation during conduction. Crossing, leaping, and migrating of electrons in 3D conductive networks contribute to electromagnetic energy attenuation and loss of the EM wave intensity. Only a limited portion of electromagnetic waves may pass through shielding materials, resulting in an absorption-dominated shielding process.<sup>193–195</sup>

---

Apart from this, 3D conductive networks have a vast surface area, and many interfaces are able to convert electromagnetic waves into heat due to dipole polarization and dielectric loss at interfaces.

### **2.3.2. Internal heating in polymer-based Metal fibres composites**

Electronic equipment lifetimes are extended, and replacement and maintenance expenses are decreased when conductive self-healing materials are used. Consequently, the creation of such materials has attracted a lot of attention.<sup>196–203</sup>

Silver nanowires (Ag NWs) were applied by Sun *et al.*<sup>197</sup> to the polyelectrolyte multilayer membrane surface. Dropping of deionized water on the cut led to many electrical conductivity healing cycles. However, a water leak might result in an electrical device short circuit. Using a healable Diels-Alder-based polymer with Ag NWs inlaid on its surface, Pei *et al.*<sup>198</sup> created a semitransparent conductive membrane. Heating the conductive surface to 110 °C, which is higher than the tolerance of some flexible plastic devices, caused a fracture on the surface to mend. Making a highly conductive membrane that may easily repair under benign circumstances is still difficult.

By depositing Ag NWs on polycaprolactone/poly(vinyl alcohol) (PCL/PVA) composites, Li *et al.*<sup>199</sup> created membranes that are highly electrically conductive and healable under the influence of near-infrared (NIR) light. Utilizing functionalized PCL as the matrix and multi-walled carbon nanotubes (MWCNTs) as the filler, Willocq *et al.*<sup>204</sup> created thermoreversible and electrically conductive nanocomposite which can be repaired locally using the Joule effect.

In this work,<sup>205</sup> a tri-layered, light-trigger healable, and highly electrically conductive fibrous membrane was developed by deposition of reduced graphene oxide and silver nanowires onto a polycaprolactone composite that contains

AuNP. The flexible membrane was repeatedly mended electrically and structurally at the same damaged area when exposed to 532 nm light.

The feasibility of the idea of combination of the reversible intrinsic self-healing property and two-way shape memory effect in a single polymer, in order to repeatedly close a large crack and then rebound it every time the damage occurs, has been proved earlier<sup>206</sup>. In this work, polyurethane (PU) containing crosslinked elastomeric styrene-butadiene-styrene block copolymer (SBS) spheres, modified with alkoxyamine (used as the internal stress providers) was studied (Figure 12a). The reversible nature of the C-ON bonds in the alkoxyamine below its homolysis temperature is an effective way to trigger intrinsic self-healing. Besides that, for activation of SME by Joule heating, multi-walled carbon nanotubes (MWCNTs) were added to increase electrical conductivity.

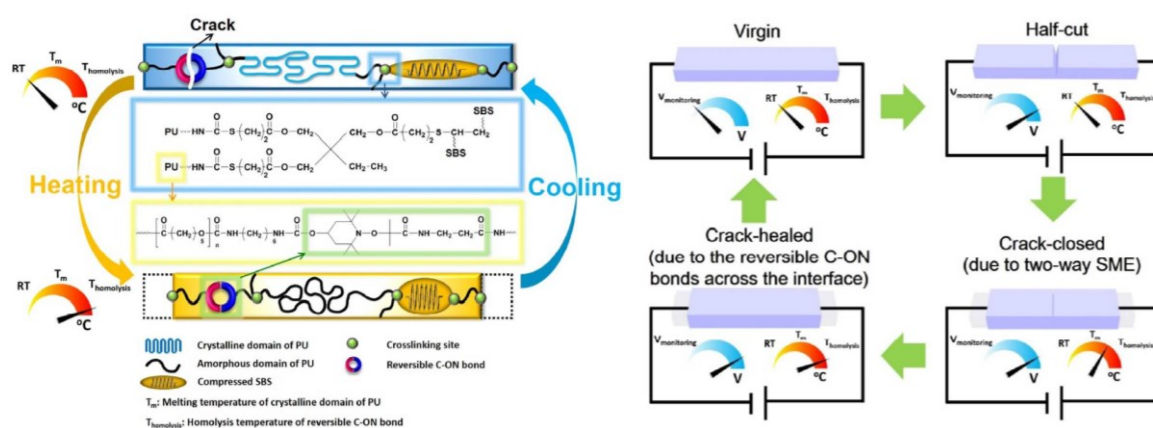


**Figure 12:** (a) Conceptual design of the polymer with dynamic reversible covalent bonding aided by two-way SME and (b) schematic drawing of autonomous repeated intrinsic self-healing of a wider crack driven by self-regulated Joule heating<sup>206</sup>

Upon cracking, paths constructed by connections between MWCNTs are partially damaged, causing the sudden increase of electrical resistance. This initiates the release of electric current from the direct current (DC) source and raising the temperature of the material by Joule heating (Figure 12b). Upon closing the crack, the conductive path is restored, and the DC source enables resistive heating for 24 h to ensure C-ON bond rearrangement. Thus, crack formation is triggering the

---

self-healing. This work expands the scope of self-healing and shape-memory polymers as the proposed approach can easily be adapted because the chemicals and manufacturing processes used above are economically scalable.

---

## 2.4. References

- [1] Wu, M., Johannesson, B. & Geiker, M. *Construction and Building Materials* vol. 28 571–583 (2012).
- [2] Diesendruck, C. E., Sottos, N. R., Moore, J. S. & White, S. R. *Angew. Chemie - Int. Ed.* 54, 10428–10447 **2015**.
- [3] Labeit, S. & Kolmerer, B. *Science (80- )*. 270, 293–296 **1995**.
- [4] Lee, E. H., Hsin, J., Mayans, O. & Schulten, K. *Biophys. J.* 93, 1719–1735 **2007**.
- [5] Gerber, T., Murawala, P., Knapp, D., *et al.* *Science (80- )*. **2018**.
- [6] Roensch, K., Tazaki, A., Chara, O. & Tanaka, E. M. *Science (80- )*. 342, 1375–1379 **2013**.
- [7] Patrick, J. F., Robb, M. J., Sottos, N. R., Moore, J. S. & White, S. R. *Nature* vol. 540 363–370 (2016).
- [8] Amaral, A. J. R. & Pasparakis, G. *Polym. Chem.* 8, 6464–6484 **2017**.
- [9] Ling, L., Li, J., Zhang, G., Sun, R. & Wong, C. P. *Macromol. Res.* 26, 365–373 **2018**.
- [10] García, F. & Smulders, M. M. J. *J. Polym. Sci. Part A Polym. Chem.* 54, 3551–3577 **2016**.
- [11] Zou, W., Dong, J., Luo, Y., Zhao, Q. & Xie, T. *Adv. Mater.* 29, **2017**.
- [12] De Espinosa, L. M., Fiore, G. L., Weder, C., Johan Foster, E. & Simon, Y. C. *Prog. Polym. Sci.* 49–50, 60–78 **2015**.
- [13] Wang, Z., Lu, X., Sun, S., Yu, C. & Xia, H. *Journal of Materials Chemistry B* vol. 7 4876–4926 (2019).
- [14] Meng, H. & Li, G. *Polymer* vol. 54 2199–2221 (2013).
- [15] Li, C. H., Wang, C., Keplinger, C., *et al.* *Nat. Chem.* 8, 618–624 **2016**.
- [16] D’Elia, E., Eslava, S., Miranda, M., Georgiou, T. K. & Saiz, E. *Sci. Rep.* 6, 1–11 **2016**.
- [17] Guo, W., Jia, Y., Tian, K., *et al.* *ACS Appl. Mater. Interfaces* 8, 21046–21054 **2016**.
- [18] Huang, L., Jiang, R., Wu, J., *et al.* *Adv. Mater.* 29, 1–6 **2017**.
- [19] Gao, L., He, J., Hu, J. & Wang, C. *ACS Appl. Mater. Interfaces* 7, 25546–25552 **2015**.
- [20] Zhao, C., Qazvini, N. T., Sadati, M., *et al.* *ACS Appl. Mater. Interfaces* 11, 8749–8762 **2019**.
- [21] Wu, S., Li, J., Zhang, G., *et al.* *ACS Appl. Mater. Interfaces* 9, 3040–3049 **2017**.
- [22] Chung, U. S., Min, J. H., Lee, P. C. & Koh, W. G. *Colloids Surfaces A Physicochem. Eng. Asp.* 518, 173–180 **2017**.
- [23] Khan, N. I., Halder, S. & Goyat, M. S. *J. Adhes.* 93, 949–963 **2017**.
- [24] Fifo, O., Ryan, K. & Basu, B. *Smart Mater. Struct.* 23, **2014**.
- [25] Garcia, S. J. & Fischer, H. R. *Self-healing polymer systems: Properties, synthesis and applications. Smart Polymers and their Applications* (Woodhead Publishing Limited, 2014).
- [26] Imato, K. & Otsuka, H. *Dynamic Covalent Chemistry* 359–387 (2017).
- [27] Wool, R. P. & O’Connor, K. M. *J. Appl. Phys.* 52, 5953–5963 **1981**.
- [28] Garcia, S. J. *Eur. Polym. J.* 53, 118–125 **2014**.
- [29] Yang, Y., Ding, X. & Urban, M. W. *Prog. Polym. Sci.* 49–50, 34–59 **2015**.
- [30] Lai, J. C., Jia, X. Y., Wang, D. P., *et al.* *Nat. Commun.* 10, 1–9 **2019**.
- [31] den Brabander, M., Fischer, H. R. & Garcia, S. J. *Self-Healing Polymeric Systems: Concepts and Applications. Smart Polymers and Their Applications* (Elsevier Ltd., 2019).
- [32] Kim, Y. H. & Wool, R. P. *Macromolecules* 16, 1115–1120 **1983**.
- [33] Prager, S. & Tirrell, M. *J. Chem. Phys.* 75, 5194–5198 **1981**.
- [34] Wool, R. P. & O’Connor, K. M. *J. Polym. Sci. Part B, Polym. Lett.* 20, 7–16 **1982**.
- [35] Wool, R. P. *Soft Matter* 4, 400–418 **2008**.
- [36] Geophysical, O. F. 95, **1990**.
- [37] Svoboda, J. & Riedel, H. 43, **1995**.
- [38] Deng, W., You, Y. & Zhang, A. *Supramolecular network-based self-healing polymer materials. Recent Advances in Smart Self-healing Polymers and Composites* (Elsevier Ltd., 2015).
- [39] Herbst, F., Döhler, D., Michael, P. & Binder, W. H. *Macromolecular Rapid Communications* vol. 34 203–220 (2013).
- [40] Fratzl, P. *Chem. Int. -- Newsmag. IUPAC* 30, 20–21 **2014**.
- [41] Yanagisawa, Y., Nan, Y., Okuro, K. & Aida, T. *Science (80- )*. 359, 72–76 **2018**.
- [42] Burattini, S., Greenland, B. W., Merino, D. H., *et al.* *J. Am. Chem. Soc.* 132, 12051–12058 **2010**.

- 
- [43] Wang, Z., Fan, W., Tong, R., Lu, X. & Xia, H. *RSC Adv.* 4, 25486–25493 **2014**.
- [44] Yang, B., Zhang, H., Peng, H., *et al.* *Polym. Chem.* 5, 1945–1953 **2014**.
- [45] Mozhdzhi, D., Ayala, S., Cromwell, O. R. & Guan, Z. *J. Am. Chem. Soc.* 136, 16128–16131 **2014**.
- [46] Aboudzadeh, A., Fernandez, M., Muñoz, M. E., Santamaría, A. & Mecerreyes, D. *Macromol. Rapid Commun.* 35, 460–465 **2014**.
- [47] Malmierca, M. A., González-Jiménez, A., Mora-Barrantes, I., *et al.* *Macromolecules* 47, 5655–5667 **2014**.
- [48] Wang, X., Vapaavuori, J., Zhao, Y. & Bazuin, C. G. *Macromolecules* 47, 7099–7108 **2014**.
- [49] Guadagno, L., Vertuccio, L., Naddeo, C., *et al.* *Compos. Part B Eng.* 157, 1–13 **2019**.
- [50] Wang, Y., Jiang, D., Zhang, L., *et al.* *Nanotechnology* 31, **2020**.
- [51] Feng, X. Q., Zhang, G. Z., Bai, Q. M., *et al.* *Macromol. Mater. Eng.* 301, 125–132 **2016**.
- [52] Song, Y., Liu, Y., Qi, T. & Li, G. L. *Angew. Chemie - Int. Ed.* 57, 13838–13842 **2018**.
- [53] Eisenberg, A. & Rinaudo, M. *Polym. Bull.* 24, 671 **1990**.
- [54] Pestka, K. A., Buckley, J. D., Kalista, S. J. & Bowers, N. R. *Sci. Rep.* 7, 1–7 **2017**.
- [55] Lu, L. & Li, G. *ACS Appl. Mater. Interfaces* 8, 14812–14823 **2016**.
- [56] Zhao, Z., Peng, F., Cavicchi, K. A., *et al.* *ACS Appl. Mater. Interfaces* 9, 27239–27249 **2017**.
- [57] Sessini, V., Raquez, J. M., Kenny, J. M., Dubois, P. & Peponi, L. *Carbohydr. Polym.* 208, 382–390 **2019**.
- [58] Calderón-Villajos, R., López, A. J., Peponi, L., Manzano-Santamaría, J. & Ureña, A. *Mater. Lett.* 249, 91–94 **2019**.
- [59] Dahlke, J., Bose, R. K., Zechel, S., *et al.* *Macromol. Chem. Phys.* 218, 1–9 **2017**.
- [60] Mordvinkin, A., Suckow, M., Böhme, F., *et al.* *Macromolecules* 52, 4169–4184 **2019**.
- [61] Voorhaar, L., Diaz, M. M., Leroux, F., *et al.* *NPG Asia Mater.* 9, e385–e385 **2017**.
- [62] Cao, L., Yuan, D., Xu, C. & Chen, Y. *Nanoscale* 9, 15696–15706 **2017**.
- [63] Wang, D., Guo, J., Zhang, H., *et al.* *J. Mater. Chem. A* 3, 12864–12872 **2015**.
- [64] Xu, C., Cao, L., Lin, B., Liang, X. & Chen, Y. *ACS Appl. Mater. Interfaces* 8, 17728–17737 **2016**.
- [65] Das, A., Sallat, A., Böhme, F., *et al.* *ACS Appl. Mater. Interfaces* 7, 20623–20630 **2015**.
- [66] Mukhopadhyay, S., Sahu, P., Bhajiwala, H., *et al.* *J. Mater. Sci.* 54, 14986–14999 **2019**.
- [67] Xiang, H. P., Rong, M. Z. & Zhang, M. Q. *ACS Sustain. Chem. Eng.* 4, 2715–2724 **2016**.
- [68] Sordo, F., Mougner, S. J., Loureiro, N., Tournilhac, F. & Michaud, V. *Macromolecules* 48, 4394–4402 **2015**.
- [69] Yang, Z., Peng, H., Wang, W. & Liu, T. *J. Appl. Polym. Sci.* 116, 2658–2667 **2010**.
- [70] Wu, X., Huang, W. M., Zhao, Y., *et al.* *Polymers* vol. 5 1169–1202 (2013).
- [71] Wu, X. L., Huang, W. M., Seow, Z. G., *et al.* *Smart Mater. Struct.* 22, **2013**.
- [72] Thakur, S. & Hu, J. *Asp. Polyurethanes* **2017**.
- [73] Zechel, S., Geitner, R., Abend, M., *et al.* *NPG Asia Mater.* 9, e420–e420 **2017**.
- [74] An, Q., Wessely, I. D., Matt, Y., *et al.* *Polym. Chem.* 10, 672–678 **2019**.
- [75] Luo, X. & Mather, P. T. *Soft Matter* 6, 2146–2149 **2010**.
- [76] Rodriguez, E. D., Luo, X. & Mather, P. T. *ACS Appl. Mater. Interfaces* 3, 152–161 **2011**.
- [77] Yuan, D., Delpierre, S., Ke, K., *et al.* *ACS Appl. Mater. Interfaces* 11, 17853–17862 **2019**.
- [78] Lai, H. Y., Wang, H. Q., Lai, J. C. & Li, C. H. *Molecules* 24, **2019**.
- [79] Cohades, A., Hostettler, N., Pauchard, M., Plummer, C. J. G. & Michaud, V. *Compos. Sci. Technol.* 161, 22–31 **2018**.
- [80] Cohades, A. & Michaud, V. *Adv. Ind. Eng. Polym. Res.* 1, 66–81 **2018**.
- [81] Zhang, P., Ogunmekan, B., Ibekwe, S., *et al.* *J. Intell. Mater. Syst. Struct.* 27, 1792–1801 **2016**.
- [82] Xu, Y. & Chen, D. *Macromol. Chem. Phys.* 217, 1191–1196 **2016**.
- [83] Wan, T. & Chen, D. *J. Mater. Sci.* 52, 197–207 **2017**.
- [84] Kobayashi, Y., Hirase, T., Takashima, Y., Harada, A. & Yamaguchi, H. *Polym. Chem.* 10, 4519–4523 **2019**.
- [85] Zhao, B., Ding, H., Xu, S. & Zheng, S. *ACS Appl. Polym. Mater.* **2019**.
- [86] Kelly, K. L., Coronado, E., Zhao, L. L. & Schatz, G. C. *J. Phys. Chem. B* **2003**.
- [87] de Aberasturi, D. J., Serrano-Montes, A. B. & Liz-Marzán, L. M. *Adv. Opt. Mater.* **2015**.
- [88] Eastman, J. A., Choi, S. U. S., Li, S., Yu, W. & Thompson, L. J. *Appl. Phys. Lett.* **2001**.

- 
- [89] Ekinci, Y., Solak, H. H. & Löffler, J. F. *J. Appl. Phys.* **2008**.
- [90] Singh, S. C. & Gopal, R. *Phys. E Low-Dimensional Syst. Nanostructures* **2008**.
- [91] Guler, U., Suslov, S., Kildishev, A. V., Boltasseva, A. & Shalaev, V. M. *Nanophotonics* **2015**.
- [92] Mattox, T. M. & Urban, J. J. *Materials* (2018).
- [93] Turkevich, J., Stevenson, P. C. & Hillier, J. *Discussions of the Faraday Society* (1951).
- [94] FRENS, G. *Nat. Phys. Sci.* **1973**.
- [95] Lea, M. C. *Am. J. Sci.* **1889**.
- [96] Henglein, A., Ershov, B. G. & Malow, M. *J. Phys. Chem.* **1995**.
- [97] Yu, Y. Y., Chang, S. S., Lee, C. L. & Wang, C. R. *J. Phys. Chem. B* **1997**.
- [98] Jana, N. R. *Small* **2005**.
- [99] Ali, M. R. K., Snyder, B. & El-Sayed, M. A. *Langmuir* **2012**.
- [100] Zijlstra, P., Bullen, C., Chon, J. W. M. & Gu, M. *J. Phys. Chem. B* **2006**.
- [101] Nikoobakht, B. & El-Sayed, M. A. *Chem. Mater.* **2003**.
- [102] Kim, F., Song, J. H. & Yang, P. *J. Am. Chem. Soc.* **2002**.
- [103] Jana, N. R., Gearheart, L. & Murphy, C. J. *Journal of Physical Chemistry B* (2001).
- [104] Busbee, B. B. D., Obare, S. O. & Murphy, C. J. 2002–2004 **2003**.
- [105] Gao, J., Bender, C. M. & Murphy, C. J. *Langmuir* **2003**.
- [106] Johnson, C. J., Dujardin, E., Davis, S. A., Murphy, C. J. & Mann, S. *J. Mater. Chem.* **2002**.
- [107] Pérez-Juste, J., Pastoriza-Santos, I., Liz-Marzán, L. M. & Mulvaney, P. *Coord. Chem. Rev.* 249, 1870–1901 **2005**.
- [108] Lohse, S. E. & Murphy, C. J. *Chemistry of Materials* (2013).
- [109] Murphy, C. J., Thompson, L. B., Alkilany, A. M., *et al.* *J. Phys. Chem. Lett.* **2010**.
- [110] Hubert, F., Testard, F. & Spalla, O. *Langmuir* **2008**.
- [111] Niidome, Y., Nakamura, Y., Honda, K., *et al.* *Chem. Commun.* **2009**.
- [112] Meena, S. K. & Sulpizi, M. *Langmuir* **2013**.
- [113] Grzelczak, M., Pérez-Juste, J., Mulvaney, P. & Liz-Marzán, L. M. *Chem. Soc. Rev.* **2008**.
- [114] Liu, M. & Guyot-Sionnest, P. *J. Phys. Chem. B* **2005**.
- [115] Yu, Y., Wang, S., Li, W. & Chen, Z. *Powder Technol.* 323, 203–207 **2018**.
- [116] Yuan, Y., Zhang, L., Liang, L., *et al.* *Ceram. Int.* **2011**.
- [117] Lafferty, J. M. *J. Appl. Phys.* **1951**.
- [118] Rea, J. R. & Kostiner, E. *J. Cryst. Growth* **1971**.
- [119] Mattox, T. M., Agrawal, A. & Milliron, D. J. *Chem. Mater.* **2015**.
- [120] Zhang, M., Yuan, L., Wang, X., *et al.* *ChemInform* **2008**.
- [121] Brewer, J. R., Deo, N., Wang, Y. M. & Cheung, C. L. *Chem. Mater.* **2007**.
- [122] Adachi, K., Miratsu, M. & Asahi, T. *J. Mater. Res.* 25, 510–521 **2010**.
- [123] Sato, Y., Terauchi, M., Mukai, M., Kaneyama, T. & Adachi, K. *Ultramicroscopy* 111, 1381–1387 **2011**.
- [124] Yavuz, V., Ngoumeni, R., Peter, K., *et al.* in *Materials Today: Proceedings* (2018).
- [125] Chen, C. J. & Chen, D. H. *Chem. Eng. J.* 180, 337–342 **2012**.
- [126] Takeda, H., Kuno, H. & Adachi, K. *J. Am. Ceram. Soc.* **2008**.
- [127] Mattox, T. M. & Urban, J. J. *Materials (Basel)*. 11, **2018**.
- [128] Fratila, R. M. & de la Fuente, J. M. *Nanomaterials for magnetic and optical hyperthermia applications. Nanomaterials for Magnetic and Optical Hyperthermia Applications* (2018).
- [129] Chen, H., Shao, L., Ming, T., *et al.* *Small* **2010**.
- [130] Link, S. & El-Sayed, M. A. *International Reviews in Physical Chemistry* (2000).
- [131] Qin, Z. & Bischof, J. C. *Chem. Soc. Rev.* **2012**.
- [132] Zhang, H., Möller, M. & Simon, U. **2017**.
- [133] Richardson, H. H., Thomas, A. C., Carlson, M. T. & Govorov, A. O. in *Materials Research Society Symposium Proceedings* (2009).
- [134] Baffou, G. & Rigneault, H. *Phys. Rev. B - Condens. Matter Mater. Phys.* **2011**.
- [135] Balazs, A. C., Emrick, T. & Russell, T. P. *Science* (2006).
- [136] Hore, M. J. A. & Composto, R. J. *Macromolecules* (2014).
- [137] Thorkelsson, K., Bai, P. & Xu, T. *Nano Today* (2015).
- [138] Jain, P. K., Lee, K. S., El-Sayed, I. H. & El-Sayed, M. A. *J. Phys. Chem. B* **2006**.
- [139] Baffou, G., Quidant, R. & Girard, C. *Appl. Phys. Lett.* **2009**.

- 
- [140] Hinman, J. G., Stork, A. J., Varnell, J. A., Gewirth, A. A. & Murphy, C. J. *Faraday Discuss.* **2016**.
- [141] Huang, X., Neretina, S. & El-Sayed, M. A. *Adv. Mater.* 21, 4880–4910 **2009**.
- [142] Xavier, J., Vincent, S., Meder, F. & Vollmer, F. *Nanophotonics* 7, 1–38 **2018**.
- [143] Schweizerhof, S., Demco, D. E., Mourran, A., Fechete, R. & Möller, M. *Langmuir* **2018**.
- [144] Lee, K. S. & El-Sayed, M. A. *J. Phys. Chem. B* **2005**.
- [145] Piliarik, M., Kvasnička, P., Galler, N., Krenn, J. R. & Homola, J. *Opt. Express* **2011**.
- [146] Takahashi, Y., Miyahara, N. & Yamada, S. *Anal. Sci.* **2013**.
- [147] Wuelfing, W. P., Gross, S. M., Miles, D. T. & Murray, R. W. *Journal of the American Chemical Society* (1998).
- [148] Otsuka, H., Akiyama, Y., Nagasaki, Y. & Kataoka, K. *J. Am. Chem. Soc.* **2001**.
- [149] Stiufiuc, R., Iacovita, C., Nicoara, R., *et al.* *J. Nanomater.* **2013**.
- [150] Murphy, C. J., Gole, A. M., Stone, J. W., *et al.* *Acc. Chem. Res.* **2008**.
- [151] Yeh, Y. C., Creran, B. & Rotello, V. M. *Nanoscale* (2012).
- [152] Her, S., Jaffray, D. A. & Allen, C. *Advanced Drug Delivery Reviews* (2017).
- [153] Durocher, S., Rezaee, A., Hamm, C., *et al.* *J. Am. Chem. Soc.* **2009**.
- [154] Li, Y., Schluesener, H. J. & Xu, S. *Gold Bull.* **2010**.
- [155] Kim, D., Park, S., Jae, H. L., Yong, Y. J. & Jon, S. *J. Am. Chem. Soc.* **2007**.
- [156] Repenko, T., Rix, A., Nedilko, A., *et al.* *Adv. Funct. Mater.* **2018**.
- [157] Dhar, S., Daniel, W. L., Giljohann, D. A., Mirkin, C. A. & Lippard, S. J. *J. Am. Chem. Soc.* **2009**.
- [158] Tran, B., Oladeji, I. O., Wang, Z., *et al.* *Electrochim. Acta* 88, 536–542 **2013**.
- [159] McQuaid, H. N., Muir, M. F., Taggart, L. E., *et al.* *Sci. Rep.* **2016**.
- [160] Stone, J., Jackson, S. & Wright, D. *Wiley Interdiscip. Rev. Nanomedicine Nanobiotechnology* **2011**.
- [161] Chen, H., Shao, L., Li, Q. & Wang, J. *Chem. Soc. Rev.* 42, 2679–2724 **2013**.
- [162] Viswanath, V., Maity, S., Bochinski, J. R., Clarke, L. I. & Gorga, R. E. *Macromolecules* **2013**.
- [163] Zhang, H. & Zhao, Y. *ACS Appl. Mater. Interfaces* **2013**.
- [164] Maity, S., Bochinski, J. R. & Clarke, L. I. *Adv. Funct. Mater.* **2012**.
- [165] Li, Y., Verbiest, T., Strobbe, R. & Vankelecom, I. F. J. *J. Mater. Chem. A* **2014**.
- [166] Habault, D., Zhang, H. & Zhao, Y. *Chem. Soc. Rev.* **2013**.
- [167] Hribar, K. C., Metter, R. B., Ifkovits, J. L., Troxler, T. & Burdick, J. A. *Small* **2009**.
- [168] Xiao, Z., Wu, Q., Luo, S., *et al.* *Part. Part. Syst. Charact.* **2013**.
- [169] Le, D. M., Tycon, M. A., Fecko, C. J. & Ashby, V. S. *J. Appl. Polym. Sci.* **2013**.
- [170] Leonardi, A. B., Puig, J., Antonacci, J., *et al.* *Eur. Polym. J.* **2015**.
- [171] Yao, Y., Hoang, P. T. & Liu, T. *J. Mater. Sci. Technol.* **2017**.
- [172] Lu, X., Zhang, H., Fei, G., *et al.* *Adv. Mater.* **2018**.
- [173] Broers, A. N. *J. Appl. Phys.* **1967**.
- [174] Hawker, C. J. & Russell, T. P. *Mater. Today* 9, 30–39 (2006)
- [175] Dix, C., Loosemore, P. & Jones, M. *Microelectron. Eng.* **1990**.
- [176] Dransfield, K., Baillie, C. & Mai, Y. W. *Compos. Sci. Technol.* **1994**.
- [177] Palmeri, M. J., Putz, K. W., Ramanathan, T. & Brinson, L. C. *Compos. Sci. Technol.* **2011**.
- [178] Ozcan, S., Tezcan, J. & Filip, P. *Carbon N. Y.* **2009**.
- [179] Fitzer, E. *Carbon* (1987).
- [180] Garg, A. C. & Mai, Y. W. *Compos. Sci. Technol.* **1988**.
- [181] Argon, A. S. & Cohen, R. E. *Polymer (Guildf)*. **2003**.
- [182] Choi, N. S., Kinloch, A. J. & Williams, J. G. *J. Compos. Mater.* **1999**.
- [183] Ling, J., Zhai, W., Feng, W., *et al.* *ACS Appl. Mater. Interfaces* **2013**.
- [184] Yuan, B., Bao, C., Qian, X., *et al.* *Carbon N. Y.* **2014**.
- [185] Singh, K., Ohlan, A., Pham, V. H., *et al.* *Nanoscale* **2013**.
- [186] Ma, Z., Kang, S., Ma, J., *et al.* *ACS Nano* **2020**.
- [187] Guo, Y., Ruan, K. & Gu, J. *Mater. Today Phys.* **2021**.
- [188] Kim, H. R., Fujimori, K., Kim, B. S. & Kim, I. S. *Compos. Sci. Technol.* 72, 1233–1239 **2012**.
- [189] Wang, L., Qiu, H., Liang, C., *et al.* *Carbon N. Y.* 141, 506–514 **2019**.
- [190] Liang, C., Song, P., Qiu, H., *et al.* *Compos. Part A Appl. Sci. Manuf.* **2019**.
- [191] Zhang, C., Li, Y., Kang, W., Liu, X. & Wang, Q. *SusMat* 1, 127–147 **2021**.

- 
- [192] Li, Q., Zhao, Y., Wang, L., *et al.* *Carbon N. Y.* 162, 86–94 **2020**.
- [193] Wu, X., Han, B., Zhang, H. Bin, *et al.* *Chem. Eng. J.* 381, 122622 **2020**.
- [194] Song, P., Liu, B., Liang, C., *et al.* *Nano-Micro Lett.* 13, 1–17 **2021**.
- [195] Zhao, S., Zhang, H. Bin, Luo, J. Q., *et al.* *ACS Nano* **2018**.
- [196] Du, R., Wu, J., Chen, L., *et al.* *Small* 10, 1387–1393 **2014**.
- [197] Li, Y., Chen, S., Wu, M. & Sun, J. *Adv. Mater.* **2012**.
- [198] Gong, C., Liang, J., Hu, W., *et al.* *Adv. Mater.* **2013**.
- [199] Li, Y., Chen, S., Wu, M. & Sun, J. *ACS Appl. Mater. Interfaces* **2014**.
- [200] Yang, W., Song, J., Wu, X., *et al.* *J. Mater. Chem. A* **2015**.
- [201] Tee, B. C. K., Wang, C., Allen, R. & Bao, Z. *Nat. Nanotechnol.* **2012**.
- [202] Wang, H., Zhu, B., Jiang, W., *et al.* *Adv. Mater.* **2014**.
- [203] Guo, K., Zhang, D. L., Zhang, X. M., *et al.* *Angew. Chemie - Int. Ed.* **2015**.
- [204] Willocq, B., Bose, R. K., Khelifa, F., *et al.* *J. Mater. Chem. A* **2016**.
- [205] Chen, L., Si, L., Wu, F., *et al.* *J. Mater. Chem. C* 4, 10018–10025 **2016**.
- [206] Fan, L. F., Rong, M. Z., Zhang, M. Q. & Chen, X. D. *ACS Appl. Mater. Interfaces* 10, 38538–38546 **2018**.

---

# 3. TRIPLE NETWORK SYSTEMS FROM COMMERCIALY AVAILABLE POLYMERS

*This chapter is based in part on the author's previously published article: **Selezneva E.V.**, Bakirov A.V., Sedush N.G., Bystrova A.V., Chvalun S.N., Demco D., Möller M., How Shape Memory Effects can Contribute to Improved Self-Healing Properties in Polymer Materials, *Macromolecules* **2021**, 54, 5, 2506–2517. Some content has been adapted accordingly.*

## 3.1. Introduction

Polymer intrinsic self-healing mostly functions through reversible inter- and/or intramolecular interactions and allows for numerous healings of the same location in the material.<sup>1</sup> However, when the cracks are so large that the molecular chains and functional groups on the opposite cracked surfaces are far apart, a problem arises. The expected healing chemistry cannot take effect in this circumstance, which is usual in practise. To tackle the challenge, the shape memory effect (SME) was utilized to narrow the opening fractures first, laying the groundwork for subsequent interaction across the interface.<sup>2–5</sup> As a result, the healing mechanism applicable to microcracks can continue to function.

Self-healing shape memory polymers are intelligent polymeric materials that can return from a deformed state to their original shape under the action of an external stimulus.<sup>6</sup> Polymers with this property have many applications in a variety of fields such as medicine and transport. However, self-healing is limited by the type

---

of damage: when the damage is permanent, such as cracks, the shape memory property only allows closure of the damage, but not complete interfacial sealing.<sup>7</sup>

A certain class of ionomers has previously been shown to exhibit self-healing ability after puncture.<sup>8</sup> Rapid healing of a hole of a few mm in diameter occurred almost instantaneously and without external intervention. The ionomers contain ionic groups capable of forming clusters. During rupture, energy is transferred to the ionomer material, heating it to a molten state, with the ionic regions retaining their intermolecular ionic interactions, generating an elastic energy and flowing, therefore healing the damage.

Ion clustering supported by the shape memory effect of the covalent network could be sufficient to cause self-healing. The material can keep two memories on its original structure: the memory on the shape preserved by the deformed network and the memory of the ion clusters that got deformed or fractured but which strive to recover. However, structural reorganization or flow of ionomers is characterized by three relaxation times, the Rouse type relaxation  $\tau_R$  of the polymer segments, the life time of the ion-pair/ion-pair contact  $\tau_i$  (corresponding to ion hopping), and the terminal relaxation time  $t_d$  (corresponding to reptation).<sup>9,10</sup> It is characteristic for ionomers in the melt, that  $\tau_i > \tau_R$  and  $t_d$  is significantly extended by the ion cluster formation compared to a non-sticky polymer (without ionic groups) of the same molecular weight. This hierarchy of relaxation times is essential for a self-healing material. In order to allow fast recovery of a cohesive contact,  $\tau_i$  should be not too long, however,  $\tau_i$  presents also the time for the loss of the microscopic mending ability. For a merely transient network  $t_d$  is the time after which all memories on the original shape get lost. Synchronization of the different events and their rates is essential for self-healing, but also a difficult task, in particular when one takes into account the different temperature dependencies of the underlying mechanisms.

---

Another aspect of polymer self-healing concerns shape recovery. Ideally, this should not be influenced by manipulation, such as squeezing the cut pieces together, but by their autonomous compression. This requires the ability to memorize shape. Classically, a material with shape memory is programmed to transform shape from state A to state B, which are both intact. For polymeric materials, this can be accomplished by using dual-mesh networks that combine covalent and noncovalent, thermoreversible crosslinks.<sup>11</sup> When such a dual-mesh material has been stretched and secured in this stretched state by noncovalent bonds, the covalent network will store elastic energy. For shape memory materials that promote self-healing. This stored elastic energy may be useful for initiating autonomous self-healing.<sup>12,13</sup>

Based on these considerations, we report here on a self-healing material that has been engineered as a multilayer cross-linked polymer network consisting of strong and durable non-covalent aggregate structures and a covalent network that will retain memory of the original shape after mechanical damage to the material (Figure 1). Thus, we intended to combine two memory effects: (i) the one based on microdeformations in the surface caused by damage, and (ii) deformations in the shape of the material. Both effects are designed for metastability and slow relaxation. Thus, energy is stored in the material, which can cause healing as the object relaxes during aging or annealing.

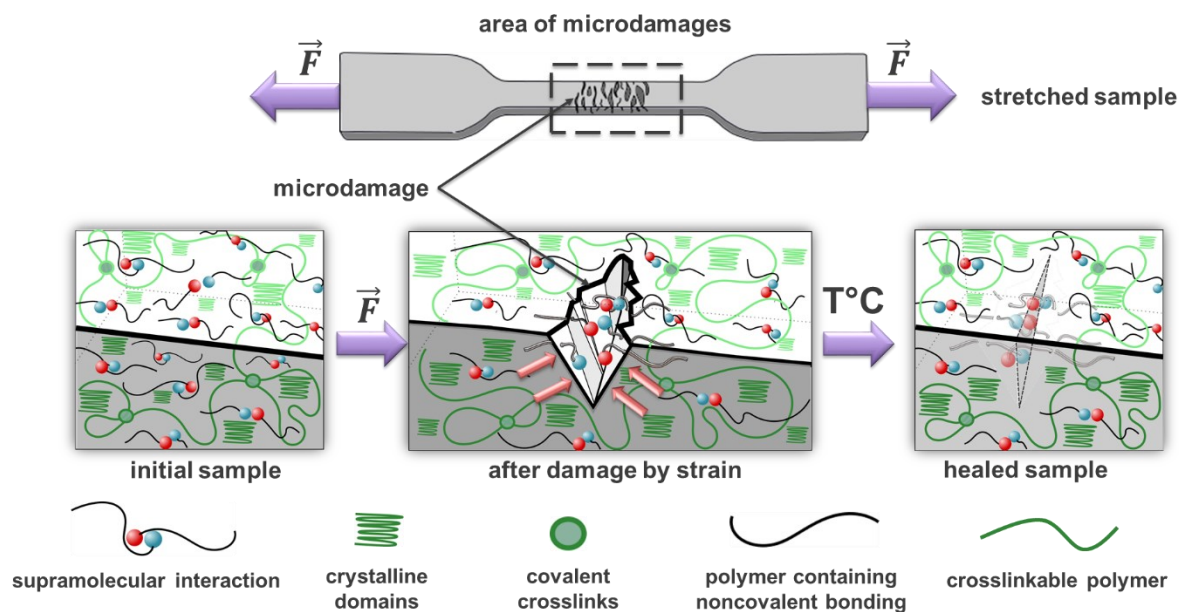


**Figure 1.** Schematic concept of a microcrack healing in a sample, combining several types of binding: strong and durable noncovalent aggregate structures and a covalent network.

If the material is covalently cross-linked, the network deforms and retains some tension after damage to restore the original shape until the entire object is destroyed. If the material also contains reversible cross-linking, it results in cold deformation. Since neither the reversible bonds nor the covalent network structure can recover in the solid state (below  $T_m$ ), the material can retain a memory of the microscopic structure, i.e., the topology of the reversible cross-links, as well as its macroscopic shape. This memory is preserved until the material relaxes, either non-autonomously with temperature rise or autonomously with direct restoration of the original shape and structure. Ideally, elastic restoration of the covalent network would first close cracks and voids or smooth out scratches, and then restoration of broken reversible bonds would trigger coherent healing at the microscale. This is peculiar to our concept, which primarily applies only to damage in which the object is not fragmented, so that the covalent network can still support repair. Consequently, self-healing will be limited to microcracks, small cuts and scratches.

---

To realize our concept, we chose a combination of readily available industrially produced polymers, namely, a commercial ionomer and an ethylene/propylene copolymer containing ethylidene-norbornene for radical crosslinking: Surlyn<sup>TM</sup> and amorphous EPDM. The ionomer is a copolymer of ethylene and methacrylic acid, which contains 5.4 mol% methacrylic acid units that have been partially neutralized with sodium or zinc. The ethylene content of the EPDM was chosen to be 56 wt % and the diene fraction was chosen to be 5.5 wt %. The ionic groups are aggregated as nanoclusters that act as reversible crosslinks. Surlyn<sup>TM</sup>-type ionomers are well known for their special self-healing properties under high impact damage causing significant temperature increase, so that the ion clusters can reorganize.<sup>14</sup> Longer polyethylene (PE) fragments in the ionomer can crystallize. Crystallization causes a hardness, which distinguishes it from rubber self-healing materials such as those reported in Leibler.<sup>15</sup> To understand the complex interaction of cross-linking and reduction processes, we conducted a thorough study of the temperature-dependent structural organization of ionomer mixtures and their structural rearrangement.

## **3.2. Results and discussion**

### **3.2.1. Obtaining of multicomponent materials capable of multiscale damage healing**

If poly(ethylene-co-methacrylic acid/methacrylate) ionomers are blended with EPDM and treated with a peroxide, we can expect that the material will develop three types of crosslinks at ambient temperature: (i) the covalent crosslinks formed by radical reaction, preferentially with the double bonds in EPDM; (ii) reversible crosslinks formed by clustering of the ionic groups; and (iii) reversible crosslinks formed by crystallites of longer ethylene sequences in the ionomer. Figure 2 demonstrates the structure model of such a blend. The covalent crosslinks are concentrated within the amorphous regions between ionic clusters and

crystallites. The amorphous regions consist of ethylene- and ethylene-co-propylene-segments with a low glass transition temperature of  $-60\text{ }^{\circ}\text{C}$ . The ionic clusters have a softening temperature that is above room temperature (see Figure 3). Longer ethylene segments of the two constituting polymers may to some extent be included in the same crosslinking crystallite.

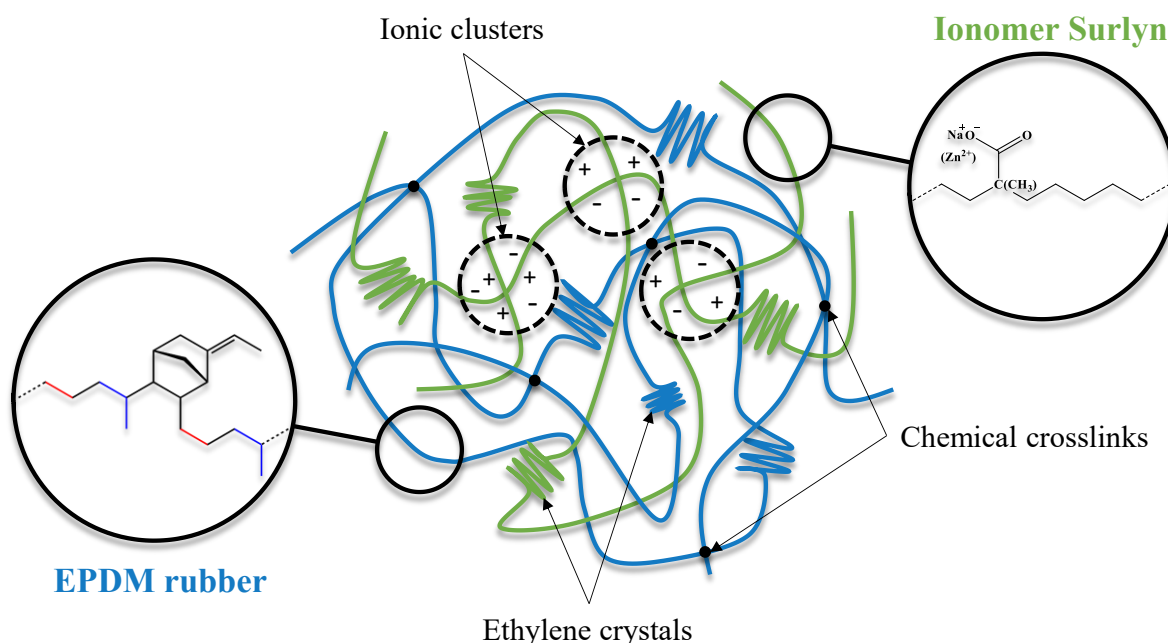


**Figure 2.** Structure model of a peroxide crosslinked blend of the Surlyn<sup>TM</sup> ionomer and EPDM rubber. The material combines crosslinks by aggregation of ionic groups, crosslinks by PE crystallites and covalent crosslinks formed by radical crosslinking.

Cold deformation at room temperature to the extent that defects like microfractures, voids or surface scratches are formed will affect the network in such way that (i) ionic clusters will break up in smaller clusters; (ii) crystalline domains will be reoriented, break, deform and unravel; (iii) the covalent network will elastically deform and eventually break up at high strain. Each of these processes relate to a characteristic time scale at which it can occur and a characteristic relaxation time to get reversed. Within the self-healing concept discussed here, relaxation of the elastic network should proceed before the defect reversible crosslinks can relax to a new more near to equilibrium structure, i.e. before the memory of the reversible crosslinks gets lost. With other words,

---

miscibility of the two polymers in the amorphous phase and adjustment of the relaxation times of the structural distortions are essential conditions to enable the self-healing effect.

In order to prepare the materials, EPDM and the ionomer were mixed together using two different procedures. According to the first procedure, the components were dissolved in a solvent together with dicumyl peroxide as a crosslinking agent to yield a clear dilute solution. This solution was precipitated in methanol and the dried precipitate was moulded to a test specimen by means of a hot press (Figure S1). Coprecipitation has been shown to enable efficient premixing before elevated temperature moulding. The second procedure implied mixing of the polymer melts together with dicumyl peroxide and shaping them by injection moulding. All blends were optically clear above the melting temperature and became opaque after cooling to ambient temperature. Opaqueness at ambient temperature is expected because of the crystallization of the polyethylene (PE) segments. Optical clarity above  $T_m$ , indicates intimate mixing of the ionomer and the amorphous EPDM above  $T_m$  (Figure S2).

When the samples prepared by injection moulding were annealed outside of the mold for 10 min at 110 °C, they shrank in length by 40 %; when the mold temperature was set to 95 °C, shrinkage in length could be reduced to 18 % (Figure S3). The shrinkage indicates insufficient relaxation of the polymer melt inside of the mold. Figure S2 depicts a Surlyn 9150/EPDM crosslinked by dicumylperoxid (DCP) disc obtained using hot pressing with longer heat exposure compared to injection moulding. The left image shows a partially crystalline, fully relaxed sample removed from the mold. The image on the right shows the sample at 110 °C, when it became completely transparent. The shrinkage in diameter caused by annealing was less than 2 %, indicating that the structure is equilibrated during moulding in the hot press.

---

### 3.2.2. Investigation of the obtained samples by different physical methods

#### Thermal analysis of the obtained samples

Table 1 lists the thermal characterization of the three polymers together with data measured for both non-crosslinked and crosslinked blends. All data in Table 1 were recorded with samples that had been mixed by the second procedure in the melt. Comparison with DSC data for the samples premixed by coprecipitation did not yield differentiating results. Like expected for the ionomer, we observed two thermal transitions in addition to the glass transition of the matrix.<sup>16</sup> The latter could only be measured for EPDM and its blends with the ionomers. Obviously, the amorphous polymer segments and domains in the ionomer are confined in their mobility by the ionic clusters and crystallites of longer  $-(\text{CH}_2-\text{CH}_2)-$  segments. Because the transitions are rather broad, we indicated only peak temperatures in Table 1. A more detailed view is given in Figure 3, where we depict characteristic DSC-traces. The high temperature transition,  $T_m$ , has been assigned to the melting of crystallites of longer  $-(\text{CH}_2-\text{CH}_2)-$  segments.<sup>17-19</sup> The low temperature transition  $T_i$  is characteristic for the ion clusters. We recently presented  $^{23}\text{Na}$ -NMR results which demonstrate the onset of mobility for the Na-ions at  $T_i$  corresponding to a kind of glass transition of the clusters. Because of the small heat effect and the fact that  $T_i$  is only observed for samples that were aged for several hours leading to an increase in density, we concluded that  $T_i$  may represent at least partially an enthalpy relaxation effect, not excluding some coincidence with melting of badly ordered crystallites of  $-(\text{CH}_2-\text{CH}_2)-$  segments. Above  $T_i$ , the ionic clusters persist and do not even dissolve above  $T_m$  as it has been shown by the resilient flow behavior of ionomers at high temperatures<sup>20</sup> as well as by  $^{23}\text{Na}$ -NMR.

**Table 1.** Calorimetric characterization of the poly(ethylene-co-methacrylic acid/Me-methacrylate) ionomer and its blend with EPDM, measured at a heating rate of 10 K/min.

N	Sample	Sample history	T <sub>g</sub> °C	T <sub>i</sub> (ΔH) °C (J/g)	T <sub>m</sub> (ΔH) °C (J/g)	Degree of cryst.*
1	EPDM	1 <sup>st</sup> heating	-60	--	--	--
2	Surlyn PC2000	1 <sup>st</sup> heating 2 <sup>nd</sup> heating 3 <sup>rd</sup> heating	-- -- --	52°(7.7) -- 50° (8.9)	93° (31.3) 92° (39.9) 91° (43.4)	11% 13% 15%
3	Surlyn 9150	1 <sup>st</sup> heating 2 <sup>nd</sup> heating 3 <sup>rd</sup> heating	-- -- --	57° (12.1) -- 59° (10.2)	94° (36.8) 93° (41.3) 93° (29.5)	13% 14%
4	Surlyn PC2000 /EPDM	1 <sup>st</sup> heating 2 <sup>nd</sup> heating 3 <sup>rd</sup> heating	-60 -60 -60	52° (5.5) -- 52° (5.9)	92° (21.9) 93° (24.4) 92° (24.4)	8% 8,5% 8,5%
5	Surlyn PC2000 /EPDM - crosslinked	1 <sup>st</sup> heating 2 <sup>nd</sup> heating 3 <sup>rd</sup> heating	-60 -60 -61	52° (5.3) -- 53°(4.7)	92°(23.6) 93°(24.3) 93° (24.8)	8% 8,5% 8,6%
6	Surlyn 9150 /EPDM	1 <sup>st</sup> heating 2 <sup>nd</sup> heating 3 <sup>rd</sup> heating	-60 -60 -60	56° (5.3) -- 53°(4.4)	99°(31.5) 98°(37.7) 98°(30.7)	11% 13% 10.5%
7	Surlyn 9150 /EPDM crosslinked	1 <sup>st</sup> heating 2 <sup>nd</sup> heating 3 <sup>rd</sup> heating	-60 -60 -60	56° (3.9) -- 54° (6.4)	97° (23.0) 96° (35.5) 96° (30.4)	8% 13% 10.5%

\*Degree of crystallinity calculate from ΔH (T<sub>m</sub>) relative to the equilibrium heat of fusion of polyethylene ΔH<sub>f</sub><sup>o</sup> = 289 J/g.<sup>21</sup>

Comparison of the DSC data of the pure ionomers and their blends demonstrated little changes. Irrespective of blending and crosslinking as well as of the counterions, the transition assigned to the ion clusters was observed only for samples that have been annealed at room temperature. Annealing in order to recover the T<sub>i</sub> transition required only 8 hours. When the samples were annealed

at 65 °C, the degree of crystallinity calculated from the  $T_m$  transition increased and the peak narrowed considerably.

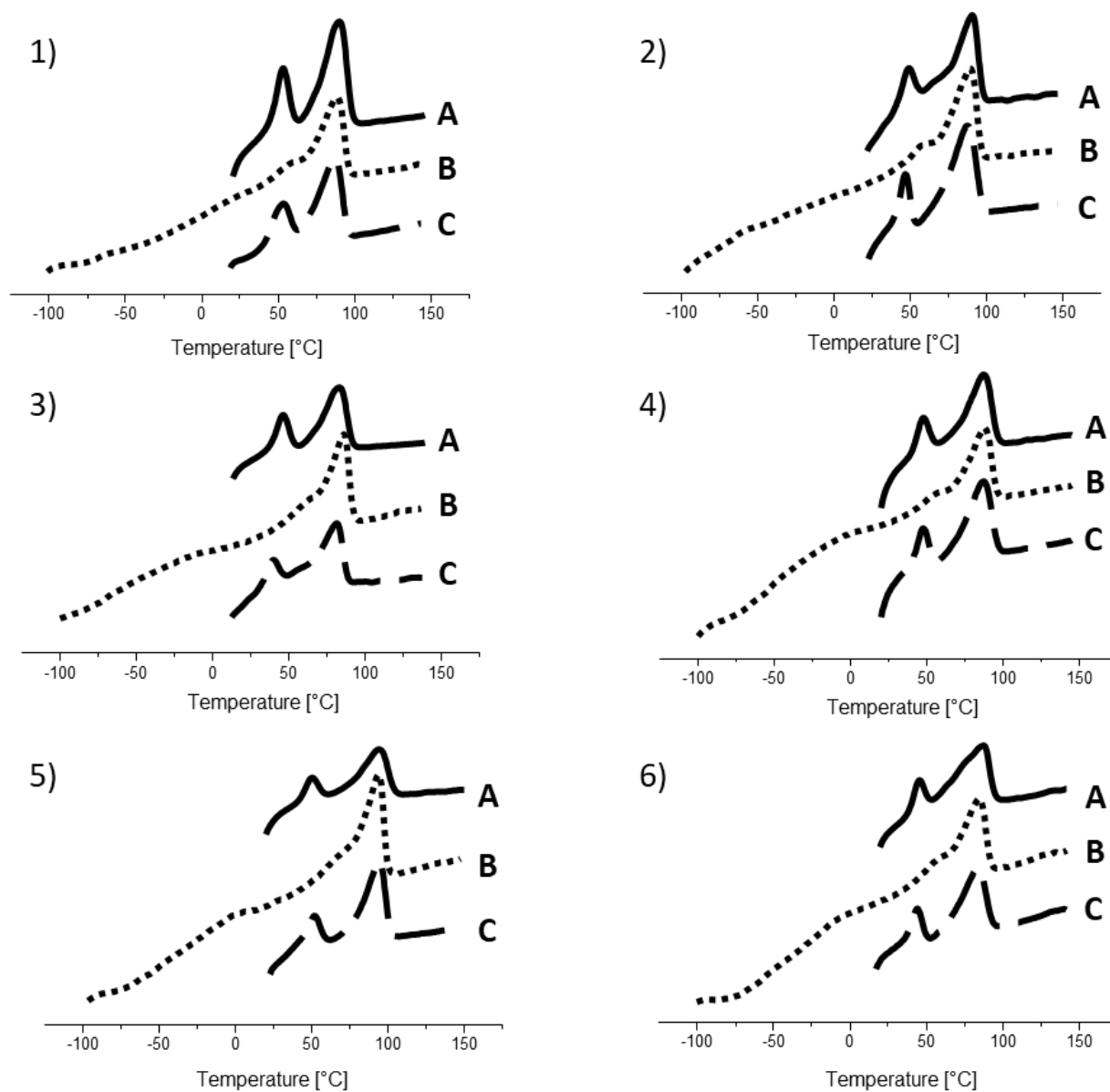


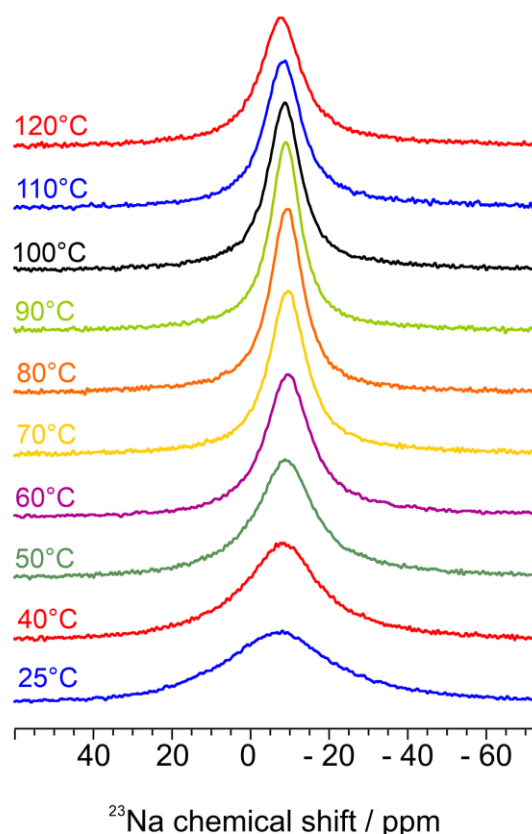
**Figure 3.** DSC scans of Surlyn 9150 (Zn) and Surlyn PC2000 (Na), and their blends with EPDM measured with heating rate 10 °/min. Left column: Surlyn 9150, right column: Surlyn PC2000. Diagrams 1) and 2) at the top represent the pure ionomer, diagrams 3) and 4) in the middle row represent the blends with EPDM, and diagrams 5) and 6) at the bottom are for the DCP-crosslinked blends with EPDM. In each diagram, the top trace belongs to the sample as prepared and stored for several days at room temperature (A). The traces in the middle belong to samples that have been heated to 150 °C and cooled down (10 °/min) to -100 °C prior to the measurements (annealing time below  $T_i < 10$  min) (B). The traces in the bottom belong to samples that were heated to 150 °C and annealed for 8 h at room temperature prior to measurements (C).

---

## Investigation of the obtained samples by $^{23}\text{Na}$ -NMR and $^{13}\text{C}$ -NMR spectroscopy

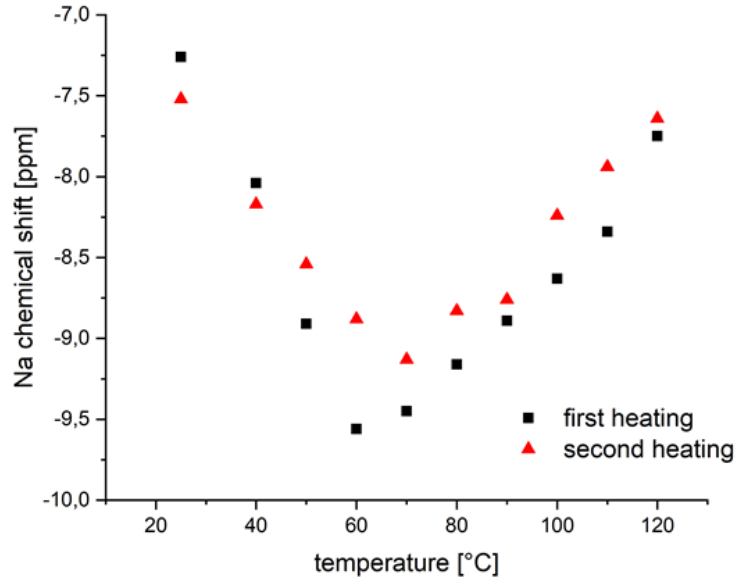
In order to obtain further insight into the structure and dynamics of the ion pair clusters, we measured solid-state  $^{23}\text{Na}$ -NMR spectra of the three samples listed in Table 1 (samples 1, 2, 4 and 5).  $^{23}\text{Na}$ -NMR spectra of styrene ionomers allowed to distinguish signals of isolated ions, hydrated ions and aggregated ions.<sup>22</sup>  $^{23}\text{Na}$  Magic-Angle-Spinning (MAS) of sodium methacrylate-ethylene ionomers have been reported to show only a broad peak with a maximum at -10 to -12 ppm that was assigned to aggregated ions, indicating rather complete participation of the  $^{23}\text{Na}$  ions in ionic aggregates.<sup>17,23</sup> We have been interested in whether and how the hydrophobic matrix and in particular the blending with EPDM affects the ionic cluster formation at temperatures below and above  $T_i$  as well as above  $T_m$ .

Figure 4 depicts the temperature dependence of the  $^{23}\text{Na}$  NMR spectrum of the Surlyn PC2000 sample. The NMR peak narrows when the temperature is raised to 100 °C but broadens again at further elevated temperature.



**Figure 4.** Variable temperature  $^{23}\text{Na}$  NMR spectra of Surlyn PC2000 measured upon heating.

In Figure 5, we plotted the temperature dependence of the  $^{23}\text{Na}$  chemical shift (maximum of the Lorentzian fit) of Surlyn PC2000 relative to sodium chloride in water. Below  $T_i$ , the signal shifted towards higher field, but the shift was reversed above  $T_i$ . Generally, an upfield shift corresponds to increased shielding of the nucleus by the surrounding electrons. Taking into account that the  $T_i$ -transition became more pronounced in the DSC scans when the sample was annealed below  $T_i$ , we consider the upfield shift an indication of an improved packing of the ion pairs to quadrupoles and higher aggregates, as it is expected from annealing of the clusters. Correspondingly, the downfield shift above  $T_i$  would be in agreement with some loosening of the clusters, which proceeds even further above  $T_m$ . When the sample was not aged for days before measuring the temperature dependence for a second time, the V-shaped dependence is less pronounced indicating a lesser densification. Hence, the observation agrees well with the explanation of the  $T_i$  transition as a kind of glass transition of the ionic clusters.



**Figure 5.** Temperature dependence of the  $^{23}\text{Na}$  NMR chemical shift (maximum of the Lorentzian fit) of Surlyn PC2000 relative to sodium chloride in water. First heating: sample aged for several days, in the second heating, the sample was measured directly after cooling from 120 °C.

The line widths of the signals in Figure 4 and their changes at raising temperature demonstrate motional narrowing caused by mobility within the clusters on the scale of milliseconds, i.e. the line width reduces from 4100 Hz at 25 °C to 1260 Hz at 90 °C.

Figure 6 shows the logarithmic dependence of the half height line width  $\Delta\nu_{1/2}$  of the  $^{23}\text{Na}$  NMR signal versus  $1/T$  (Arrhenius plot) between 25 and 120 °C: First heating: sample as aged for several days, second heating: sample was measured directly after cooling from 120 °C. For temperatures between 25 and 80-90 °C the data can be approximated linearly with a positive slope. The observation is in agreement with a continuous increase in mobility within the ionic clusters that cause motional narrowing. Molecular processes that are responsible for the motional narrowing include positional exchange of ion bound water and the sodium ions itself. The insert in Figure 6 shows a fit of the data between 25 °C and 80 °C to the Eyring equation (1).

$$\ln\{\Delta\nu_{1/2}T\} = \frac{k_B}{h} - \frac{\Delta S^\ddagger}{R} + \frac{\Delta H^\ddagger}{1000R} \frac{1000}{T} \quad (1)$$

The positive slope was calculated to a normalized activation enthalpy of  $\Delta H^\# / R = 1910$  K and an activation enthalpy of  $\Delta H^\# = 15.9$  kJ mol<sup>-1</sup> for the exchange and reorientation processes that are responsible for the line narrowing.

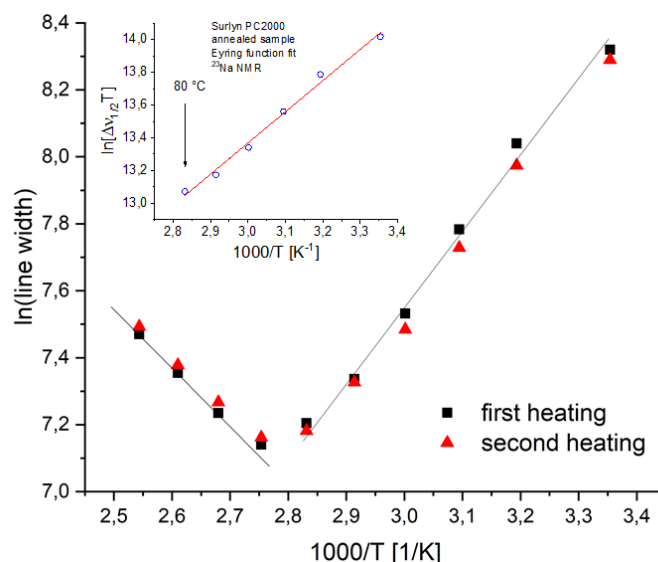


**Figure 6.** Logarithmic plot of the half height line width  $\Delta v_{1/2}$  of the <sup>23</sup>Na NMR signal versus 1/T (Arrhenius plot) for Surlyn PC2000. The change from a positive slope for temperatures between 25° and 80 °C to a negative slope for temperatures between 90 and 120 °C indicates a critical change in the structure and dynamics in the temperature range where also the  $-(CH_2-CH_2)_n-$  segments melt. The insert displays a fit of the data from first heating between 25° and 80° C according to the Eyring function. The positive slope of the straight line corresponds to  $\Delta H^\# / R = 1910$  K and an activation enthalpy of  $\Delta H^\# = 15.9$  kJ/mol.

When the temperature was raised further above the melting of the  $-(CH_2-CH_2)_n-$  segments, the temperature dependence of the line width changed critically and the signals became broader again. Within this temperature regime, the polymer chains gain additional mobility as the crosslinks by the crystallites of the  $-(CH_2-CH_2)_n-$  segments are released. We associate this with the onset of ion pair hopping between the clusters, which was largely suppressed at lower temperatures by the crystallite network. In this case, the broadening of the <sup>23</sup>Na-NMR signals is explained by the release of the confinement, which allows the ion-pairs to interact in an expanded chemical surrounding. Certainly, the data indicates that the ion pair clustering is significantly affected by the structure of the hydrophobic matrix itself as well.

This influence of the matrix becomes also evident, when the pure Surlyn PC2000 is compared with its blend with EPDM. The EPDM/Surlyn blends studied here were prepared with a propylene rich EPDM which does not form crystals. Correspondingly, the total fraction of crystallites in the blends is reduced compared to pure Surlyn PC2000 (Table 1). Figure 7 and Figure 8 summarize the  $^{23}\text{Na}$ -NMR of the blend Surlyn PC2000/EPDM 70/30 and of the same blend that was crosslinked above  $T_m$  by addition of a small amount of dicumlyperoxide, Surlyn, PC2000/EPDM 70/30 + 0.5 wt% DCP.

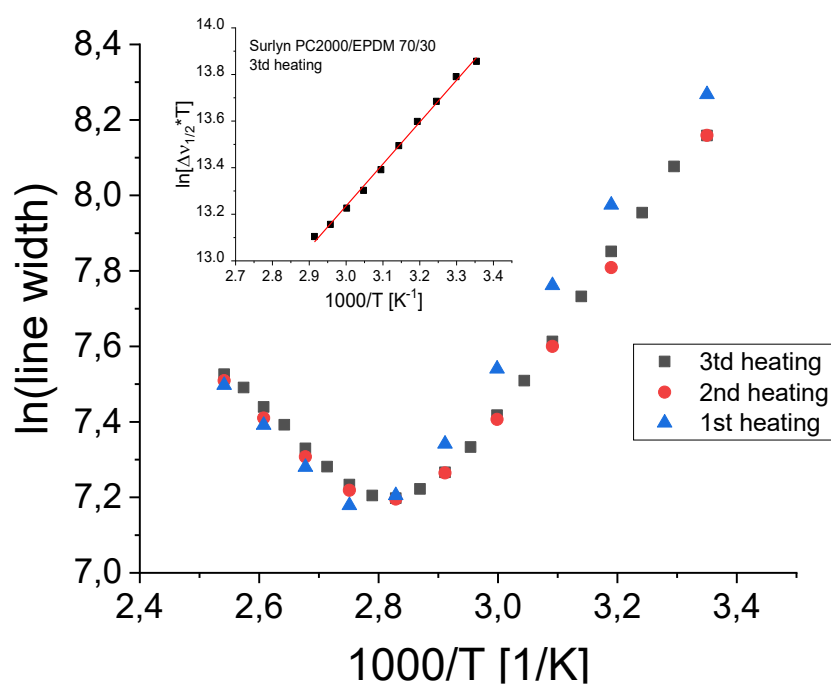


**Figure 7.** Logarithmic plot of the half height line width  $\Delta v_{1/2}$  of the  $^{23}\text{Na}$  NMR signal versus  $1/T$  (Arrhenius plot) for a 70/30 Blend of Surlyn PC2000 with EPDM. The insert displays a fit of the data between  $25^\circ$  and  $80^\circ$  C according to the Eyring function. The positive slope of the straight line corresponds to  $\Delta H^\ddagger/R = 1800$  K and an activation enthalpy of  $\Delta H^\ddagger = 15.0$  kJ/mol.

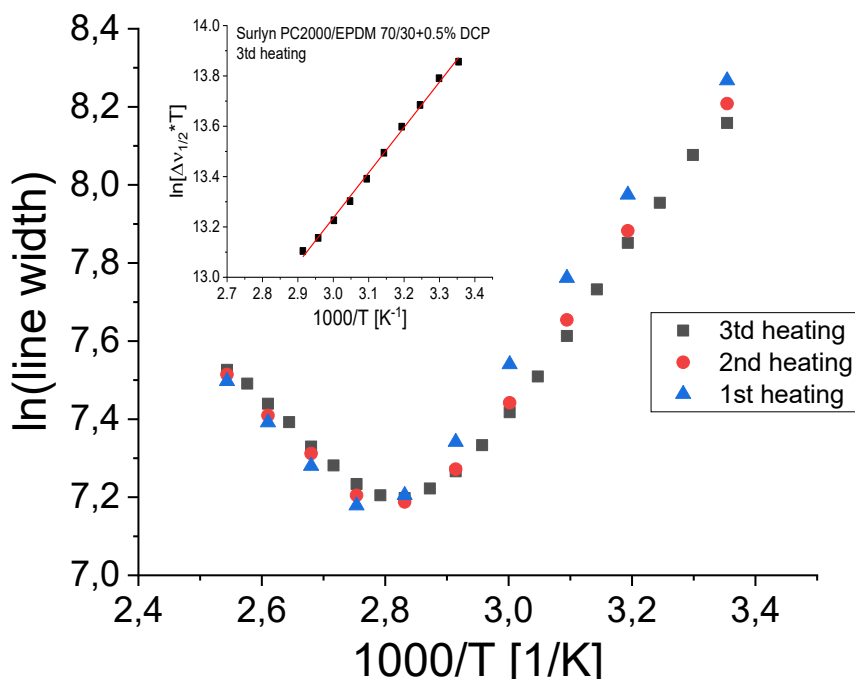


**Figure 8.** Logarithmic plot of the half height line width  $\Delta\nu_{1/2}$  of the  $^{23}\text{Na}$  NMR signal versus  $1/T$  (Arrhenius plot) for a 70/30 Blend of Surlyn PC2000 with EPDM that was crosslinked at elevated temperature with dicumylperoxide. The insert displays a fit of the data between 25° and 80° C according to the Eyring function. The positive slope of the straight line corresponds to  $\Delta H^\ddagger/R = 1800$  K and an activation enthalpy of  $\Delta H^\ddagger = 15.0$  kJ/mol. Line width

Table 2 summarizes line width and the activation enthalpy values which we calculated from the positive slope of the  $\ln(\Delta\nu_{1/2})$  values below  $T_m$  for all three samples, pure Surlyn PC2000, the blend with EPDM, and the blend with crosslinked EPDM. As it is also shown in Fig. 5-7, that the line width values decrease slightly but consistently for all samples at ambient temperature, when the samples have been cooled down from the melt without further annealing (2<sup>nd</sup> and 3<sup>rd</sup> heating). We also observe small reductions of the line width in  $^{23}\text{Na}$  NMR spectra of the blends with EPDM at 25°C compared to pure Surlyn PC2000. These observations support that the mobility of the sodium ions is restricted by the formation of  $-(\text{CH}_2-\text{CH}_2)_n-$  crystallites as well as by ageing below  $T_i$ . Such differences vanished, when the samples were heated above  $T_i$ , and all three samples yielded  $^{23}\text{Na}$ -NMR signals with the same width within the error margin. The Eyring fit of the temperature dependence of the line width in the range between 25 and 80 °C yielded values of  $15.9$  kJ/mol<sup>-1</sup> for the pure Surlyn and  $15.0$

$\text{kJ/mol}^{-1}$  for the blends. These values do not differ significantly when one takes into account the annealing effect. At most, the values support that the dilution of the hydrophobic matrix around the ionic clusters by EPDM eases the ion mobility slightly.

**Table 2.** Line width and the activation enthalpy values of pure Surlyn PC2000, the blend with EPDM, and the blend with crosslinked EPDM

	Sample preparation	$\Delta v_{1/2}$ (25°C) [Hz]	$\Delta v_{1/2}$ (60°C) [Hz]	$\Delta v_{1/2}$ (90°C) [Hz]	$(\Delta H^+ / R)$ [K]	$\Delta H^\#$ [kJ/mol <sup>-1</sup> ]
Surlyn PC2000	1 <sup>st</sup> heating	4100	1870	1260	1910	$15.9 \pm 0.5$
	2 <sup>nd</sup> heating	-	--	--	--	
Surlyn PC 2000/EPDM 70:30	1 <sup>st</sup> heating	3810	1800	1360	1860	$15.0 \pm 0.5$
	2 <sup>nd</sup> heating	3490	1650	1360	1740	
	3 <sup>rd</sup> heating	3490	1670	1390	1800	
Surlyn PC2000/EPD M 70/30 + DCP.	1 <sup>st</sup> heating	3890	1880	1380	1800	$15.0 \pm 0.5$
	2 <sup>nd</sup> heating	3670	1710	1350	1840	
	3 <sup>rd</sup> heating	3830	1850	1340	1800	

Finally, we want to note the pronounced effect on the line widths of the spectra by the uptake of water within the clusters. This is demonstrated by the ambient temperature line widths, which we measured for samples that were soaked for 7 days in water in order to saturate the ionic clusters. The line widths of the  $^{23}\text{Na}$ -NMR signals resulted in 1100, 1260, and 1450 Hz for Surlyn PC2000, its blend with EPDM and the crosslinked blend, respectively. Without water, a comparable narrowing was only observed when the temperature was raised to 90 °C. Because of the hydrophobic nature of the matrix and the selective adsorption of water in the ion clusters, we consider this as evidence that the line narrowing below  $T_m$  is mostly caused by the internal mobility within the clusters, either by raising the temperature or by water solvation of the ionic groups. Clearly, the plastifying effect of water leads to faster sodium clusters dynamics.

Thus, below  $T_m$ , ion mobility is largely restricted to exchange processes within the ionic clusters evidenced by motional narrowing of the signal. Continuous

---

increase of motional narrowing below and above  $T_i$  or by plastisizing water is in agreement with a glass transition of the ionic clusters and the thermal effect may be explained, at least partly, by enthalpy relaxation. This does not exclude some coincidence with the melting transition of imperfect PE crystals, that contributes further to the heat effect at  $T_i$ . Comparison with DSC and SAXS experiments demonstrates some competition between assembly of ion clusters and crystallization of  $-(\text{CH}_2\text{-CH}_2)_n-$  segments. Ageing of the samples at room temperature allows improved vitrification of the ions within the clusters. In turn, ageing of the samples above  $T_i$ , enables improved crystallization of  $-(\text{CH}_2\text{-CH}_2)_n-$  segments on the expense of the ion assembly. Depending on the extent of the confinement by the crystallites, the ion cluster vitrification can get largely suppressed. Only above  $T_m$ , when the  $-(\text{CH}_2\text{-CH}_2)_n-$  crystallites are molten and the confinement is terminated, ion mobility including ion hopping between clusters and broadening of the structural variety of ion clusters can develop fully. The observation that the ion mobility was slightly improved by the blending with EPDM even when the hydrophobic matrix had been crosslinked indicated vast mixing of the amorphous components.

### **Examination of the obtained samples by $^{13}\text{C}$ -NMR spectroscopy**

As mentioned above, the  $T_i$  has its origin in the onset of mobility of the ionic groups, which allows improved crystallization of  $-(\text{CH}_2\text{-CH}_2)-$  segments. For the ionic clusters, this is shown by the linewidth of the  $^{23}\text{Na}$ -NMR-signals. For the structure of the matrix around such clusters,  $^{13}\text{C}$ -NMR spectra can give complementary information based on the chemical shift of methylene groups, which can be distinguished for crystalline and amorphous  $-(\text{CH}_2\text{-CH}_2)-$  segments due to the sensitivity of the NMR relaxation times on molecular dynamics. Figure 9 shows the  $^{13}\text{C}$ -NMR spectra of the Surlyn PC2000 ionomer and its blends with EPDM. The spectra measured under MAS CP conditions

(Figure 9: 1 and 2) do not differ below and above  $T_i$ . The assignment of the signals is given in the figure, with the most prominent signals at 31.1 and 32.9 ppm belonging to the longer  $-(CH_2-CH_2)-$  segments in the amorphous and the crystalline state, respectively. Because cross-polarization is sensitive to the mobility of the methylene groups, the signal intensities cannot be used to calculate the degree of crystallinity, and in order to prove the molecular mobility, we repeated the experiment with direct polarization and without MAS. The spectra 3) and 4) demonstrate a significant broadening of the signals and a main signal belonging to the amorphous  $-(CH_2-CH_2)-$  segments. A completely different situation is observed for the blends with EPDM in Figure 7, 5) and 6). Direct polarization without MAS yielded highly resolved lines with the main signal corresponding to amorphous  $-(CH_2-CH_2)-$  segments. We consider the well resolved narrow signals for the mixture without MAS as indication of the miscibility of both polymers in the amorphous phase. No difference was observed whether the samples were crosslinked by DCP or not.

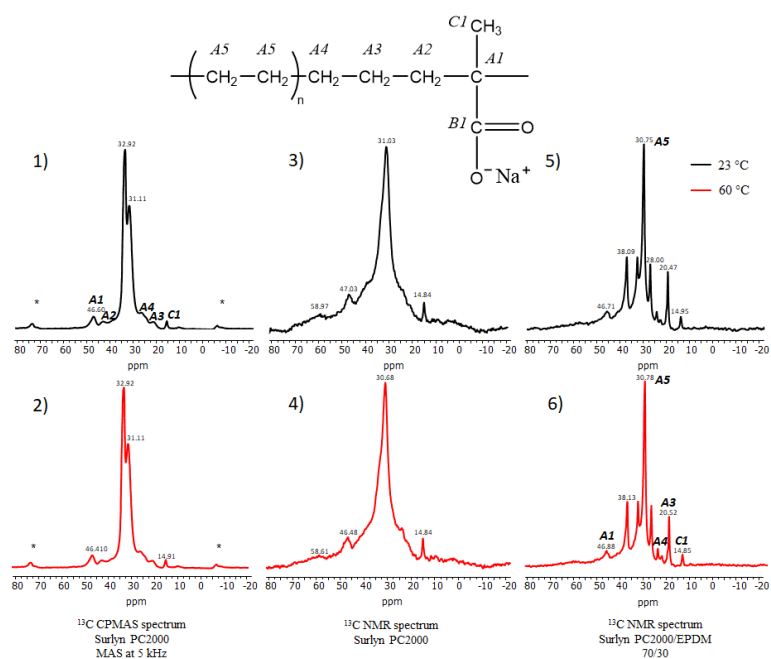
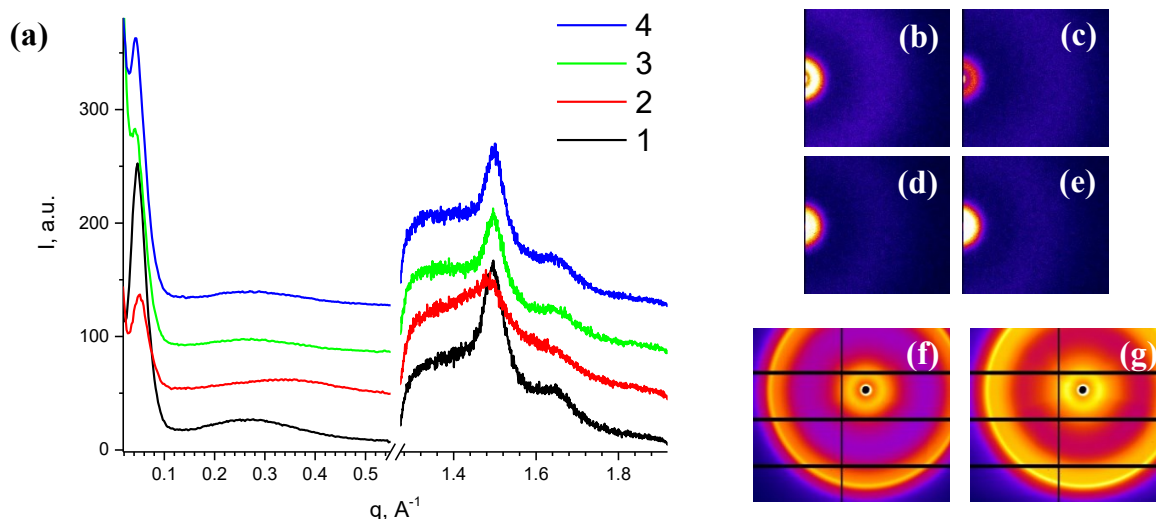


**Figure 9.**  $^{13}C$ -NMR spectra of Surlyn PC2000, 1) - 4), and its blend with EPDM, 5), 6), measured below (room temperature, black) and above (60°C, red)  $T_i$ . Spectra 1) and 2) were measured with CP-MAS, spectra 3) – 6) were measured with direct polarization and long delay times between pulses (30 s). The assignments of the signals are given on the top.

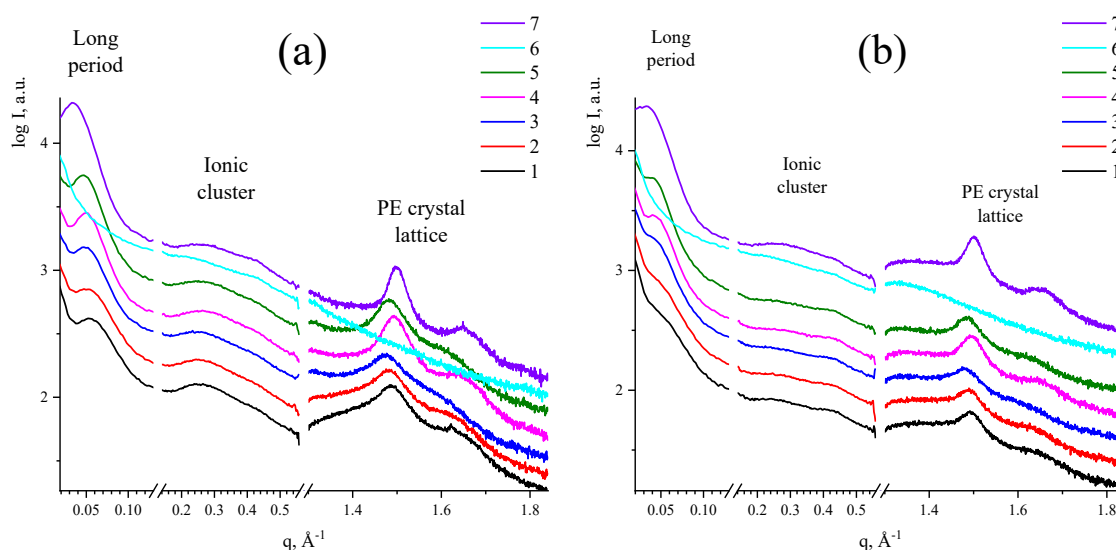
---

## Investigation of the obtained samples by X-ray diffraction

Further characterization of the ionomer blends was done by X-ray diffraction studies at varied sample temperature. Figure 10 shows the small- and wide-angle diffraction of films of Surlyn and Surlyn/EPDM composites: (1) Surlyn 9150, (2) Surlyn PC2000, (3) Surlyn 9150/EPDM, and (4) Surlyn 9150/EPDM crosslinked with 0.5 wt% DCP. We observed the same structural features for all three samples: wide-angle diffraction peaks for the 110 and 200 reflection for the crystalline  $-(\text{CH}_2-\text{CH}_2)-$  segments, a broad peak for the ion clustering at  $q \approx 0.26$  for Surlyn 9150 and at  $q \approx 0.35$  for Surlyn PC2000, and a well resolved SAXS peak at  $q \approx 0.06$ , which we assigned to a 11 nm period of the stacked crystal lamellae of the  $-(\text{CH}_2-\text{CH}_2)-$  segments. Exchange of the counter ions from  $\text{Na}^+$  to  $\text{Zn}^{2+}$  did not lead to substantial changes in crystallite structure. However, the long period at 90 Å the WAXS reflections became more blurred. Only the ionic cluster peak position changed to  $0.34 \text{ \AA}^{-1}$  (vs.  $0.25 \text{ \AA}^{-1}$  for Surlyn 9150 ionomer films). The comparison demonstrates that the ion cluster organization remained in the crosslinked EPDM blend of the ionomer. The fact that the crosslinked blends yielded broader (diffuse) small-angle peaks demonstrates a less well-developed structural organization of the ionomer clusters and crystallites from longer  $-(\text{CH}_2-\text{CH}_2)-$  segments. The 2D SAXS and WAXS diffraction patterns demonstrate an isotropic orientation of the respective structures within all sample



**Figure 10.** (a) combined SAXS-WAXS curves from bottom to top for Surlyn 9150 ionomer film (1), for Surlyn PC2000 (2), Surlyn 9150/EPDM (3) and Surlyn 9150/EPDM crosslinked mixtures (0.5 wt% DCP) (4) annealed at 120 °C for 20 min. The blend fractions were 14:6 by weight. Curves given in logarithmic scale and shifted vertically for clarity. (b)-(e) corresponding 2D SAXS diffraction patterns. (f),(g) 2D WAXS data for Surlyn 9150 and Surlyn 9150/EPDM/DCP blended films.



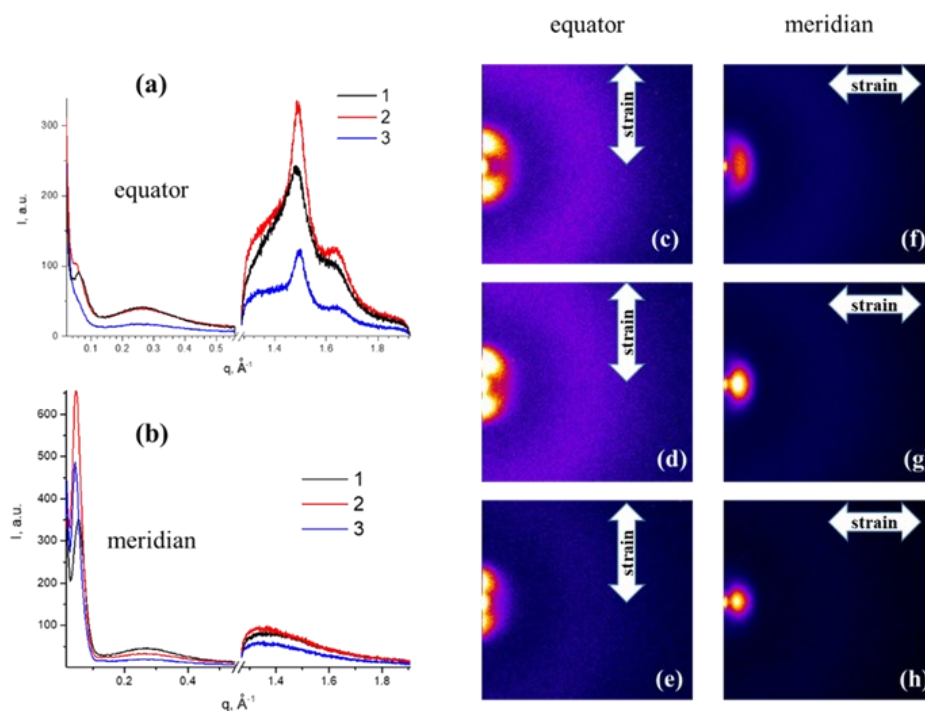
**Figure 11.** Temperature dependent SAXS-WAXS curves for Surlyn 9150 ionomer film (a), and the crosslinked Surlyn 9150/EPDM blend (b). Temperatures from bottom to top are 1: 20 °C, 2: 40 °C, 3: 60 °C, 4: after first cooling at 20°C, 5: second heating at 60 °C, 6: second heating at 100 °C and 7: after cooling from 100 °C to 20 °C. Curves are given in logarithmic scale and shifted vertically for clarity.

Figure 6 depicts temperature dependent changes of the WAXS/SAXS pattern of the pure Surlyn 9150 (a) and its crosslinked 14:6 (by weight) blend with EPDM (b). When the samples were heated above  $T_i$ , the small angle reflections assigned to the long period of stacked PE crystallites shifted towards smaller angles and

---

the wide-angle reflection became sharper. This improvement of the ordering of longer  $-(\text{CH}_2-\text{CH}_2)-$  segments remained when the samples were cooled to  $20^\circ\text{C}$ . Subsequent heating to  $120^\circ\text{C}$  resulted in complete melting of the PE crystallites, the corresponding small- and wide-angle peaks disappeared completely. In contrast, the ionic SAXS peak remained. Cooling the sample from  $120^\circ\text{C}$  to room temperature resulted in the recovery of the original SAXS/WAXS pattern. The crystal structure restored with an even larger long period of  $180\text{ \AA}$ . The ionic cluster structure restored as well.

In addition to the information on the structural organization of the relaxed samples in Figure 10 and 11, we performed SAXS and WAXS measurements to investigate the changes that occur when the sample got stretched at ambient temperature, i.e., below  $T_i$  and  $T_m$ . Figure 12 a and b depict equatorial and meridional scans and the corresponding 2D patterns of the uniaxially stretched samples with indication of the stretching direction. Samples were prepared by injection moulding and stretched to different extent ( $\varepsilon \approx 150\%$  for Surlyn 9150,  $\varepsilon \approx 110\%$  for Surlyn 9150/EPDM,  $\varepsilon \approx 70\%$  for crosslinked Surlyn 9150/EPDM). The long period  $110 - 120\text{ \AA}$  is most distinct in the meridional direction, indicating parallel orientation of the lamellae with respect to the stretching direction. Correspondingly, the WAXS reflections are observed only in the equatorial scans. Most important is the observation that the ionic peak at  $0.26\text{ \AA}^{-1}$  did not show any anisotropy but weakened considerably, in particular for the crosslinked blend. The significant difference in intensity can be explained by large deformation and destruction of the ionic cluster either upon cold stretching or by small cuts.



**Figure 12.** Combined SAXS-WAXS curves for stretched Surlyn 9150 ionomer film (1), Surlyn 9150/EPDM mixture (2) and Surlyn 9150/EPDM mixture crosslinked with 0.5 wt% DCP (3) in equatorial (a) and meridional (b) directions. 2D SAXS images for deformed Surlyn 9150 along equator (c) and meridian (f), Surlyn 9150/EPDM along equator (d) and meridian (g), Surlyn 9150/EPDM/DCP along equator (e) and meridian (h). Stretching direction is marked.

### 3.2.3. Assessment of the efficiency of the self-healing processes in the obtained specimens

To evaluate shape recovery after large deformations of the crosslinked ionomer/EPDM blends, samples were studied after deformation and subsequent heating to 120 °C. At this temperature, the  $-(\text{CH}_2-\text{CH}_2)_n-$  segments are molten and the recovery can be effected by the relaxation of the covalent as well as of the ion-cluster network. Figure 8 a shows photographs of a bone shaped test specimen of the crosslinked Surlyn 9150/EPDM blend, that was stretched to  $\varepsilon = 630\%$  and kept in the deformed state for 12 h before it was annealed at 120 °C for 15 min. The sample was taken as received by hot pressing. This means that the internal

---

structure, i.e., ionic cluster organization, as well as the processing-caused deformation of the covalent network, was not equilibrated. The sample recovered fully in length from originally 30 mm to 29 mm. However, when the sample was subsequently stretched to break, we observed significant weakening of the structure corresponding to a reduction in strain at break by 50 % and a nearly 30 % reduced tensile strength. WAXS pattern show the uniaxial orientation by strain and the recovery of the isotropic crystallite arrangement after melting and cooling. When the same experiment was repeated with pure Surlyn 9150, instead of the crosslinked blend with EPDM, we observed a similar weakening of the mechanical properties, but the original shape of the sample (length) was only partially recovered to 37 mm (initial value: 30 mm). In both cases, the recrystallization of the  $-(\text{CH}_2-\text{CH}_2)_n-$  segments appeared to be impeded as shown by the weak WAXS pattern.

As a conclusion from this data, we consider significant contributions to the macroscopic shape recovery by the covalent network, but additionally also by the reorganization of the ionic cluster structure. Hence, we repeated the experiment with careful attention to the annealing, i.e. optimization of the cluster formation before cold deformation. Figure 13 b shows the stress-strain results of the recovery experiment for the same sample preparation like in Figure 13 a, with the difference that the sample had been annealed for 3 h at 120 °C before deformation in order to improve the ion cluster organization and that the sample remained a

reduced amount of time in the strained state. In this case, the subsequent “healing attempt” by heating the sample for 15 min to 120 °C yielded not only nearly full recovery of the original length (30.6 mm) but also much better restoration of the original mechanical properties (with respect to the experiment in Figure 8 a): the deformation at break recovered to  $\epsilon = 299\%$ , versus  $\epsilon = 277\%$  originally, the strength at break to 14.4 MPa versus 11.3 MPa, and the modulus to 78,5 MPa from 95.1 MPa.

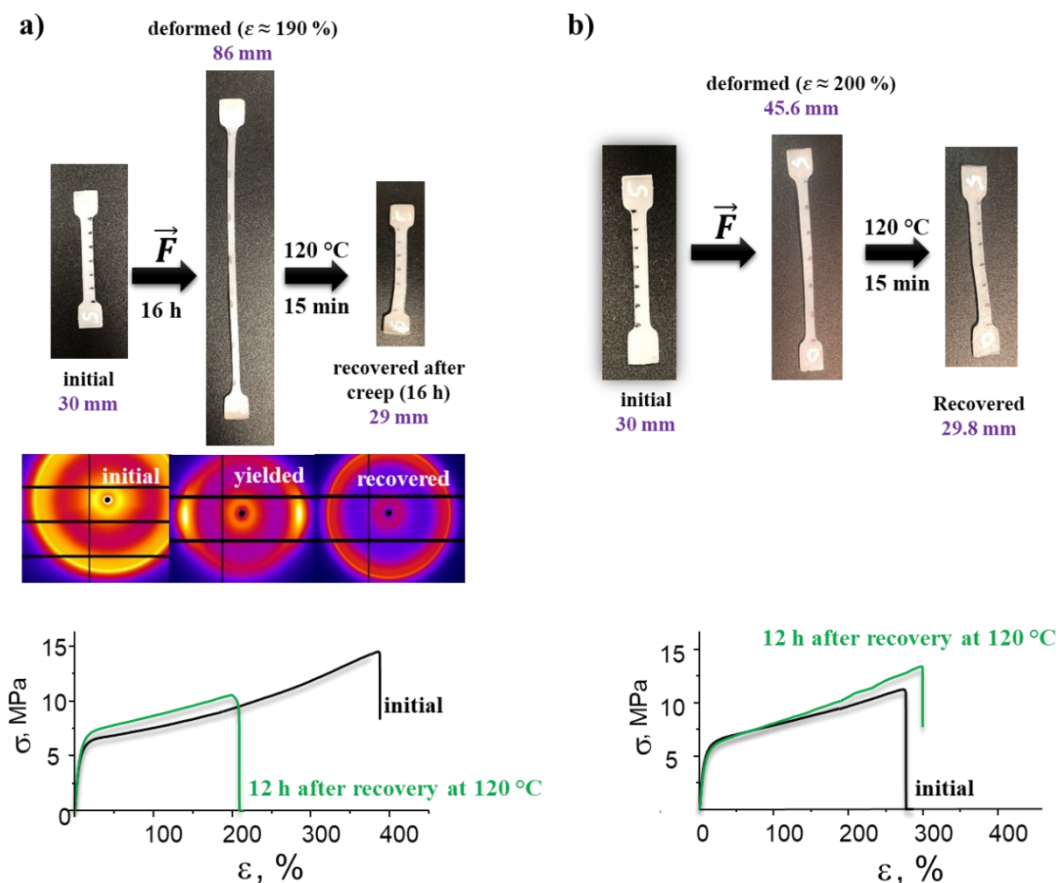


**Figure 13.** Recovery experiment of uniaxially stretched bone-shaped samples of crosslinked Surlyn 9150/EPDM blends. Left side (a): the sample was stretched as received by hot pressing, right side (b): the sample was annealed for 3 h at 120 °C before stretching in order to improve the equilibration of the ion cluster organization. The photographs depict the samples before deformation (left), after deformation in the cold-deformed state (middle) and after recovery at 120 °C for 15 min. Stress-strain curves show experiments for a sample as prepared and for a sample that been strained and subsequently “healed” by thermal treatment at 120 °C for 15 min. The comparison demonstrates significantly improved recovery when the structural organization of sample was initially equilibrated by thermal treatment.

In the following, we demonstrate self-healing experiments, which exploit the combination of the macroscopic structure regeneration by the shape memory effect with microscopic mending which is enabled by the recovery of the ionic cluster structure.

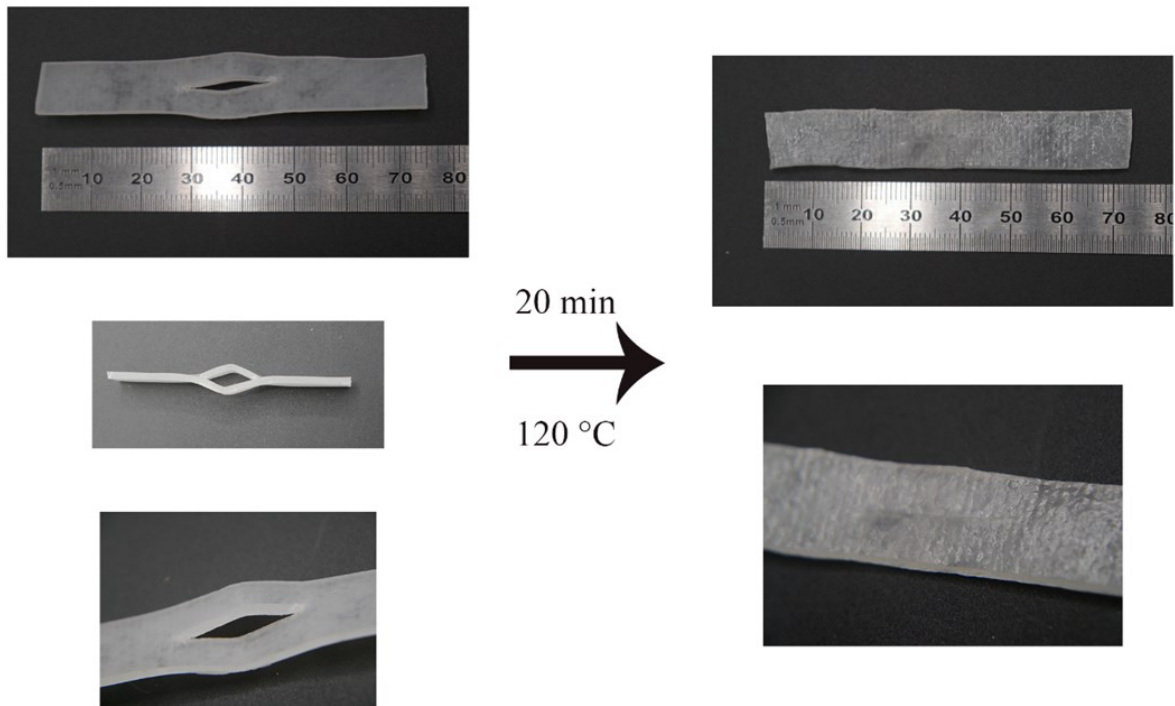


**Figure 14.** Healing of a large damage caused by cutting and subsequent cold large deformation. The ribbon was prepared from Surllyn PC2000/EPDM (70/30) crosslinked by 0.5 wt% DCP. The sample was prepared by the coprecipitation method and moulded by hot pressing (1 h – 80 °C, 2 h -110 °C, 20 min 190 °C,  $p = 10$  bar). Scale bar depicts mm.

Figure 14 depicts a ribbon sample in which a slit was cut by a sharp knife and then pulled apart. When the sample got heated for a short time to 120 °C, the flat shape recovered and the slit closed. Without crosslinking, we observed a widening of the slit. Most importantly, the two surfaces generated by the cut mended and could not be pulled apart.

The mending effect is shown in more detail in Figure 15, where we cut a slit into a disc-shaped sample from the center to the outer edge (Figure 10 d and b) and

observed practically complete healing when the sample was heated for 20 min to 120 °C.

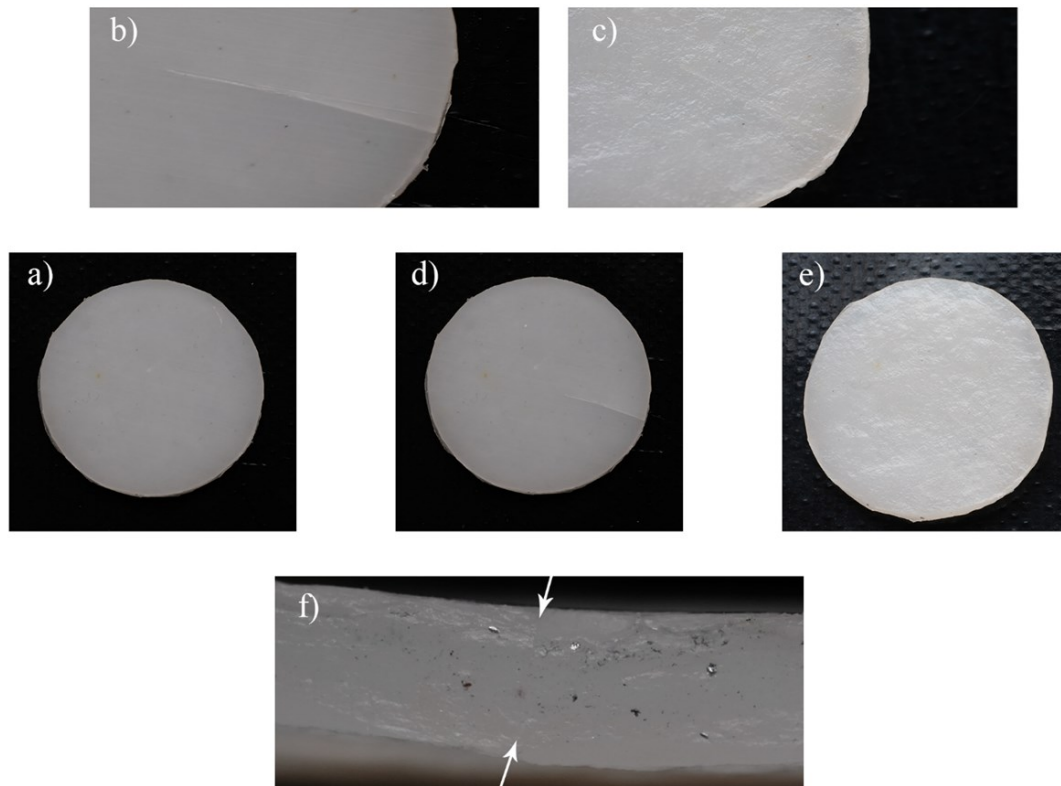


**Figure 15.** Self-healing test for a disc shaped sample of a Surlyn 9150/EPDM blend (coprecipitation preparation) that was crosslinked by DCP. a) sample as obtained by hot pressing (1 h – 80 °C, 2 h - 110 °C, 20 min 190 °C, p = 10 bar, diameter 25 mm, thickness 2 mm). d) a slit was cut from the center to the rim, b) enlargement of the cut. c), e) and f) demonstrate that the cut mended rather perfectly when the sample was heated to 120 °C for 20 min. Images c) and e) were taken after the sample cooled down to room temperature. f) depicts the edge on view on the cut after mending.

The data shows how a defect in the range of millimeters to centimeters can be repaired by the stress that has been caused by the defect formation. The principle of this large defect healing involves a hierarchy of deformations and defects: (i) deformation and rupture of ionic clusters on the atomic scale, (ii) reorientation and deformation of polymer crystallites on the submicron scale, and (iii) entropy elastic deformation of a polymer covalent network on the macroscopic scale. Each mechanism stores stress at its particular length scale. The covalent network contributes mostly to the macroscopic shape recovery, while the ionic clusters try to recover their structural relaxation on the nanometer scale. The crystals play a

---

dual role. On the one side, they contribute to healing, when they reconstitute their arrangement as in the original material, on the other side they deform plastically and prevent early stress-relaxation until the temperature raised above their melting point.

---

### 3.3. Conclusions

We have demonstrated that combination of different crosslinks can contribute to large scale self-controlled mending. Although healing had to be triggered by a raise in temperature, mending has been driven entirely by the internal stress that was built up in the materials when the defect was generated. Strain recovery of the covalent network can affect restoration of the original macroscopic shape of an object as long as the damage of the network is not too extensive. Here we exploit, that even relatively large structural defects do not compromise shape memory abilities. The microscopic cohesive healing requires recovery of the cluster structure. However, only at elevated temperature, the ion pair clusters get dynamically weakened and get an increasingly transient character. Creep recovery and stress relaxation for poly(styrene-co-styrene sulfonate) ionomers have demonstrated ion pair association even at temperatures as high as 220 °C. Hence, the ion clusters can preserve the microscopic as well as the macroscopic structural memory for relatively long times. The fact, that the  $-(\text{CH}_2\text{-CH}_2)_n-$  crystallites deform plastically upon strain below  $T_m$  and arrest the state of deformation, enables us to control the time at which the healing will take place. The microscopic memory for cohesive healing is based on the reorganization of the ionomer clusters.

Within our concept, we do not only extend the rubbery plateau by crosslinking, but we also exploited the crystallization of the  $-(\text{CH}_2\text{-CH}_2)_n-$  segments in order to control the relaxation events from outside. Because the polyethylene crystallites plastically deform and orient, the deformation of the ionic clusters as well as deformation of the covalent network are retained as long as thy crystallite do not melt. Although the system performed according to these considerations, there is a room for further improvement. Even at the low degree of crystallization of 10-14%, crystal formation and ion-cluster organization work against each other, so ion-pair clustering is not optimum and depends very much on the thermal history

---

of the samples. Good results can only be obtained with samples that have been annealed at room temperature. Improvement should be possible by tailoring the crystalline component as well as the ionic aggregation.

Within the common classification regarding autonomous and non-autonomous self-healing, the system would not be called autonomous, because the healing effect was only observed at elevated temperature. This was the price paid for the easy control of the process, but it also enabled us to prepare a self-healing material that is not rubbery at ambient temperature. The crosslinked ionomer/EPDM blends, which we presented here, have a comfortable hard touch and might well be suitable for coatings.

---

### 3.4. Supporting information

#### Materials.

Surlyn PC 2000, partially neutralized by Na<sup>+</sup> (E-0.054MAA-0.3Na), and Surlyn 9150, partially neutralized by Zn<sup>2+</sup> (E-0.054MAA Zn), were obtained from DOW. EPDM (Keltan™ 13561C, 5.5% norbornene, 56% ethylene units) was obtained from ARLANXEO. Dicumyl peroxide ( $t_{1/2} = 10$  h at 114 °C) was used as received from Sigma-Aldrich.

#### Samples preparation

##### **Blending Surlyn and EPDM by premixing the components in solution and subsequent precipitation and moulding.**

At a temperature of 65 °C, 14 g of Surlyn PC2000 or Surlyn 9150 were dissolved in 380 mL of a mixture of butanol-1 and toluene (1: 9) and mixed with a mixture of 6 g of EPDM in 40 mL of the same solvent mixture to yield a clear ~5 wt% solution. An amount of 30 mg of dicumyl peroxide (DCP) (0.5 wt% from EPDM) was added to the 70/30 weight % ionomer-EPDM solution. Afterwards the warm solution was added slowly to 1.5 L of methanol containing 15 % water. The coprecipitated polymers were collected by filtration and dried at 60 °C under vacuum overnight (see Figure S1 of *Supporting information*).

The dried coprecipitate was moulded to discs with a diameter of 25 mm by means of a temperature controlled vacuum press (MeltPrep GmbH, Gratz, Austria). For larger samples preparation a P200S-VAK press (Vogt Labormaschinen GmbH, Berlin, Germany) was used. The moulding procedure comprised two steps. In the first step, vacuum was applied, then the temperature was raised to 80 °C and then a pressure of 1.7 bar was applied. After 1 h, the temperature was raised further to 110 °C, while the pressure was maintained at the same level. After 2 h the sample

---

was cooled to room temperature and removed from the mold. With the Vogt press, a similar procedure was used, except that the pressure was increased to 10 bar before raising the temperature to 110 °C. For the samples, containing DCP, temperature was raised to 190 °C for 20 min to ensure crosslinking before cooling it to room temperature. Figure S2 of *Supporting information* depicts a disc of the Surlyn 9150 / EPDM blend crosslinked by DCP prepared by this procedure. Left image of Figure S2 shows the partially crystalline, fully relaxed sample as removed from the mold. The image on the right depicts the sample at 110 °C where it became entirely clear. The shrinkage in diameter caused by the annealing was less than 2 % indicating that the structure equilibrated during moulding.

### **Melt-Blending of Surlyn and EPDM and test specimen preparation by injection moulding.**

A co-rotating twin-screw micro compounder with conic screws and a volume of 15 mL (DSM Xplore, The Netherlands) was used as a reactor for mixing Surlyn PC2000 or Surlyn 9150 and EPDM in the melt. Surlyn and EPDM were fed together with 70/30 ratio into the microcompounder at a barrel temperature of 200°C under nitrogen. For crosslinking, dicumyl peroxide, DCP, was added to the melt (0.5 wt% from EPDM) with a screw rotation rate of 40 rpm for 10 min. Afterwards, the resulting copolymers were processed on a 5.5 mL injection moulding machine (DSM Xplore) into dog bone specimens with gauge length of 60 mm and thickness of 2 mm under the following conditions: cylinder temperature 200 °C, mold temperature 60 °C or 95 °C, holding pressure 7 MPa, holding time 10 s, and cooling time 20 s (or 1 min). When the samples were annealed outside of the mold for 10 min at 110 °C, they shrunk in length by 40%, when the mold temperature was set to 95 °C the shrinkage in length could be reduced to 18 % (Figure S3 of *Supporting information*). The shrinkage indicates insufficient relaxation in the mold.

---

## Characterization methods

### <sup>23</sup>Na NMR spectroscopy.

For the NMR experiments and if not specified differently in the discussion, samples were employed as stored at ambient conditions but not rigorously dried. NMR spectra <sup>23</sup>Na (I=3/2) were measured with a 11.8 T wide bore magnet system and a Bruker Avance III console operating at frequency of 132.32 MHz <sup>23</sup>Na Larmor frequency, equipped with a commercial static double-resonance probe for samples with 4 mm outer diameter. The temperature was changed in the interval from 25 - 120 °C and was maintained within  $\pm 0.1$  K during the individual measurements using a Bruker BSVT temperature control unit. All <sup>23</sup>Na NMR spectra were externally referenced to <sup>23</sup>Na signal of a 1 M aqueous NaCl solution at 25 °C. For all measurements a recycle delay of 2 s, and a 30 deg radio-frequency pulse for signals excitation with pulse length was 2  $\mu$ s (pulse power of 170 W) chosen, in order to ensure a quantitative signal excitation independent of possible local variations of the <sup>23</sup>Na quadrupolar coupling. The temperature dependent spectra were acquired with a dwell time of 2  $\mu$ s, 8192 data points in the time domain and 512 transients leading to 40 min measuring time for each temperature including 15 min thermal equilibration time prior to each measurement. The <sup>23</sup>Na ionomers spectra showed a single signal with lorentzian line shape. The spectral linewidth was determined by fitting the spectra using the DMfit software.<sup>24</sup> The temperature settings were calibrated using the temperature dependent <sup>1</sup>H chemical shift difference of the residual protons of methanol-d4 in order to account for minor deviation in the NMR setup using the calctemp AU program of the Bruker TopSpin software (version 3.6).

---

## **Carbon-<sup>13</sup>NMR.**

Spectra were recorded with wide bore AV700, and AVIII500 Bruker NMR spectrometers at <sup>13</sup>C frequency of 176.073 MHz, and 125.751 MHz with cross-polarization magic-angle sample-spinning (MAS) probe heads with 3.2 mm, and 4 mm ZrO rotors, respectively. For temperature variation, we used a Bruker temperature control unit (BCU 05) with temperature stability better than 1°C, that was calibrated by comparison with the temperature dependence of neat ethylene glycol chemical shift resonances.<sup>25</sup> Spectra were measured with non-rotating samples as well as with MAS and chemical shifts were externally referenced to adamantane. 4096 or 2024 scans were sampled with a recycle delay of 10 s, a radio-frequency pulse length of 2 μs, and a dwell time of 10 μs. 8k time domain data were filled to 16k. The time domain data were 8k and the zero filling was done with 16k. We employed the Hartmann-Hahn pulse sequence for <sup>1</sup>H-<sup>13</sup>C cross-polarization,<sup>26-28</sup> and set the strength of the <sup>13</sup>C radio frequency 60 W with the pulse length of 2 ms. Proton high-power decoupling was achieved by a spinal-64 pulse sequence with duration of 50 ms.<sup>28</sup> Because cross-polarization and the resulting signal intensity is affected by local dynamics and is thus non-quantitative, we employed in some experiments <sup>13</sup>C direct polarization.

## **Differential scanning calorimetry.**

Differential scanning calorimetry was performed using DSC 204 (Netzsch, Germany). Samples (typical weight: 10 mg) were placed in standard Netzsch 25 microliter aluminum crucibles. Metallic indium and palmitic acid were used as standards for temperature calibration. The heating and cooling rates were typically 10 K/min.

---

## **X-ray analysis.**

Small-angle and wide-angle diffraction patterns of high resolution were recorded using SAXS and WAXS camera S3-Micropix, manufactured by Hecus (CuK $\alpha$ ,  $\lambda = 1.542 \text{ \AA}$ ). Two detectors were employed: a two-dimensional Pilatus 100 K and a linear gas position sensitive detector PSD 50M operating at a pressure of 8 bar Ar/Me, the high-voltage and the current at the Xenocs Genix generator were set to 50 kV and 1 mA, respectively. For shaping the X-ray beam, Fox 3D vacuum optics were used. The slits in the Kratky collimator were set to 0.1 and 0.2 mm correspondingly. The angular scale was between  $0.003 \text{ \AA}^{-1}$  and  $1.9 \text{ \AA}^{-1}$ . Silver behenate and LDPE (Lupolen<sup>TM</sup>) were used as a reference and for calibration. To eliminate the influence of air, the X-ray optics system and camera were evacuated to  $2\text{-}3 \times 10^{-2} \text{ mm Hg}$ . The exposition time was varied between 600 to 3000 s.

## **Mechanical Tensile Tests**

Mechanical tests were performed on an Instron 5982 testing machine at room temperature with 50 mm/min deformation rate (cold deformation). Samples were either stretched until breakage or strained to an extension of  $\varepsilon = (l - l_0)/l_0$  of 300 %. When the samples were removed from the clamps directly after deformation, we observed a significant recovery, sometimes even exceeding two-thirds of the original deformation. When we kept the samples fixed in the strained state for at least 2 h, strain recovery was reduced significantly, as described in the Results and Discussion part for the respective samples.

## Experimental data

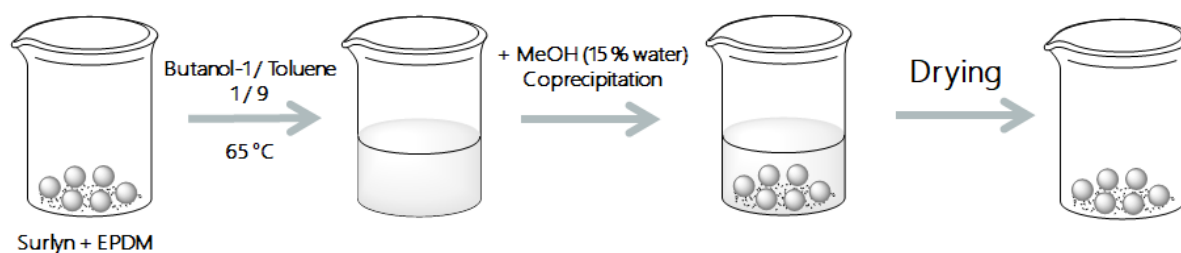


**Figure S1.** Dissolution and coprecipitation of a mixture of Surlyn ionomer and EPDM

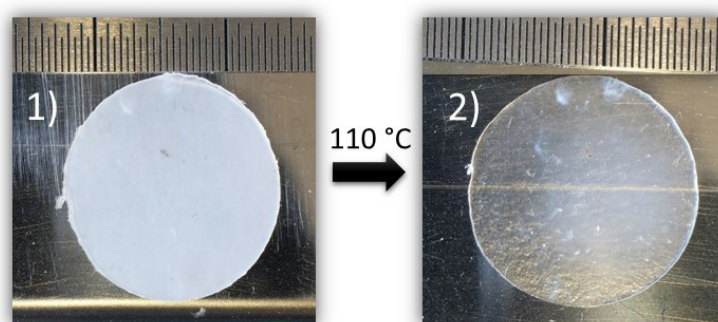


**Figure S2.** Disc of Surlyn 9150 / EPDM (70/30) blend ( $d = 16$  mm, thickness – 0.5 mm) that was crosslinked by 0.5 % DCP. Left image (1) at 23°C, right image (2) at 110°C. Sample was moulded for 1 h at 80°C at a pressure of 1.7 bar and subsequently heated for 2 h to 110 °C, and then 20 min at 190 °C. Blend was prepared by coprecipitation. Scale bar depicts mm.

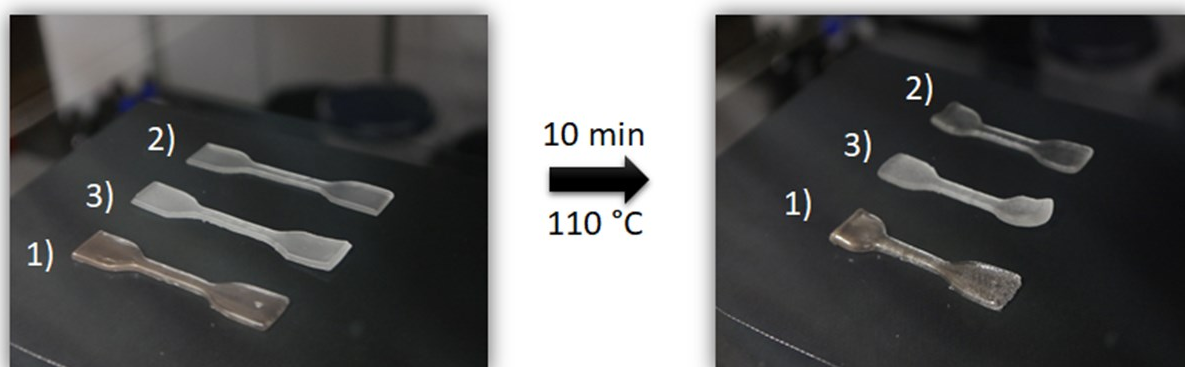


**Figure S3.** Injection moulded samples before and after temperature treatment at 110°C, mold temperature was 95°C, (1) Surlyn PC2000, (2) Surlyn PC2000/EPDM, (3) Surlyn PC2000/EPDM.

---

### 3.5. Acknowledgements

This research was conducted within the Max Planck School Matter to Life supported by the German Federal Ministry of Education and Research (BMBF) in collaboration with the Max Planck Society. The investigation was performed in part at the Center for Chemical Polymer Technology, supported by the EU and North Rhine-Westphalia (EFRE 30 00883 02).

### Contributions to the Chapter

Robert Graf carried out the  $^{23}\text{Na}$  NMR experiments. Prof. Demco executed  $^{13}\text{C}$  NMR, as well as needed calculations and with Alexandra Bystrova helped with manuscript corrections. In a group of Prof. Chvalun Nikita Sedush performed a cold deformation of the crosslinked polymer blends and Sergei V. Krashennikov obtained stress-strain curves for prepared samples. Artem Bakirov was responsible for all X-ray measurements. Prof. Dr. Martin Möller supervised this project.

Parts of this chapter were previously published as: **Selezneva E.V.**, Bakirov A.V., Sedush N.G., Bystrova A.V., Chvalun S.N., Demco D., Möller M., How Shape Memory Effects can Contribute to Improved Self-Healing Properties in Polymer Materials, *Macromolecules* **2021**, 54, 5, 2506–2517

**Selezneva E.V.**, Bakirov A.V., Sedush N.G., Chvalun S.N., Demco D., Möller M., How Shape Memory Effects can Contribute to Improved Self-Healing Properties in Polymer Materials, *IUPAC-MACRO2020+ The 48th World Polymer Congress* May 16-20, **2021** Jeju, Korea

Some content has been adapted accordingly.

---

## 3.6. References

- [1] Zhang, M. Q. & Rong, M. Z. *Polymer Chemistry* vol. 4 4878–4884 (2013).
- [2] Neuser, S., Michaud, V. & White, S. R. *Polymer (Guildf)*. **2012**.
- [3] Cohades, A. & Michaud, V. *Adv. Ind. Eng. Polym. Res.* 1, 66–81 **2018**.
- [4] Wan, T. & Chen, D. *J. Mater. Sci.* 52, 197–207 **2017**.
- [5] Jiang, Z. C., Xiao, Y. Y., Kang, Y., Li, B. J. & Zhang, S. *Macromol. Rapid Commun.* 38, 1–8 **2017**.
- [6] Behl, M. & Lendlein, A. *Mater. Today* **2007**.
- [7] Xiao, X., Xie, T. & Cheng, Y. T. *J. Mater. Chem.* **2010**.
- [8] Kalista, S. J., Ward, T. C. & Oyetunji, Z. *Mech. Adv. Mater. Struct.* 14, 391–397 **2007**.
- [9] Stukalin, E. B., Cai, L. H., Kumar, N. A., Leibler, L. & Rubinstein, M. *Macromolecules* 46, 7525–7541 **2013**.
- [10] Mordvinkin, A., Suckow, M., Böhme, F., *et al.* *Macromolecules* 52, 4169–4184 **2019**.
- [11] Liu, C., Qin, H. & Mather, P. T. *J. Mater. Chem.* 17, 1543–1558 **2007**.
- [12] Wang, S. & Urban, M. W. *Nat. Rev. Mater.* 5, 562–583 **2020**.
- [13] Zhang, M. Q. *Express Polym. Lett.* **2020**.
- [14] Varley, R. J. & van der Zwaag, S. *Acta Mater.* 56, 5737–5750 **2008**.
- [15] Cordier, P., Tournilhac, F., Soulié-Ziakovic, C. & Leibler, L. *Nature* 451, 977–980 **2008**.
- [16] Eisenberg, A. & Rinaudo, M. *Polym. Bull.* 24, 671 **1990**.
- [17] Yoshimizu, H. & Tsujita, Y. *Annu. Reports NMR Spectrosc.* 44, 1–22 **2001**.
- [18] Tadano, K., Hirasawa, E., Yamamoto, H. & Yano, S. *Macromolecules* 22, 226–233 **1989**.
- [19] Zhang, L., Brostowitz, N. R., Cavicchi, K. A. & Weiss, R. A. *Macromol. React. Eng.* 8, 81–99 **2014**.
- [20] Weiss, R. A. & Yu, W. C. *Macromolecules* 40, 3640–3643 **2007**.
- [21] Wignall, G. D., Alamo, R. G., Londono, J. D., *et al.* *Macromolecules* 33, 551–561 **2000**.
- [22] Longworth, R. & Vaughan, D. J. *Nature* 218, 85–87 **1968**.
- [23] Jia, Y., Kleinhammes, A. & Wu, Y. *Macromolecules* 38, 2781–2785 **2005**.
- [24] Massiot, D., Fayon, F., Capron, M., *et al.* *Magn. Reson. Chem.* 40, 70–76 **2002**.
- [25] Raiford, D. S. & Fisk, C. L. *Anal. Chem.* 51, 2050–2051 **1979**.
- [26] Baias, M., Demco, D. E., Colicchio, I., Blümich, B. & Möller, M. *Chem. Phys. Lett.* 456, 227–230 **2008**.
- [27] Kolodziejewski, W. & Klinowski, J. *Chem. Rev.* 102, 613–628 **2002**.
- [28] Fung, B. M., Khitritin, A. K. & Ermolaev, K. *J. Magn. Reson.* **2000**.

---

## 4. SELF-HEALING COMPOSITE MATERIALS WITH PLASMONIC NANOPARTICLES

### 4.1. Introduction

When functional nanoparticles and a polymer matrix are combined, they form an interesting class of hybrid materials. Nanoparticle (NP)-polymer hybrid materials, particularly when formed into thin films, are one type of hybrid material that can exhibit unique electrical, optical, mechanical, thermal, dielectric, and magnetic characteristics.<sup>1-4</sup> Furthermore, many polymer manufacturing methods may be utilized to create hybrid materials with little adjustments.<sup>5,6</sup> This benefit suggests that the polymer hybrids are produced at a low cost. Their possible uses vary from energy conversion to memory storage to foldable screens.<sup>7</sup>

Bending and form distortion of the films over time, as well as small cuts and damages might lead to early failures and decreased component life. Small nanoparticles must be distributed uniformly in the hybrid film to create a flexible composite. Appropriate flexibility assessment is also required in order to evaluate the properties of various hybrid films and effectively anticipate their behaviour in device applications.

When hybrid films are damaged by external distortion forces,<sup>8-10</sup> the ability to repair the damaged films is critical for maintaining performance and extending the lifetime of the associated devices.<sup>9,11,12</sup> Through reversible molecular interactions from the polymer matrix, an intrinsic self-healing ability can be introduced into the polymer matrix. However, the majority of self-healing processes take place at high temperatures.<sup>13</sup>

---

Plasmonic inorganic particles with a photothermal effect can be used to cure defects and damages. NPs from e.g. gold or silver, may cure polymers with certain wavelengths by converting electromagnetic energy to heat.<sup>13,14</sup> A localized surface plasmon resonance (LSPR) phenomenon occurs when an incoming electromagnetic beam is illuminated; confinement and collective oscillation of these polarizable electrons result in visible light absorption.<sup>15-17</sup>

Metal nanoparticles' surface plasmon resonance is beneficial for a variety of applications, including photothermal heating.<sup>18</sup> There has long been interest in dispersing NPs into polymers to form polymer composites, with particular emphasis on NP dispersion and how it affects or is impacted by the morphology of the polymer matrix.<sup>19-21</sup> Photothermal heating is an intriguing approach for achieving distant and localised heating with noble-metal NPs, and it has applications in therapy,<sup>22</sup> drug delivery,<sup>23-25</sup> polymer curing<sup>26</sup> and processing.<sup>27</sup> Photothermal triggering of self-healing is of great interest,<sup>28</sup> as well as a shape-memory-polymer effect linked to NP plasmonic properties.<sup>29-36</sup> The SPR wavelength and intensity are affected by the geometry of the NP as well as the chemical environment. Gold nanorods (AuNRs) have a faint transverse SPR at 530 nm that overlaps with the SPR of Au nanospheres, as well as a stronger, red-shifted longitudinal SPR. Light polarised along the length or orthogonal to the length of the AuNR, respectively, excites the longitudinal or transverse SPR. The wavelength of the longitudinal SPR exceeds 530 nm and is proportional to the aspect ratio of AuNRs.

Photothermal heating provides various advantages over traditional thermal heating, including the following: (i) the matrix can be heated in a noncontact way if it is sufficiently transparent for light to permeate and reach the NPs. (ii) changing of various characteristics of light may be used to accurately control heating.<sup>37,38</sup> (iii) because AuNPs transduce light into heat locally, their placement enables for extremely localised photothermal heating. The particle temperature

---

can reach 700 °C, which warms the surrounding polymer matrix.<sup>39-43</sup> With reaching the glass transition temperature, material flows, healing the damage.

The production and photothermal healing of hybrid films made of ionomer Surlyn PC2000 or self-healing blend Surlyn PC2000/EPDM/DCP with incorporated plasmonic nanoparticles (AuNR and LaB<sub>6</sub>) is the focus of this research. By coprecipitation and hot pressing, photothermally active composite materials with a tunable optical imprint were created. Optimal concentrations of AuNRs and LaB<sub>6</sub> plasmonic nanoparticles have been established and healing ability of the composited under the action of IR radiation has been confirmed.

---

## 4.2. Results and discussion

### 4.2.1 Synthesis of functional plasmonic nanoparticles and their stabilization

Composites based on commercially available polymers and plasmonic nanoparticles (gold nanorods, gold nanoparticles and LaB<sub>6</sub>) were obtained to select initiation modes, determine effective concentrations, and study the self-healing process, which provide uniform material heating under infrared radiation (IR) due to plasmon resonance.

As part of this project, gold nanorods (NRs) were synthesized by reduction on soft matrices represented by a micellar surfactant solution. We obtained NRs with sizes of 16 × 70 nm, whereby the longitudinal plasmon resonance can be tuned in a fairly wide range (610 - 920 nm). The gold nanorods exhibit two typical absorption peaks at 511 nm (transverse surface plasmon peak, i.e., TSPP) and around 800 nm (longitudinal surface plasmon, i.e., longitudinal surface plasmon peak (Figure 1)). To increase the affinity of the AuNR to the utilized matrix polymers, as well as to increase their stability in suspension, the nanorods were modified with functional polyethylene glycol (PEG) with the molecular weights ranging from 0.8 to 3 kDa (Figure 1).

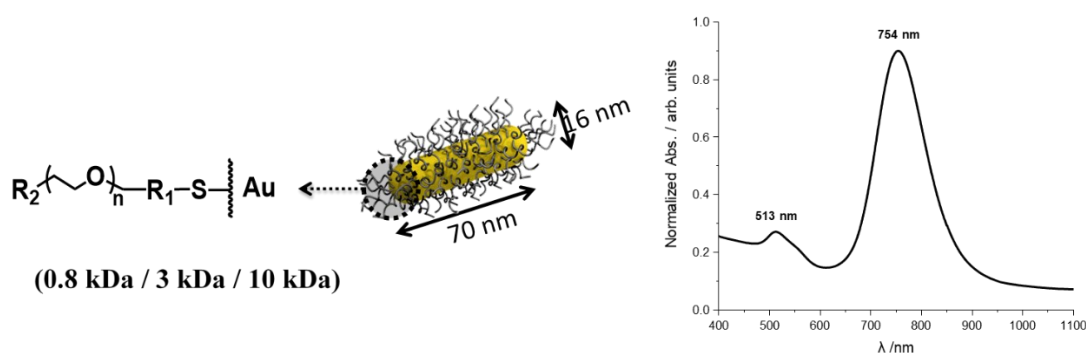


**Figure 1.** Structure and optical absorption spectra of synthesized polyether-functional AuNR

Stabilized milling produced (MP) LaB<sub>6</sub> nanoparticles (Ø 20 nm) or plasma produced (PP) nanoparticles (Ø 20 nm) were also used as plasmonic nanoparticles in compositions with the matrix polymers. LaB<sub>6</sub> (PP) was additionally stabilized by PhB(OH)<sub>2</sub>. The optical absorption spectrum of PhB(OH)<sub>2</sub> stabilized PP LaB<sub>6</sub> and commercially available stabilized MP LaB<sub>6</sub> with absorption peak maximums at 820 and 975 nm, respectively, are presented in Figure 2.

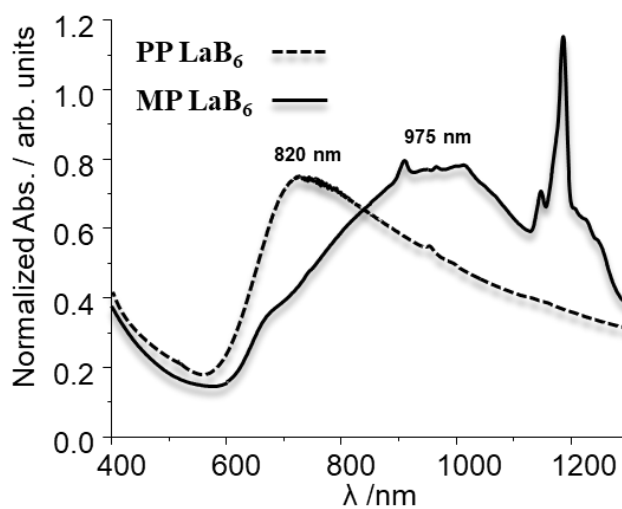


**Figure 2.** Optical absorption spectrum of PhB(OH)<sub>2</sub> stabilized PP LaB<sub>6</sub> and commercially available stabilized MP LaB<sub>6</sub> (dispersion in water).

#### 4.2.2 Study of methods of introducing plasmonic nanoparticles into polymer matrices. Determination of effective concentrations and modes of external exposure

In this study, composites of polysulfone (PSU), Surlyn PC2000 ionomer, and self-healing matrix consisting of Surlyn PC2000/EPDM/DCP containing functional plasmonic NPs as photothermally active composites with tuneable optical imprint were prepared. The robust matrix polymer PSU is a hydrophobic thermoplastic material made from bisphenol-A and the corresponding bis(p-halogenphenyl)sulfone by a multistep polycondensation reaction. PSU is commercially available in form of pellets and yields a strong material with high

---

transparency in the range from  $\lambda = 400$  nm to  $> 1600$  nm after thermal moulding or casting from a solution. The use of this polymer made it possible to determine the effective concentrations of plasmonic NPs to achieve efficient heating under IR radiation, as well as the selection of plasmon resonance initiation modes. The composites were prepared by mixing a solution of PSU and a suspension of nanoparticles in dichloromethane (DCM) (in the case of MP LaB<sub>6</sub> in isopropanol). Shaping was carried out at the polymer melting point by hot pressing (after coprecipitation and drying of the resulting powder under reduced pressure) or by solvent evaporation (Figure 3).

The ionomer known under the brand name Surlyn has recently become a subject of interest due to its ability to self-heal at elevated temperatures. Previously obtained self-healing composites derived from a mixture of Surlyn PC2000 and EPDM polymers followed by DCP crosslinking were also filled with plasmonic nanoparticles to initiate IR-induced self-healing. The composites were also prepared using a similar technique for PSU-NP by mixing a Surlyn PC2000 or Surlyn PC2000/EPDM/DCP solution in toluene/butanol-1 mixture at 65 °C and a nanoparticle suspension in DCM (in the case of MP LaB<sub>6</sub> in isopropanol) followed by coprecipitation and drying of the resulting powder at reduced pressure. Shaping was carried out at the melting temperature of the polymer by hot pressing (Figure 3).

The list of the obtained polymer matrix-NP composite materials, their properties, as well as the properties of the used nanoparticles are presented in Table 1.

**Table 1:** properties of used nanoparticles and obtained matrix-NP composites

N	NP type	$d_{NP}$ [nm]	Dispersing agent	$\omega$ end-groups*	$M_n^a$ [kDa]	Stability (dispersion) <sup>b</sup>	Film colour <sup>c</sup>	
							Solvent casting	Hot pressing
PSU/NP composite								
1	AuNP	20	$\alpha$ -thiol PEG	OMe	0.8	yes	pink	-
2	AuNR	$L = 70$ $d = 16$	$\alpha$ -thiol PEG	OMe	0.8	yes	red	pink
3			$\alpha$ -thiol PEG	OH	3	yes	blue	red
4	LaB <sub>6</sub> (PP) <sup>d</sup>	20	PhB(OH) <sub>2</sub>	-	0.12	yes	green	green
5	LaB <sub>6</sub> (MP) <sup>d</sup>	20	[commercial]	-	-	yes	-	green
Surlyn PC 2000/NP composite								
6	AuNR	$L = 70$ $d = 16$	$\alpha$ -thiol PEG	OH	3	yes	-	red
7	LaB <sub>6</sub> (MP)	20	[commercial]	-	-	yes	-	green
Surlyn PC 2000/EPDM/DCP/NP composite								
8	AuNR	$L = 70$ $d = 16$	$\alpha$ -thiol PEG	OH	3	yes	-	red
9	LaB <sub>6</sub> (MP)	20	[commercial]	-	-	yes	-	green

<sup>a</sup> Commercial products, values given by the supplier.

<sup>b</sup> Dispersion stability was determined visually by colour changes and detection of precipitates.

<sup>c</sup> Freestanding PSU-NP film after solvent evaporation.

<sup>d</sup> PP – plasma produced, MP – milling produced

\*OMe = methoxy and OH = hydroxy end-groups

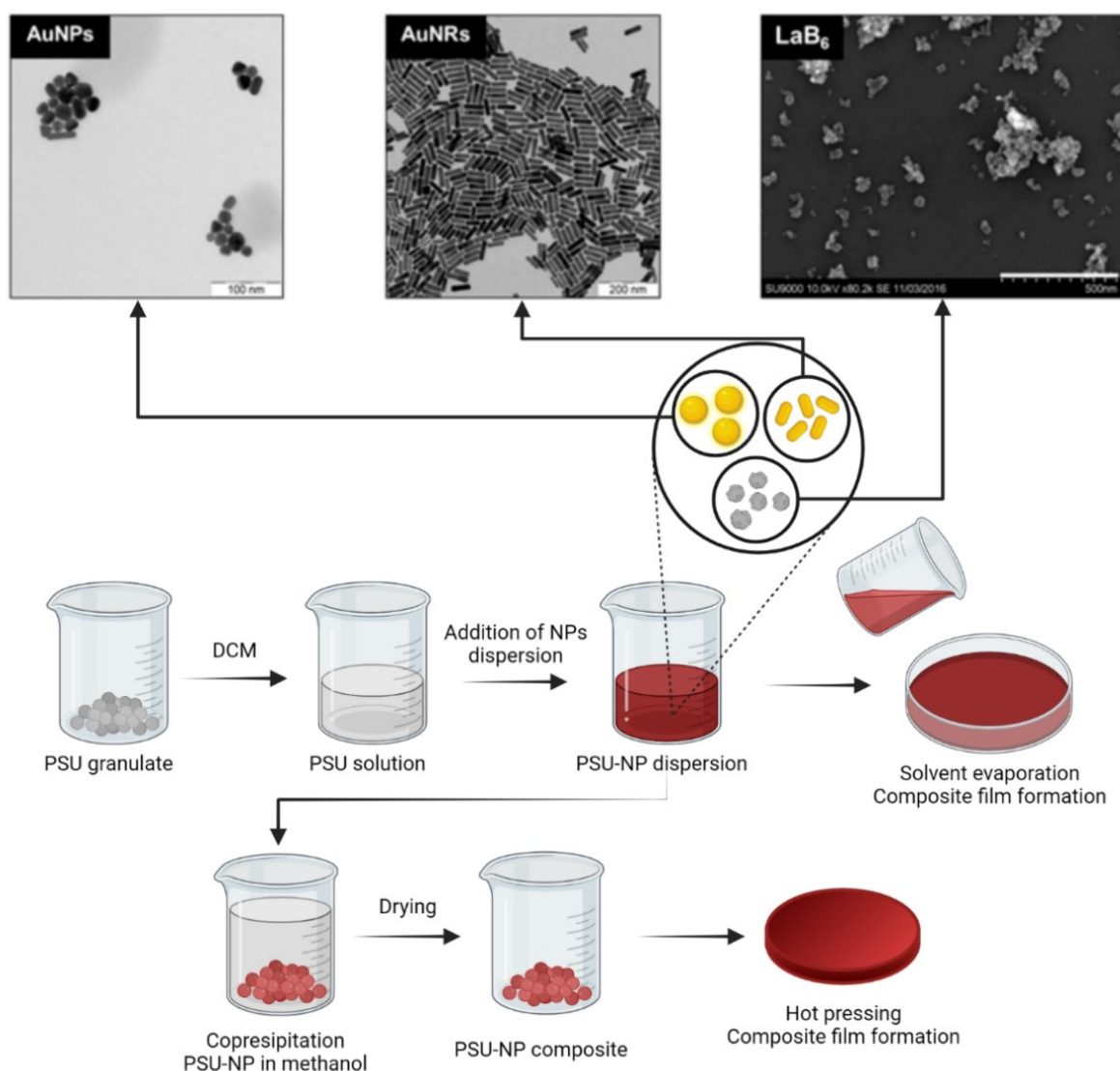


**Figure 3.** Fabrication of PSU-NP, Surlyn PC2000-NP or Surlyn PC2000/EPDM/DCP-NP composite films.

After complete evaporation of DCM in the hot pressing process, the resulting PSU-NP composite films, which are active in the near-infrared region of the spectrum, were further investigated for their optical properties using UV-visible spectroscopy. Furthermore, the determination of the presence of NPs within the polymer matrices was studied using TEM. The absorption maxima of AuNR and LaB<sub>6</sub> were tuned to match the NIR laser output maximum ( $\lambda = 800 \text{ nm}$ ) to study their thermal response during IR irradiation.

---

Figure 4 shows the optical absorption spectra and TEM photos of the corresponding PSU-NP composite films. As a reference example, PSU - AuNPs@PEG-0.8K exhibit a single absorption maximum at  $\lambda = 534$  nm (Figure 4b) due to the uniaxial plasmon resonance of the spherical AuNPs used.<sup>43</sup> While two absorption maxima at  $\lambda = 512$  nm and 920 nm were observed for the PSU-AuNRs@PEG-0.8K composites obtained by solvent evaporation (3.2.2.2a), and  $\lambda = 512$  nm and 825 nm for the PSU-AuNRs@PEG-3K made by hot-pressing (Figure 4c) caused by the transverse (TSPR) and longitudinal surface plasmon resonance (LSPR) of asymmetric AuNRs, respectively.<sup>44</sup> TEM micrographs of PSU-AuNRs@PEG-0.8K thin sections confirmed that the AuNRs are homogeneously distributed within the PSU matrix.

For PP PSU-LaB<sub>6</sub>, broader NIR absorption was detected with a maximum at  $\lambda = 805$  nm (for evaporated samples, Figure 4d-i) and  $\lambda = 822$  nm (for hot-pressed samples, Figure 4d-iii). Notably, the size of LaB<sub>6</sub> NP agglomerates in case of the hot-pressed samples was significantly smaller (250 nm for samples prepared by solvent evaporation and 100 nm for hot-pressed samples), indicating a better distribution of LaB<sub>6</sub> during the melting processes (Figure 4d-ii/v). The use of LaB<sub>6</sub> obtained by the milling method broadened the absorption band with a maximum at  $\lambda = 1030$  nm, allowing the sample to be irradiated in the higher infrared light spectrum (Figure 4d-iv). However, the size of particle agglomerates is relatively similar with PP LaB<sub>6</sub> with sizes of approximately 100 nm (Figure 4d-vi).

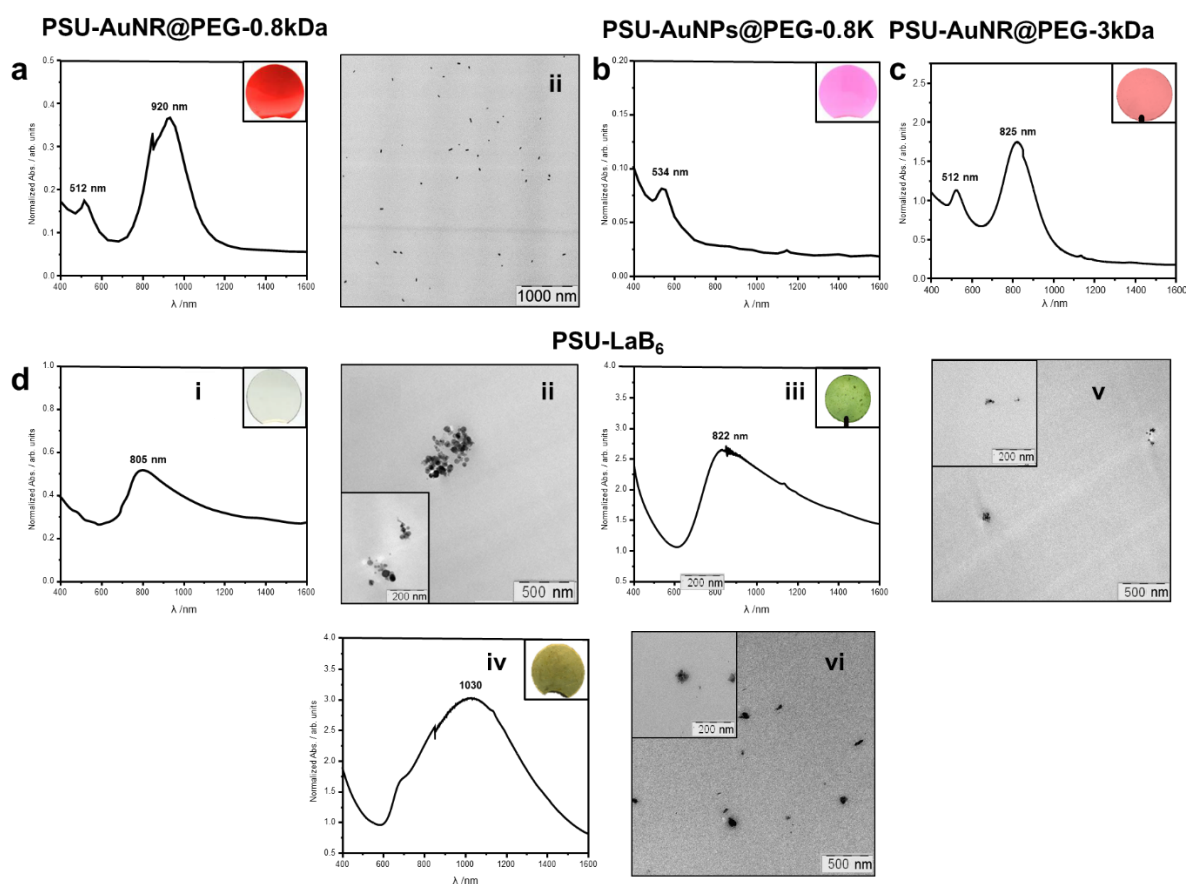


**Figure 4.** (a) (i) optical absorption spectra of PSU-AuNRs@PEG-0.8K prepared by solvent evaporation and (ii) respective TEM micrograph of a thin film. (b) PSU-AuNPs-PEG-0.8kDa. (c) Optical absorption spectra of PSU-AuNRs@PEG-3K prepared by hot pressing. (d) (i) PSU-LaB<sub>6</sub>(PP) prepared by solvent evaporation and (ii) its TEM micrograph. (iii) PSU-LaB<sub>6</sub>(PP) prepared by hot pressing and (v) its TEM micrograph. (iv) PSU-LaB<sub>6</sub>(MP) composite prepared by hot pressing and (vi) its TEM micrograph.

The transition of NR into NP and the formation of NP agglomerations depending on the method of composite production and/or the choice of stabilizing agent were the subject of subsequent investigations. It was established previously,<sup>45</sup> that films containing AuNRs obtained by solvent evaporation have a strong tendency to agglomerate when modified with higher molecular weight PEG derivatives. After evaporation of the solvent, the films obtained from non-stable dispersions were stained blue due to AuNRs agglomeration. TEM microphotographs showed that the AuNRs aggregated into sphere-like aggregates (~ 500 nm in size) upon solvent evaporation, resulting in a strong spectral shift to the blue side with respect to the spectrum of the initial red coloured dispersion.

---

Thus, we can state that an increasing molecular weight of the PEG ligand, decreases the stability of the PSU dispersion/matrix. Furthermore, the different end groups of the PEG ligands cause additional attraction forces, i.e., hydrogen bond interactions, leading to AuNR aggregation, especially overnight in the presence of DCM.

The influence of the duration of the heat treatment during the hot pressing on the nanorod-nanoparticle transition temperature was established before by Sjören Schweizerhof<sup>45</sup>. For PSU-AuNRs-PEG-0.8kDa, the transition temperature from rod-shaped to spherical particles occurs quite quick at about 300 °C. The noticeable colour change from red to pink indicates this change of shape. Despite the change of the form, the AuNRs remain uniformly distributed in the polymer matrix without visible agglomeration, proving their excellent compatibility with PSU.

This fact prompted us to use a lower temperature when preparing samples for hot pressing. However, since the PSU moulding temperature is usually 350 °C, the time of heat exposure was lengthened. It was found that the absorption maximum,  $\lambda = 825$  nm, characteristic of AuNRs-PEG-3kDa dispersion in water, shifts towards shorter wavelengths with increasing temperature treatment time during hot pressing of the composite, reaching 650 nm after 1 h at 240 °C (Figure 5b). The repetition of the hot pressing experiments showed that the optimal fabrication time for homogeneous PSU-NRs composites is 15 min at 240 °C (Figure 5c-iii). Thus, by heat treating the composite film, the AuNR aspect ratio can be changed and the absorption maxima can potentially be adjusted from 800 nm (AuNR) to about 500 nm (AuNP) (Figure 5a).<sup>46</sup> Moreover, the colour change of the material after hot pressing to pink supports the assumption of the presence of spherical-shaped NP (Figure 5-c,iv). Indeed, TEM microphotographs proved that not only nanorods but also nanoparticles were present after the melt treatment (Figure 5c-ii). The generated spheres had an average diameter of  $d = 33$  nm  $\pm$  6 nm and

occupied approximately the same volume as the originally used AuNRs ( $L_{\text{AuNR}} = 70 \text{ nm}$ ,  $d_{\text{AuNR}} = 16 \text{ nm}$ ). Thus, AuNRs are not stable at high temperatures ( $>250 \text{ }^\circ\text{C}$ )<sup>42</sup> and quickly transform into spherical particles, which agrees well with literature data.<sup>42,46,47</sup>

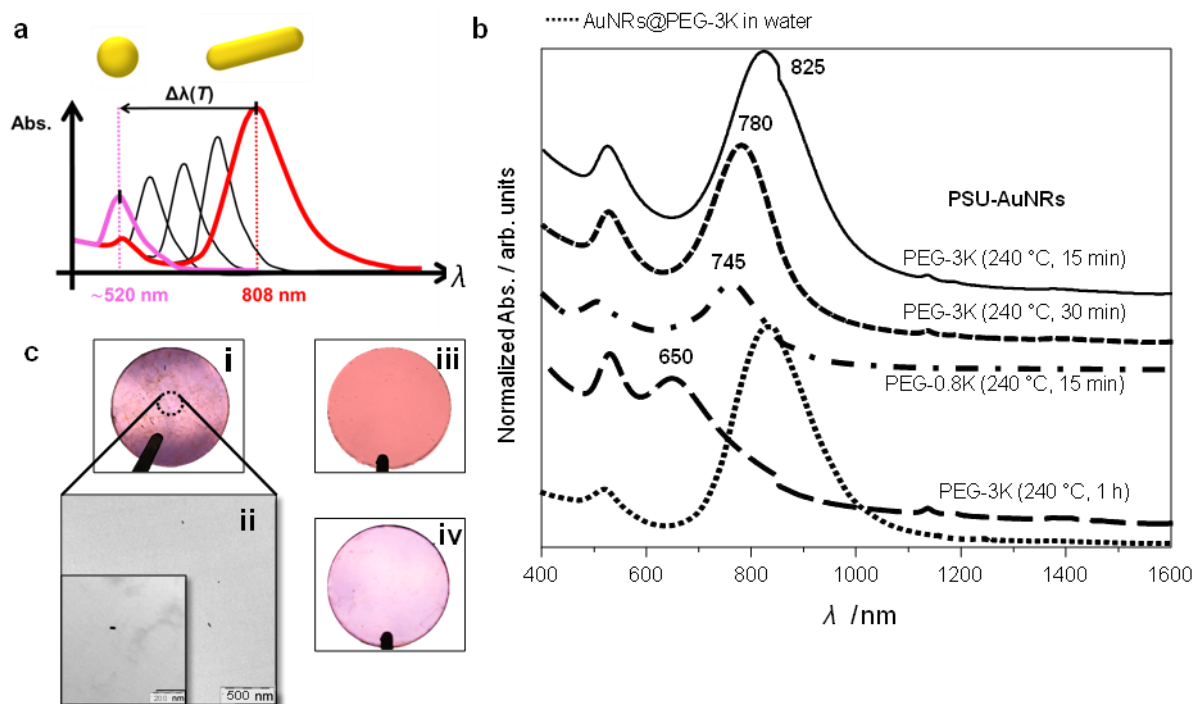


**Figure 5.** (a) tunable optical spectrum of AuNR due to (photo) thermally induced shape changes of nanorods ( $\Delta\lambda(T)$ ) in the range from 800 to 500 nm. (b) Optical absorption spectra of PSU-AuNRs@PEG-3K composites obtained by hot pressing with different heat treatment times (240  $^\circ\text{C}$  from 15 to 60 min) and PSU-AuNRs@PEG-0.8K, versus AuNRs@PEG-3K dispersion in water (c) (i) PSU-AuNRs@PEG-0.8K composite film (hot pressing 240  $^\circ\text{C}$ , 15 min) and (ii) corresponding micrograph of thin film obtained by PEM. (iii) PSU-AuNR@PEG-3K composite film (hot pressing 240  $^\circ\text{C}$ , 15 min) and (iv) PSU-AuNR@PEG-3K composite film (hot pressing 240  $^\circ\text{C}$ , 1 h).

The most useful characteristic of NIR-active composite materials is their photothermal properties. Irradiation at the absorption maximum with a NIR laser ( $\lambda = 808 \text{ nm}$ ) causes rapid conversion of incident light to heat. The heat release during irradiation was monitored with a high-speed thermal imaging camera and the corresponding temperature profiles were recorded (Figure 6a).

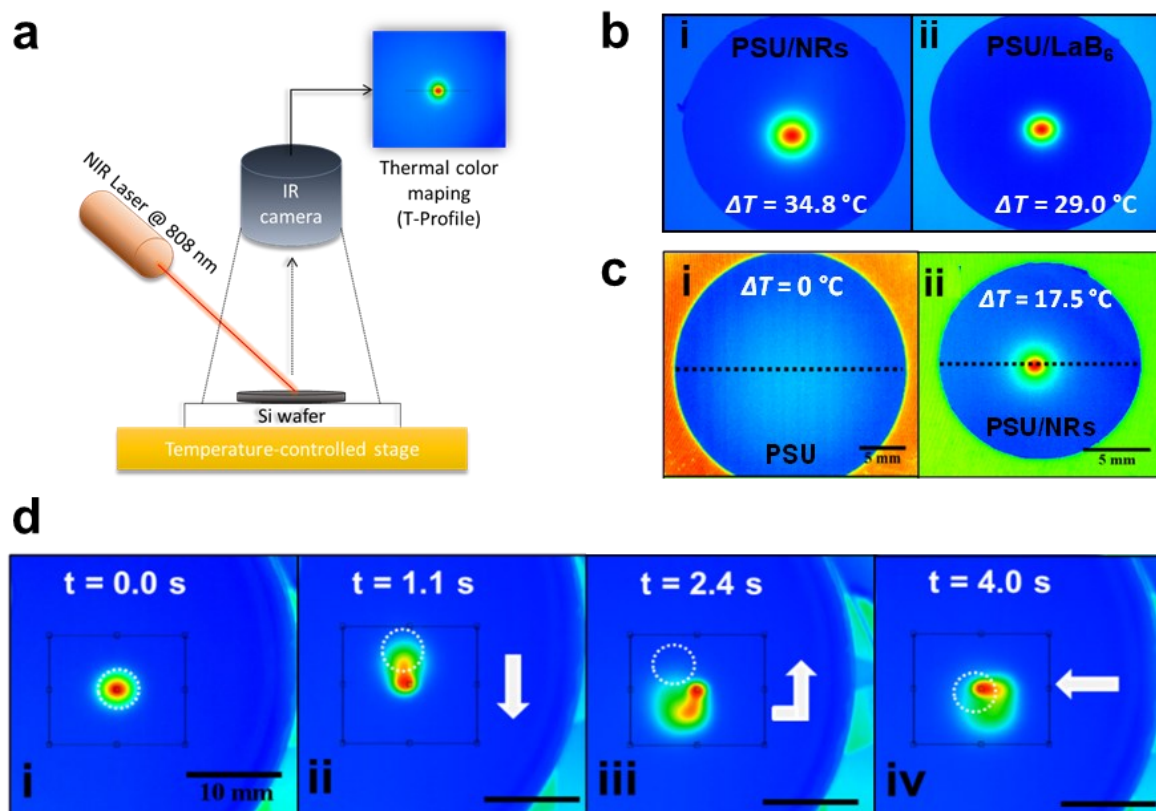


**Figure 6.** (a) laser setup for photothermal heating of PSU-NP composites. (b) Thermal colour map and respective temperature ( $\Delta T$ ) of PSU-NPs composites obtained by hot pressing (i) PSU-AuNR@PEG-3K and (ii) PSU-LaB<sub>6</sub> (PP). (c) Thermal colour map and respective temperature ( $\Delta T$ ) of (i) pure PSU and (ii) PSU-AuNR@PEG-0.8K along the dashed line at pulsed laser irradiation. (d) Thermal color map of PSU-LaB<sub>6</sub> (PP) at varying time scale and laser position.

As expected, pure PSU showed no significant temperature change during irradiation at 808 nm at  $P = 86$  mW (pulsed mode, 1 ms on, 15 ms off) (Figure 6c-i) due to its transparency at 808 nm. In comparison, the PSU-AuNRs@PEG-0.8K prepared from solution showed an average temperature of 20 °C without irradiation, which was set by the temperature-controlled pad. When the same sample was irradiated (Figure 6c-ii) with the same parameters as for pure PSU, a rapid temperature rise to about 37.5 °C ( $\Delta T = 17.5$  °C) was observed. After the laser was turned off, the sample temperature quickly decreased to the initial 20 °C. In addition, a dynamic experiment using PSU-LaB<sub>6</sub> (PP) and screening different positions of the sample showed that heat is generated only in locations where the laser beam hits/penetrates the material surface (Figure 6d). On a relatively short time scale, the maximum temperature emission ( $T_{\text{max.}} \sim 40$  °C)

---

follows the laser beam. The initial position of the laser is marked by the dotted circle in Figure 6d.

The photothermal heating could be enhanced when the PSU-NP composites were fabricated by hot pressing. In this case, the possibly favourable distribution of the NPs within the material lead to the observation of a higher maximum temperature. The maximum effect was achieved for the PSU-AuNR@PEG-3kDa composite ( $T_{\text{max.}} = 54.8 \text{ }^{\circ}\text{C}$ , Figure 6b-i), but also with PSU-LaB<sub>6</sub> (PP), a very strong increase was observed ( $T_{\text{max.}} = 49.0 \text{ }^{\circ}\text{C}$ , Figure 6b-ii).

Commercial thermal imaging cell phone adapters provide an inexpensive alternative for quickly assessing the temperature profile of composites during near-infrared irradiation. The fabricated samples were irradiated with NIR light ( $\lambda = 850 \text{ nm}$ ,  $P = 1.6 \text{ W}$ ) and the thermal colour map was observed using a commercially available smartphone adapter (Figure 7a). For this particular study, five different samples were made with PSU-based NP composites produced by hot pressing (Figure 7c-f). The sample in Figure 8c contains pure PSU as the reference material, Figure 7d-f shows samples from PSU-AuNRs@PEG-0.8K (red), PSU-AuNRs@PEG-3K (red) and PSU-LaB<sub>6</sub> (PP) (green), respectively. The heat maps to the right of the corresponding images in Figure 7c-f show the unirradiated (i) and the irradiated state (ii).

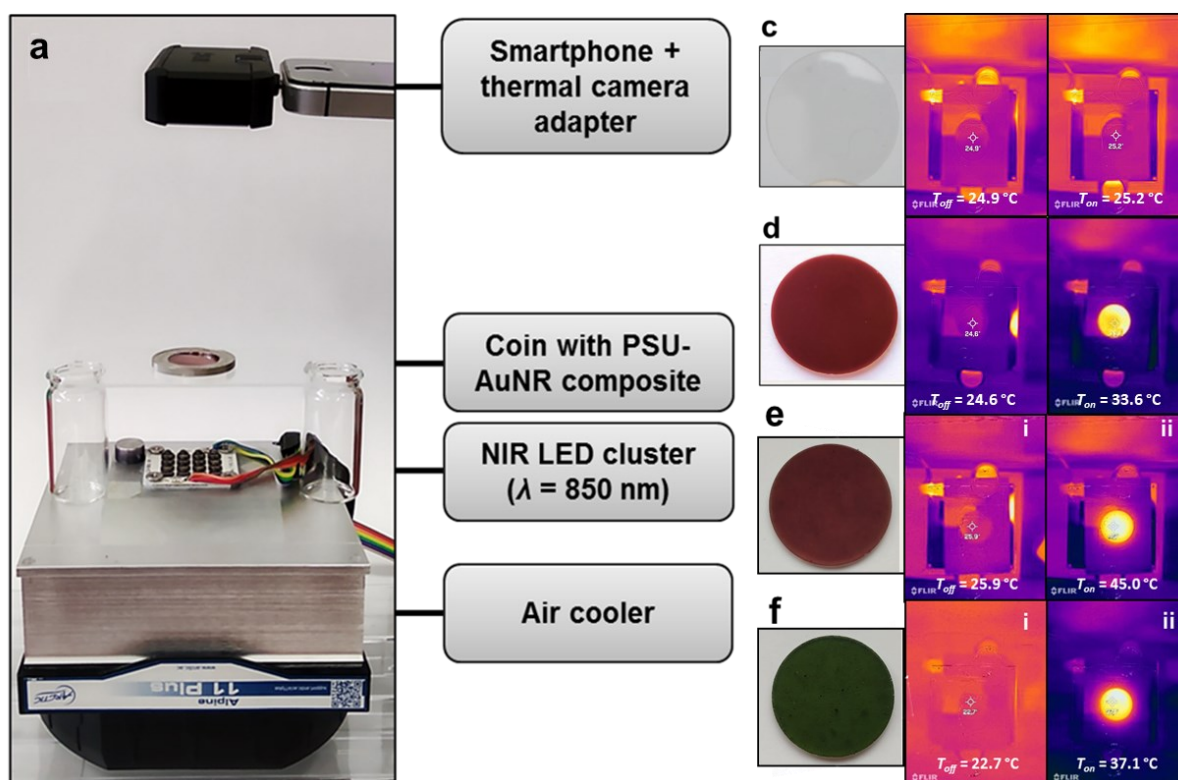


**Figure 7.** (a) Installation to check the security of fabricated coins using a smartphone with an adapter for an external thermal imaging camera and a homemade cluster of NIR LEDs for photothermal heating. Samples produced with (c) pure PSU, (d) PSU-AuNRs@PEG-0.8K, (e) PSU-AuNRs@PEG-3K (hot pressing) and (f) PSU-LaB<sub>6</sub> (PP). The colour heat maps on the right show samples of (i) the unirradiated and (ii) irradiated states.

As expected, the pure PSU showed no significant temperature change when irradiated ( $\Delta T = 0.3$  °C, Figure 7c-i/ii). When the disk contained evenly distributed AuNRs however, the temperature difference was  $\Delta T = 9.0$  °C (Figure 7d-i/ii). Irradiation of the sample obtained by hot pressing containing AuNR gave  $\Delta T = 19.1$  °C (Figure 7e-i/ii). For the PSU-LaB<sub>6</sub> (PP) composite,  $\Delta T$  was lower (14.4 °C), probably due to the formation of LaB<sub>6</sub> NP agglomerates.

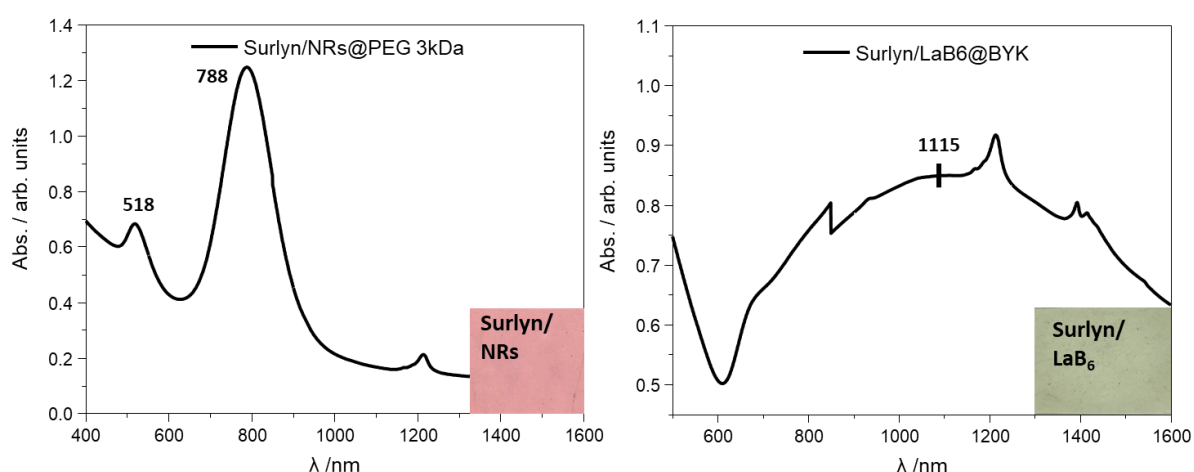
Thus, simple and cost-effective systems for rapidly determining photothermal temperature changes are available. This makes our system potentially attractive not only as an application for self-healing materials, but also for convenient use as a protective marker for everyday objects.

In conclusion, co-precipitation followed by hot pressing or solution casting of polysulfone (PSU) composites, Surlyn PC 2000 ionomer, or Surlyn PC 2000/EPDM/DCP matrices containing functional plasmonic NPs as photothermally active composites with tunable optical imprints can be prepared.

#### 4.2.3 Investigation of the healing process of polymer composites with plasmonic nanoparticles

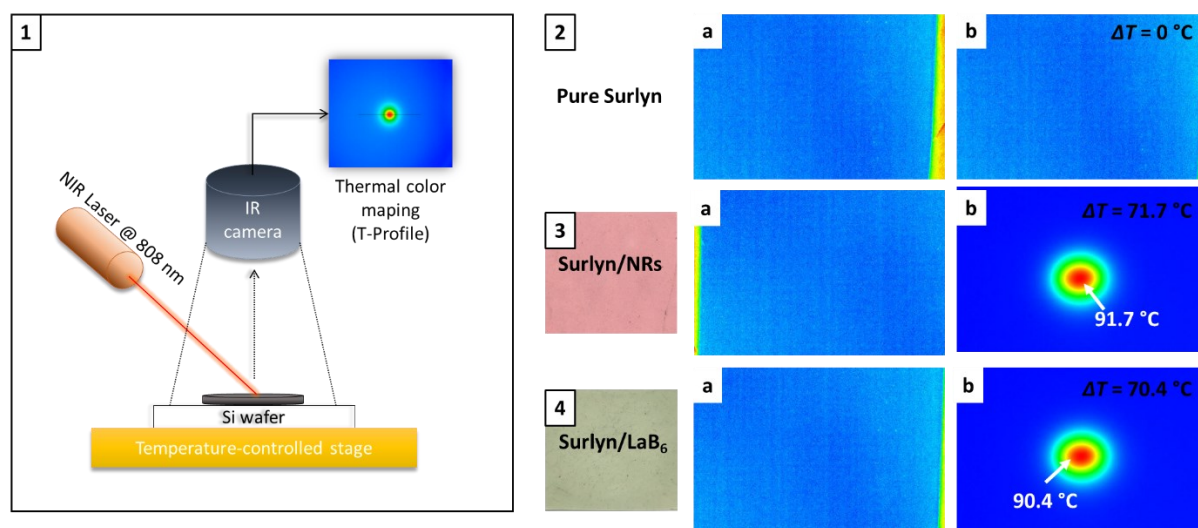
In the next step, we carried out a comparison of the efficiency of healing processes when using different types of energy input to self-healing compositions namely laser or LED block.

Figure 8 shows the optical absorption spectra of Surlyn PC2000/NRs and Surlyn PC2000/LaB<sub>6</sub> composite films. For the Surlyn PC2000/NRs composites, two absorption maxima were observed at  $\lambda = 518$  nm and 788 nm, while for Surlyn PC2000/LaB<sub>6</sub>, only one broad peak with a maximum of  $\lambda = 1115$  nm is visible. This shows that the established procedure for sample preparation does not change the properties of plasmonic nanoparticles, compared to the optical absorption spectra of NP dispersions in water (Figure 1 and 2).



**Figure 8.** Optical absorption spectra of Surlyn PC2000/NRs and Surlyn PC2000/LaB<sub>6</sub> composite films obtained by hot pressing.

In the next stage of the study, the obtained composites were irradiated at the absorption maximum with a NIR laser ( $\lambda = 808$  nm), leading to a rapid conversion of the incident light to heat. The heat release during irradiation was monitored with a high-speed thermal imaging camera and the corresponding temperature profiles were recorded (Figure 9). As expected, the pure Surlyn polymer matrix showed no significant temperature changes during irradiation at 808 nm at  $P = 86$  mW (pulsed mode, 1 ms on, 15 ms off) due to its transparency at 808 nm. Composite materials with plasmonic nanoparticles first showed an average temperature of 20 °C without irradiation, which is set at the initial stage by the thermostat. When the same samples were irradiated using identical parameters as for the pure matrix polymer, a rapid temperature increase was observed (average  $\Delta T = \sim 72$  °C). In the case of the Surlyn/LaB<sub>6</sub> composite, the heating effect is maximal, increasing the temperature of the sample to approximately 90.4 °C ( $\Delta T = 70.4$  °C) in 20 s of exposure. After turning off the laser, the sample temperature quickly cools down to the original 20 °C (Figure 9).



**Figure 9.** (1) laser setup for photothermal heating of PSU-NP composites. Thermal colour map and corresponding temperature ( $\Delta T$ ) of pure Surlyn PC2000 (2) and its composites with plasmonic nanoparticles: Surlyn PC2000/NRs (3) and Surlyn PC2000/LaB<sub>6</sub> (4) before (a) and after (b) exposure.

The fabricated samples were additionally irradiated with NIR light ( $\lambda = 850$  nm,  $P = 1.6$  W) using a  $2 \times 2$  cm LED block, and the thermal colour map was observed using a commercially available smartphone adapter (Figure 10). The sample in Figure 10 (2) contains pure Surlyn PC2000 as the reference material; Figures 11(3)-(4) show samples of Surlyn PC2000/NRs and Surlyn PC2000/LaB<sub>6</sub>. The heat maps on the right of the photographs of the samples show the unirradiated (a) and the irradiated state (b).

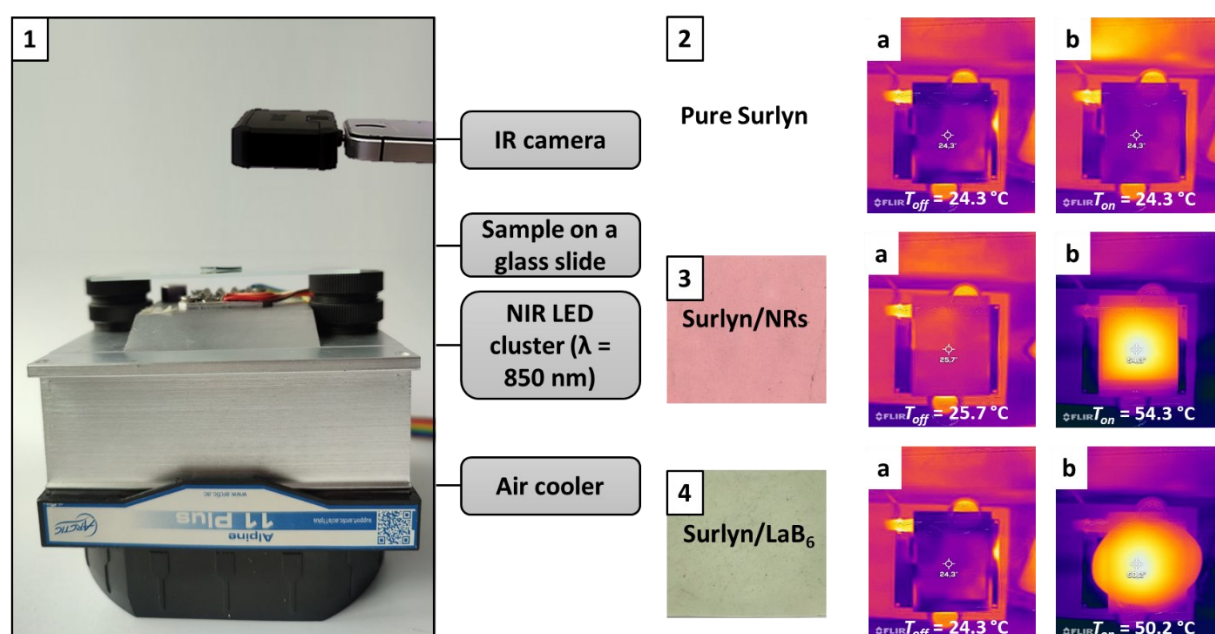


**Figure 10.** Study of the temperature response of composites with plasmonic nanoparticles under the action of IR radiation using a smartphone with an external thermal camera adapter and a custom-made cluster of NIR LEDs for photothermal heating (1). (2) Pure Surlyn PC2000 in (a) unirradiated and (b) irradiated state; (3) Surlyn PC2000/NRs in (a) unirradiated and (b) irradiated state; (4) Surlyn PC2000/LaB<sub>6</sub> in (a) unirradiated and (b) irradiated state.

As expected, the pure Surlyn polymer matrix showed no significant temperature change during irradiation ( $\Delta T = 0$  °C, Figure 10(2) a-b). When Surlyn contains evenly distributed AuNRs, however, the temperature difference was measured at  $\Delta T = 28.6$  °C (Figure 10(3) a-b). Irradiation of the samples containing LaB<sub>6</sub> gave  $\Delta T = 25.9$  °C (Figure 10(4)a-b). The difference in thermal response to IR irradiation for LaB<sub>6</sub> and AuNR composites in Surlyn PC2000 matrix was minimal.

---

In addition, the healing of small scratches on the surface of Surlyn PC2000/NRs and Surlyn PC2000/LaB<sub>6</sub> composites by irradiation with a near-infrared laser ( $\lambda = 808$  nm) was studied. Due to the fast local heating of the lesion, rapid visible healing of the scratches was observed. However, the small contact spot of the laser beam with the material does not allow larger lesions to heal, so it was decided to use a homemade 2-by-2-cm LED block ( $\lambda = 850$  nm,  $P = 1.6$  W) as an infrared radiation source, and the heat map was recorded using a high-speed thermal imaging camera.

Fine scratches approximately 0.2 mm deep and 3 to 5 mm long were applied to the surface of the composites with a scalpel. Subsequently, healing of the scratches was performed in the infrared radiation mode ( $\lambda = 850$  nm,  $P = 1.6$  W) at a distance of 1 cm from the radiation source. Rapid closure of the incisions was observed within 35 seconds of the start of the radiation. Figure 11 shows photographs of the Surlyn PC2000/LaB<sub>6</sub> sample before the onset of radiation (a). Within 10 seconds of the applied IR radiation, the closure of the incision was observed (Figure 11b), and after 35 seconds its complete disappearance was evident (Figure 11d). The temperature of the sample was recorded with a thermal imaging camera. After 10 sec of radiation the sample reached a maximum temperature of 55.7 °C and the closure of the cut was observed, while after 6 sec (max. sample temperature 60.1 °C) the beginning of the damage healing occurred. The specimen was kept irradiated for an additional 20 sec and reached a temperature of 84 °C. Complete closure of the incisions was also recorded by scanning electron microscopy for both Surlyn PC2000/LaB<sub>6</sub> and Surlyn PC2000/NRs composites (Figure 12).

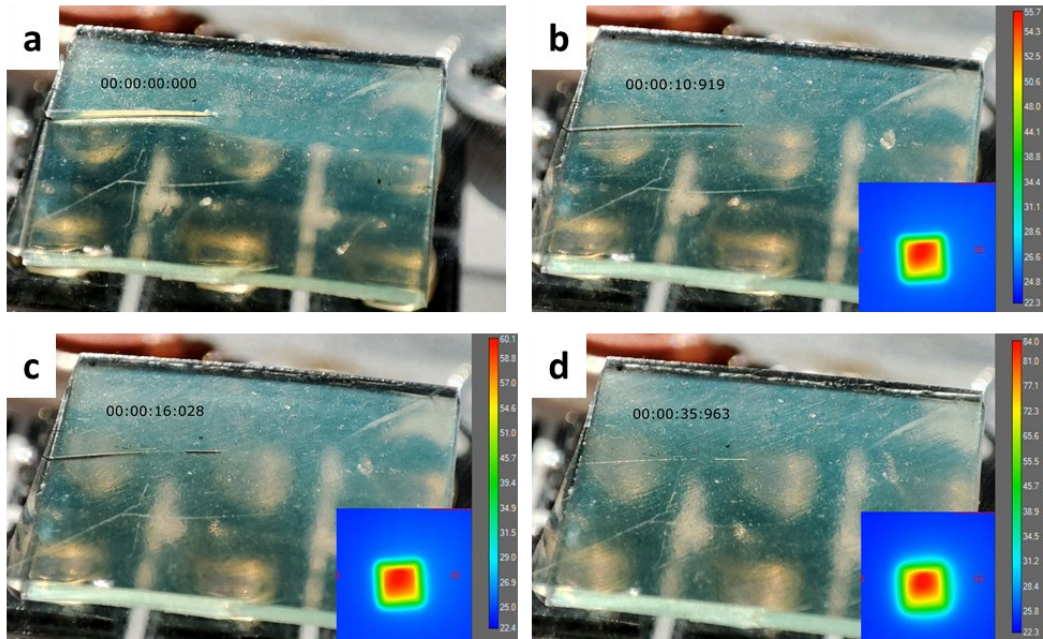


**Figure 11.** Curing of shallow scratches 0.23 mm deep on the surface of Surlyn PC2000/LaB<sub>6</sub> composite. Before IR irradiation (a), after 10 (b), 16 (c) and 35 sec (d).

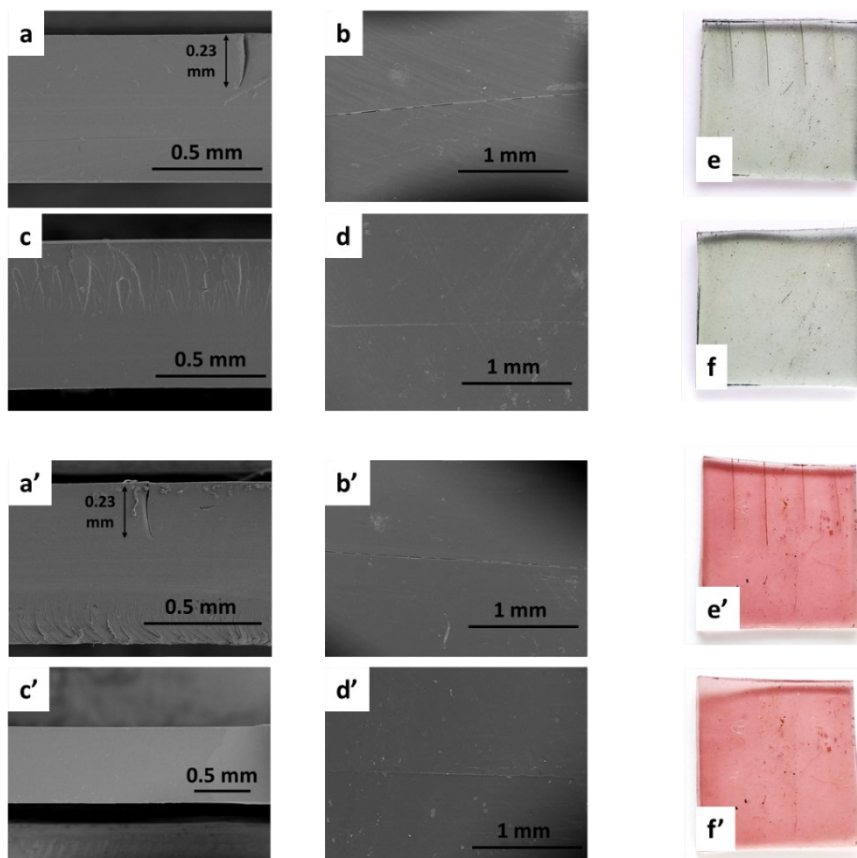


**Figure 12.** Study of healing process of Surlyn PC2000/LaB<sub>6</sub> (a-f) and Surlyn PC2000/NRs (a'-f') composites under the influence of IR radiation. Photographs of 10×10 mm samples before (a, a') and after (f, f') healing. Scanning electron microscopy of composites before (side view: a, a', top view: b, b') and after (side view: c, c', top view: d, d') damage healing.

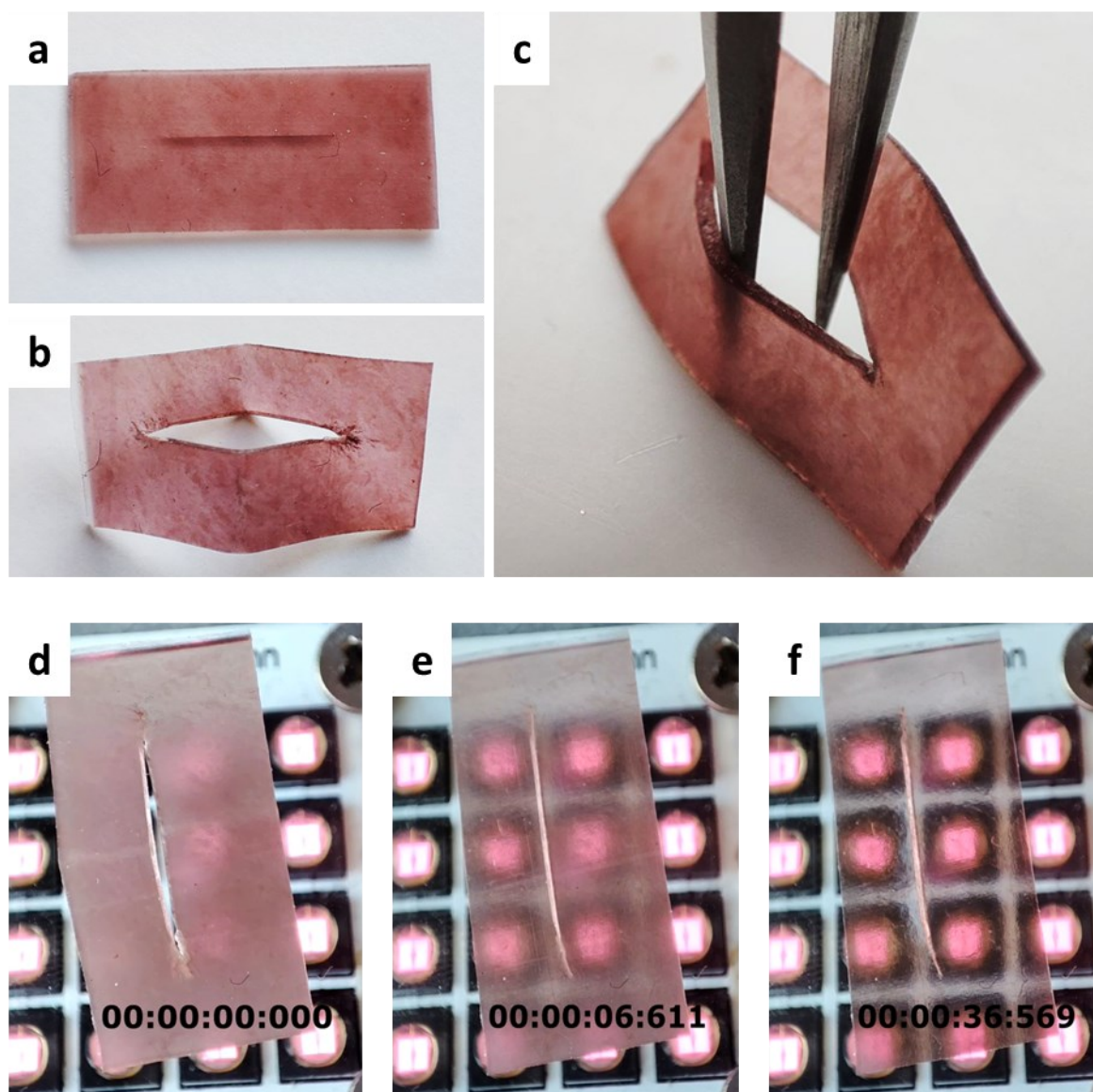


**Figure 13.** Healing of a large lesion caused by incision followed by cold deformation. The specimen was prepared with Surlyn PC2000/EPDM (70/30) and gold nanorods cross-linked with 0.5 wt %. DCP. The sample was prepared by coprecipitation and moulded by hot pressing (1 h - 110 °C, p = 10 bar). Where a-c depict the original sample after damage application, before the IR radiation (d) and after 6 (e) and 36 s (f) of IR radiation.

Next, we demonstrate self-healing experiments that use a combination of macroscopic structure regeneration due to the shape memory effect combined with microscopic healing, which is provided by restoring the ion cluster structure under the action of IR radiation (Figure 13). For this experiment, a sample of Surlyn PC 2000/EPDM polymer crosslinked with DCP was mixed with gold nanorods was prepared, which had previously shown to heal large lesions at elevated temperatures. The findings show how a defect ranging from millimetres

---

to centimetres can be repaired by stress induced defect formation. The healing process is initiated by IR radiation, and the two surfaces formed by the incision were healed and could not be separated. However, complete disappearance of the healed damage scar was not observed even after 40 sec of exposure to IR radiation. This effect may be caused by reduction of the mobility of the ionic groups effected by polyethylene crystals.

---

### 4.3. Conclusions

Composites of polysulfone (PSU) and Surlyn PC2000 ionomer, as well as Surlyn PC2000/EPDM cross-linked DCP, containing functional plasmonic NPs as photothermally active composite materials with a tunable optical imprint, were prepared by the method of co-precipitation followed by hot pressing.

Self-healing tests of Surlyn/NR and Surlyn/LaB<sub>6</sub> composites as well as Surlyn/EPDM cross-linked DCP with NRs were carried out under the action of NIR radiation. A comparison was made of the effectiveness of healing processes using various types of energy supply to self-healing compositions. The effectiveness of healing with photothermal heating in a short period of time of small scratches and bigger damages with a distortion of the original shape of the sample has been proven.

---

## 4.4. Supporting information

### Materials

Ethylene propylene rubber (EPDM) and Surlyn PC2000 were used as obtained. Dicumyl peroxide (DCP) (Sigma Aldrich, 98%) was used without further purification. Polysulfone granulate (PSU, Ultrason® S 2010 NAT) was provided by BASF. Toluene (> 99.8%), Butanol-1 (> 99.8%), hexane (> 99.8%), dichloromethane (DCM, > 99.8%), methanol (MeOH, > 99.8%), and ethanol (EtOH, > 99.8%) were purchased from VWR. Tetrachloro-gold (III) acid trihydrate ( $\text{HAuCl}_4 \cdot 3\text{H}_2\text{O}$ , >99.9 %), silver nitrate ( $\text{AgNO}_3$ , 99.9999 %), cetyltrimethylammonium bromide (CTAB, >99 %), L-ascorbic acid, hydroquinone (> 99 %), tri-base sodium citrate dihydrate (> 99 %), and sodium borohydride ( $\text{NaBH}_4$ , > 99 %) were purchased from Sigma-Aldrich and used as obtained. Thiol-functionalized polyethylene glycols with different end groups (HS-PEG-R) were purchased from the following companies: HS-PEG-0.8K-OMe with  $M_n = 0.8$  kDa and HS-PEG-6K-OMe with  $M_n = 6$  kDa from Sigma-Aldrich, HS-PEG-3K-OH with  $M_n = 3$  kDa and HS-PEG-10K-COOH with  $M_n = 10$  kDa were purchased from Iris Biotech. Phenylboronic acid ( $\text{PhB(OH)}_2$ , 95%) was purchased from Sigma-Aldrich or TCI Chemicals and stored in the refrigerator before use. Commercially available lanthanum hexaboride obtained from plasma (plasma produced (PP)) or by milling (MP) ( $\text{LaB}_6$ , nanoscale) were obtained from Sindlhauser Materials GmbH. MP  $\text{LaB}_6$  was received as stabilized dispersion in iso-propanol. Only deionized water (DI) (18.2  $M\Omega \cdot \text{cm}$ , "PURELAB Plus", Veolia) was used for nanoparticle synthesis. Small gold nanoparticles (AuNPs) were synthesized as previously reported.<sup>48-50</sup> Stabilization of small AuNPs<sup>48</sup> with HS-PEG-OMe-0.8K was done as previously described for AuNRs. The desired concentration of AuNP-PEG-0.8K for further usage was obtained by

---

centrifugation and transfer to DCM. All glassware was thoroughly cleaned and stored in the oven before use.

## **Characterization methods**

### **Optical spectroscopy**

UV-Vis/BIC standard spectra were recorded on a commercial Jasco V-780 ST spectrophotometer in the range  $\lambda = 200\text{-}1600$  nm. Absorbance (Abs. in conventional units), transmittance (T in %) of the composite films were measured using a standard film holder and pure matrix polymer as a reference. All samples were characterized by a scanning speed of 1000 nm/min at an average response (data step = 1 nm). The spectra were evaluated using Jasco spectra management software (version 2).

### **Transmission electron microscopy**

First, thin slices of the composite films were prepared using an ultramicrotome (type: Powertome XL, RMC Boekeler) equipped with a 45° diamond disk. The layer thickness was set to 70 nm. TEM microphotographs of thin film sections were obtained with a Carl Zeiss Libra 120 microscope equipped with an in-column energy filter at an electron beam accelerating voltage of 120 kV.

### **Scanning electron microscopy**

Scanning electron microscopy (SEM) was performed with a Hitachi S3000 N (Hitachi, Japan) with acceleration voltage of 5kV and an amperage of  $\sim 60\mu\text{A}$ . To improve the conductivity a 5 nm layer of gold/palladium (60:40) was sputter coated on the samples, using an ACE 600 sputter coater (Leica, Germany). Image

---

analysis was performed with ImageJ analysis software. Fluorescence microscopy was performed with a Zeiss Axioplan 2 (Zeiss, Germany).

### **Fluorescence Microscopy**

The core-sphere transition temperature for AuNR composites was determined using a Zeiss Axioplan 2 microscope equipped with an AxioCam ICc 3. A thin slice of the PSU-AuNRs@PEG-0.8K composite film was pretreated at 80 °C in a vacuum at 10 mbar for 24 hours. The film was then fixed between two thin slides and heated from 25 °C to 300 °C using a Mettler Toledo FP82HT slide connected to a Mettler Toledo FP 90 central processor. The transition was determined optically by the colour change of the composites after a 2-min equilibration at the corresponding temperature.

### **Photothermal heating of polymer/NP composites**

The thermal imaging measurements were taken using a FLIR<sup>®</sup> A655Sc at a frame rate of 6.25 fps. The sample was placed on a peltier heating stage which was temperature controlled with an accuracy of  $T = 20 \pm 0.1$  °C. The thermal imaging camera was placed directly above the sample. As a laser source, a near infrared (NIR) laser ( $\lambda = 808$  nm, 8 W, continuous wave (cw), Roithner Lasertechnik) was used. The laser was incident on the sample from the top at an angle of approximately 45 degrees with an ellipsoidal beam footprint of 0.49 mm<sup>2</sup>. The output power was previously calibrated with an optical power meter (PM200, Thorlabs) and set to  $P = 86$  mW at pulsed irradiation with 1 ms on-phase and 15 ms off-phase. The produced data was extracted from the native FLIR<sup>®</sup> software and analyzed using ImageJ (V1.52d).

Furthermore, a FLIR<sup>®</sup> ‘One Pro’ smartphone adapter (for iOS) was used in combination with a suitable smartphone to visualize the thermal color map of irradiated PSU-AuNR composites. For this purpose, the respective composite

---

materials were irradiated from the bottom with a NIR LED light source ( $\lambda = 850 \text{ nm}$ ,  $P_{\text{max}} = 16 \text{ W}$ ).

### **Mechanical Tensile Tests**

Mechanical tests were performed on an Instron 5982 testing machine at room temperature with 50 mm/min deformation rate (cold deformation). Samples were either stretched until breakage or strained to an extension of  $\varepsilon = (l - l_0)/l_0$  of 300%.

### **Healing tests**

A razor blade was used to introduce a dent 0.2 mm deep into Surlyn PC2000/NP composite films (1×1 cm, thickness  $\approx 2 \text{ mm}$ ) or to cut through EPDM/Surlyn PC2000/DCP/NP (2×1 cm, thickness  $\approx 2 \text{ mm}$ ) sample. Then the samples were heated for a short time using a self-made NIR LED cluster for photothermal heating ( $\lambda = 850 \text{ nm}$ ,  $P = 1.6 \text{ W}$ ). A thermal infrared imaging camera FLIR<sup>®</sup> A655Sc was used to detect the temperature variation of the crack surface. The microscopy images of the cracks were taken with a scanning electron microscope (Hitachi S3000 N).

## **Sample preparation**

### **Synthesis of nanoparticles and preparation of stabilized dispersions**

#### **Synthesis of AuNR**

AuNRs were synthesized according to the previously described seed-mediated growth method<sup>48-50</sup> with slight modifications as described below.

---

**Growth solution (I).**  $\text{HAuCl}_4\cdot 3\text{H}_2\text{O}$  solution (50 mL, 0.003 M) and deionized water (100 mL) were added to an Erlenmeyer flask equipped with a stirrer. This mixture was then heated to 25 °C in a water bath and stirred. After a couple of minutes, CTAB (150 mL, 0.2 μM) was carefully added to avoid foaming. To the dark amber solution, 1-Ascorbic acid (3.1 mL, 0.05 M) and  $\text{AgNO}_3$  (3.3 mL, 0.008 M) were added successively with a delay of 10 min. After adding 1-ascorbic acid dropwise, the solution was discoloured. This solution was then further stirred and maintained at a constant temperature of 25 °C.

**Initial solution (II).** Deionized water (4.2 mL), CTAB (5 mL, 0.2 M) and  $\text{HAuCl}_4\cdot 3\text{H}_2\text{O}$  (830 μL, 0.003 M) were added to a sealed vial and gently stirred. A freshly prepared and ice-cooled  $\text{NaBH}_4$  solution (600 μL, 0.01 M) was quickly added under vigorous stirring and incubated at high stirring speed for 2 min. The solution immediately turned brownish. The solution was then stirred gently for another 5 min and left for about 15 min before use.

**AuNR Synthesis.** With vigorous stirring, 875 μL of (II) was added to 2 mL of (I) and left at a high stirring speed for 5 min. Then the stirring speed was reduced to low and left like this for ≈30 min. 1-Ascorbic acid (2 mL, 0.05 M) was slowly added to the slightly red solution using a syringe pump ( $V = 0.5 \text{ mL}\cdot\text{h}^{-1}$ ). After the complete addition of 1-ascorbic acid, the solution was stirred for another 30 min until the synthesis was complete. Fresh CTAB-stabilized AuNRs were centrifuged at 9500 rpm for 25 min, concentrated to 20 mL ( $C_{\text{Ac}} = 1.5 \text{ mg/mL}$ ), and passed through a polyethylene terephthalate (PET) filter ( $d_p = 1.2 \text{ }\mu\text{m}$ ) before use.

### PEG-stabilized AuNRs

The standard procedure for AuNR functionalization with PEG is as follows: a freshly prepared aqueous dispersion of AuNR-CTAB ( $V = 10 \text{ mL}$ ,  $c = 1.3 \text{ mg}\cdot\text{ml}^{-1}$ ) was treated with the appropriate HS-PEG-R (8 mg in 1 mL EtOH). Under

---

ultrasound for 30 min at 60 °C and then for 3.5 h at 20 °C, according to the procedure described in the literature<sup>50</sup> to obtain a final concentration of AuNRs ~ 3.25 mg·ml<sup>-1</sup>. The prepared dispersions were placed in sealed vials and stored in the refrigerator at 4 °C until further use.

### **PhB(OH)<sub>2</sub>-stabilized LaB<sub>6</sub>**

PhB(OH)<sub>2</sub>-LaB<sub>6</sub> dispersions were prepared by placing LaB<sub>6</sub> (10 mg) and PhB(OH)<sub>2</sub> (0.418 mmol) in DCM ( $V_{\text{DCM}} = 5 \text{ ml}$ ,  $C_{\text{LaB}_6} \sim 2 \text{ mg}\cdot\text{ml}^{-1}$ ). The mixture was sonicated for 6 h to produce a greenish-dark dispersion. The dispersion was placed in a sealed vial and stored at room temperature. The dispersion was treated briefly with ultrasound before use, since it shows sedimentation of the particles after a few days.

## **Preparation of composite materials with plasmonic nanoparticles**

### **Fabrication of freestanding PSU-NP composite films by solvent evaporation**

Briefly, PSU (1.67 g) was dissolved in DCM (6 mL) for 12 h. Afterwards, AuNR-PEG in DCM (0.5 mL, 0.097 wt%) or PhB(OH)<sub>2</sub>-LaB<sub>6</sub> in DCM (1 mL, ~ 0.1 wt%) were added and the dispersion was briefly homogenized. Afterwards, the dispersions were poured into a glass petri dish (inner diameter  $d = 55 \text{ mm}$ ), immediately covered with parafilm and left undisturbed overnight for at least 12 h. The respective freestanding PSU-NP composite films were then removed from the glass petri dish and a small piece ( $d = 15 \text{ mm}$ ,  $h \sim 1 \text{ mm}$ ) was blanked out for further characterizations.

### **Production of PSU-NP composite samples by hot pressing**

---

Briefly, PSU (1.67 g) was dissolved in DCM (6 mL) for 12 hours. Then, AuNP-PEG in DCM (0.5 mL, 0.097 wt%), PhB(OH)<sub>2</sub>-LaB<sub>6</sub> in DCM (1 mL, ~0.1 wt%) or stabilized MP LaB<sub>6</sub> in iso-propanol (1 mL, ~0.1 wt%) were added and the dispersion was briefly homogenized. To the dispersion of PSU-NP in DCM, 35 mL of additional DCM was added and stirred for 5 min ( $C \approx 3$  wt%). Obtained solution was added dropwise to cold methanol under vigorous stirring. The resulting powder was subjected to vacuum filtration and dried overnight under vacuum at 60 °C. From the dried composite, discs with a diameter of 25 mm and a thickness of 1-2 mm were moulded using a temperature-controlled vacuum press (MeltPrep GmbH, Graz, Austria). The normal procedure included shaping the sample for 15 min at 240 °C and 1.7 bar.

### **Production of Surlyn PC2000-NP or Surlyn PC2000/EPDM/DCP-NP composite films by hot pressing**

At 65 °C, 14 g of Surlyn PC2000 was dissolved in 380 ml of a mixture of butanol-1 and toluene (1: 9). Then AuNR-PEG in DCM (3.5 mL, 0.097 wt%) or MP LaB<sub>6</sub> in isopropanol (7 mL, ~0.1 wt%) was added and the dispersion was briefly homogenized. To obtain a crosslinked polymer blend, 6 g of EPDM in 40 ml of the same solvent mixture was added to Surlyn PC2000 to obtain a clear solution of ~ 5% wt. Additionally 30 mg of dicumyl peroxide (0.5 wt% of EPDM) was added to the 70/30 Ionomer-EPDM mixture. Then, like in case of pure Surlyn composites, AuNR-PEG in DCM (5 mL, 0.097 wt%) or MP LaB<sub>6</sub> in isopropanol (10 mL, ~0.1 wt%) were added and the dispersion was briefly homogenized. The warm solutions of Surlyn PC2000-NP or Surlyn PC2000/EPDM/DCP-NP were then slowly added to 1.5 L of cold methanol containing 15% water. The coprecipitated composites were separated by vacuum filtration and dried at 60 °C under vacuum for 20 h.

---

The dried coprecipitated powder was moulded into discs 25 mm in diameter and 1.7 mm thickness using a temperature-controlled vacuum press (MeltPrep GmbH, Gratz, Austria). To prepare larger samples, a P200S-VAK press (Vogt Labormaschinen GmbH, Berlin, Germany) was used. The moulding process was performed at 110 °C for 1 h. For samples containing a crosslinking agent, the temperature was raised to 190 °C for 20 min to ensure crosslinking before cooling to room temperature. Samples of 10×10 cm with a thickness of 0.7 mm were obtained.

---

## 4.5. Acknowledgements

Prof. Martin Möller gratefully acknowledges the support of an Advanced Grant from the European Research Council (ERC), Jellyclock 695716. This work was performed in collaboration with the Center for Chemical Polymer Technology CPT, which is supported by the EU and the federal state of North Rhine-Westphalia (grant EFRE 30 00883 02). We want to thank Volkan Yavuz (Sindlhauser Materials), who kindly provided the LaB<sub>6</sub>.

### Contributions to the Chapter

Oliver Jung and Ben Schmidt helped with the photothermal heating experiments. Alexander Nedilko performed the advanced optical spectroscopy. Stefan Hauk, Sven Buschmann and Michelle Maaßen supported with characterization experiments and preparation of composites. Friedrich Meder and Immanuel Georgius helped with the syntheses and characterization of plasmonic NPs. Prof. Dr. Martin Möller and Prof. Dr. Andrij Pich supervised this project.

---

## 4.6. References

- [1] Hanemann, T. & Szabó, D. V. *Materials* (2010).
- [2] Tanaka, T., Montanari, G. C. & Mülhaupt, R. in *IEEE Transactions on Dielectrics and Electrical Insulation* (2004).
- [3] Wang, Q. & Zhu, L. *Journal of Polymer Science, Part B: Polymer Physics* (2011).
- [4] Dang, Z. M., Yuan, J. K., Zha, J. W., *et al.* *Progress in Materials Science* (2012).
- [5] Laschewsky, A. *Polymers* (2014).
- [6] Althues, H., Henle, J. & Kaskel, S. *Chem. Soc. Rev.* **2007**.
- [7] Vijaya Sarathy, K. & Narayan, K. S. *Curr. Sci.* **1999**.
- [8] Ko, J., Kim, Y. J. & Kim, Y. S. *ACS Appl. Mater. Interfaces* **2016**.
- [9] Tan, Y. J., Wu, J., Li, H. & Tee, B. C. K. *ACS Applied Materials and Interfaces* (2018).
- [10] Wang, Z., Liang, H., Yang, H., *et al.* *Prog. Org. Coatings* 137, 105282 **2019**.
- [11] Wu, D. Y., Meure, S. & Solomon, D. *Progress in Polymer Science (Oxford)* (2008).
- [12] Kanu, N. J., Gupta, E., Vates, U. K. & Singh, G. K. *Composites Part A: Applied Science and Manufacturing* (2019).
- [13] Yang, Y. & Urban, M. W. *Chem. Soc. Rev.* **2013**.
- [14] Amendola, V., Pilot, R., Frascioni, M., Maragò, O. M. & Iatì, M. A. *Journal of Physics Condensed Matter* (2017).
- [15] Chen, H., Shao, L., Li, Q. & Wang, J. *Chem. Soc. Rev.* 42, 2679–2724 **2013**.
- [16] Ye, X., Zheng, C., Chen, J., Gao, Y. & Murray, C. B. *Nano Lett.* **2013**.
- [17] Jiang, N., Zhuo, X. & Wang, J. *Chemical Reviews* (2018).
- [18] Govorov, A. O. & Richardson, H. H. *Nano Today* (2007).
- [19] Balazs, A. C., Emrick, T. & Russell, T. P. *Science* (2006).
- [20] Hore, M. J. A. & Composto, R. J. *Macromolecules* (2014).
- [21] Thorkelsson, K., Bai, P. & Xu, T. *Nano Today* (2015).
- [22] Jain, P. K., Huang, X., El-Sayed, I. H. & El-Sayed, M. A. *Acc. Chem. Res.* **2008**.
- [23] Kim, J. H. & Lee, T. R. *Drug Dev. Res.* **2006**.
- [24] Hribar, K. C., Lee, M. H., Lee, D. & Burdick, J. A. *ACS Nano* **2011**.
- [25] Zhang, Z., Wang, J., Nie, X., *et al.* *J. Am. Chem. Soc.* **2014**.
- [26] Joseph Fortenbaugh, R. & Lear, B. J. *Nanoscale* **2017**.
- [27] Viswanath, V., Maity, S., Bochinski, J. R., Clarke, L. I. & Gorga, R. E. *Macromolecules* **2013**.
- [28] Cho, Y. J., Kong, L., Islam, R., *et al.* *Nanoscale* 12, 20726–20736 **2020**.
- [29] Behl, M., Razzaq, M. Y. & Lendlein, A. *Advanced Materials* (2010).
- [30] Leng, J., Lan, X., Liu, Y. & Du, S. *Progress in Materials Science* (2011).
- [31] Hribar, K. C., Metter, R. B., Ifkovits, J. L., Troxler, T. & Burdick, J. A. *Small* **2009**.
- [32] Xiao, Z., Wu, Q., Luo, S., *et al.* *Part. Part. Syst. Charact.* **2013**.
- [33] Le, D. M., Tycon, M. A., Fecko, C. J. & Ashby, V. S. *J. Appl. Polym. Sci.* **2013**.
- [34] Leonardi, A. B., Puig, J., Antonacci, J., *et al.* *Eur. Polym. J.* **2015**.
- [35] Yao, Y., Hoang, P. T. & Liu, T. *J. Mater. Sci. Technol.* **2017**.
- [36] Lu, X., Zhang, H., Fei, G., *et al.* *Adv. Mater.* **2018**.
- [37] Zhang, H., Xia, H. & Zhao, Y. *J. Mater. Chem.* **2012**.
- [38] Zhang, H., Zhang, J., Tong, X., Ma, D. & Zhao, Y. *Macromol. Rapid Commun.* **2013**.
- [39] Haes, A. J., Haynes, C. L., McFarland, A. D., *et al.* *MRS Bulletin* (2005).
- [40] Leng, J. S., Lu, H., Liu, Y. J., Huang, W. M. & Du, S. Y. *MRS Bull.* **34**, 848–855 **2009**.
- [41] Setoura, K., Werner, D. & Hashimoto, S. *J. Phys. Chem. C* **2012**.
- [42] Petrova, H., Juste, J. P., Pastoriza-Santos, I., *et al.* *Phys. Chem. Chem. Phys.* **2006**.
- [43] Link, S. & El-Sayed, M. A. *International Reviews in Physical Chemistry* (2000).

- 
- [44] Link, S., Burda, C., Mohamed, M. B., Nikoobakht, B. & El-Sayed, M. A. *Journal of Physical Chemistry A* (1999).
- [45] Schweizerhof, S. Selective surface modification of gold nanorods with functional polymers for tunable self-assembly and optical properties, Möller, M, Richtering, W. **2020**.
- [46] Taylor, A. B., Siddiquee, A. M. & Chon, J. W. M. *ACS Nano* **2014**.
- [47] Zou, R., Zhang, Q., Zhao, Q., *et al.* *Colloids Surfaces A Physicochem. Eng. Asp.* **2010**.
- [48] Jana, N. R., Gearheart, L. & Murphy, C. J. *Langmuir* **2001**.
- [49] Keul, H. A., Möller, M. & Bockstaller, M. R. *Langmuir* **2007**.
- [50] Schweizerhof, S., Demco, D. E., Mourran, A., *et al.* *Macromol. Chem. Phys.* **2017**.

---

# 5. METAL FIBRE-FILLED COMPOSITE MATERIALS

## 5.1. Introduction

Polymers exhibit many great properties, including high specific strength, great chemical stability, electrical insulating characteristics and a good processability. In addition polymers are comparably inexpensive materials.<sup>1</sup> They have been therefore widely used in the electronics, medicinal, energy, and manufacturing industries for decades. However, polymeric matrices suffer from a poor intrinsic thermal conductivity and are insufficiently thermally stable, thus limiting its further application in fields requiring strong heat dissipation and low thermal expansion.<sup>1</sup> Linear thermoplastics and thermosets are two key kinds of polymers utilised in advanced polymer composite industries.

Polymer composites are sophisticated materials that are an alternative to traditional materials like metals or ceramics. They are made up of at least two parts of distinct phases, one of which is the continuous polymeric matrix phase and the other comprises the reinforcements (fibers, filler). Tensile/impact strength, stiffness, wear resistance, thermal conductivity, corrosion resistance and fatigue life are all increased in polymer composites.<sup>2</sup>

Nanocomposites containing magnetic particles, which possess inherent magnetic characteristics, have gained a lot of interest among the various nanomaterials employed in industrial, environmental, and biological applications. These composites have the potential to be used as anticancer materials, magnetic resonance imaging,<sup>3,4</sup> magnetic recoverable catalysts,<sup>5,6</sup> hyperthermia therapy,<sup>7,8</sup> bio-separation,<sup>9,10</sup> and magnetorheological materials.<sup>11</sup>

---

However, the inherent instability of magnetic nanoparticle dispersions in a continuous phase over extended periods of time is a pressing issue that must be solved in order to facilitate the usage of magnetic nanocomposite in a variety of different applications. Magnetic nanoparticles tend to agglomerate in order to reduce the energy by reducing the amount of surface area.<sup>12</sup> Furthermore, because pure magnetic metal nanoparticles are extremely reactive in air and are readily oxidised, their magnetic characteristics may be lost with time. Here, the utilization of magnetic metal fibres in polymer composites serves as a great alternative for many different applications.

The lifespan and strength of polymers and polymer composites for structural uses are equally difficult to achieve.<sup>13</sup> Polymeric materials can deteriorate in the presence of a harsh environment, such as heat and mechanical stress, resulting in the production of microcracks. If microcracks remain unnoticed, they can lead to catastrophic failures. We require tools and strategies for early damage detection and restoration.<sup>14</sup> It is preferable that materials have the ability to heal themselves<sup>15</sup> since it is difficult to detect and fix damages deep within the material. The term "self-healing materials" refers to materials which can repair damage, such as cracks, and return to or near-restore its previous state while still functioning as intended. Self-healing materials improve the material's safety and durability.<sup>16</sup>

In construction applications, functional polymers are popular due to high production capacity, resistance to corrosion, and good electrical conduction.<sup>17</sup> Polymers can vary in their electrical conductivity based on the nature and connectivity of their fillers, which is measured using the percolation theory. As the percolation threshold of a polymer increases, its conductivity also increases.<sup>18</sup> Fillers such as carbon nanotubes, graphite, carbon black, metal and carbon fibres can improve the electrical conductivity of polymer composites.<sup>19</sup>

---

Electromagnetic interference shielding (EMI) is a technique used to prevent the interference of electromagnetic signals in electrical and electronic equipment. Originally made from metal, EMI shielding components have gained popularity in recent years due to their ability to conduct electricity. In comparison to metals, these composites offer every one of the metals advantages while being far more affordable. The most important quality to look for is its shielding effectiveness (SE).<sup>20</sup>

Improvements in electrical conductivity and EMI SE are the consequence of decreased electrical resistance. When an electrically conductive composite is added to a self-healing polymer matrix, the damaged conductivity is restored. After some time, the EMI protection function will activate again.<sup>21</sup>

In this work, conductive metal fibres with a length of several millimeters were chosen as filler for the polymer matrix. The high specific surface area of the conductive rods provides a high amount of scattering centres and, therefore, a high number of internal reflections. Due to the low metal content, the composite is lightweight and effectively dissipates heat energy resulting from the absorption of electromagnetic waves. In the case of self-healing composites, the shielding will initiate the healing of a damage by non-invasive heating through electromagnetic absorption.

When an alternating magnetic field is applied to the composite, electromotive forces are generated in the material, creating eddy currents in form of many closed rings in the composite material. These circular eddy currents create secondary magnetic fields that displace the main field and prevent it from penetrating deep into the metal fibres. The shielding effect of eddy currents increases with a higher field frequency and a higher eddy current strength (Figure 1).

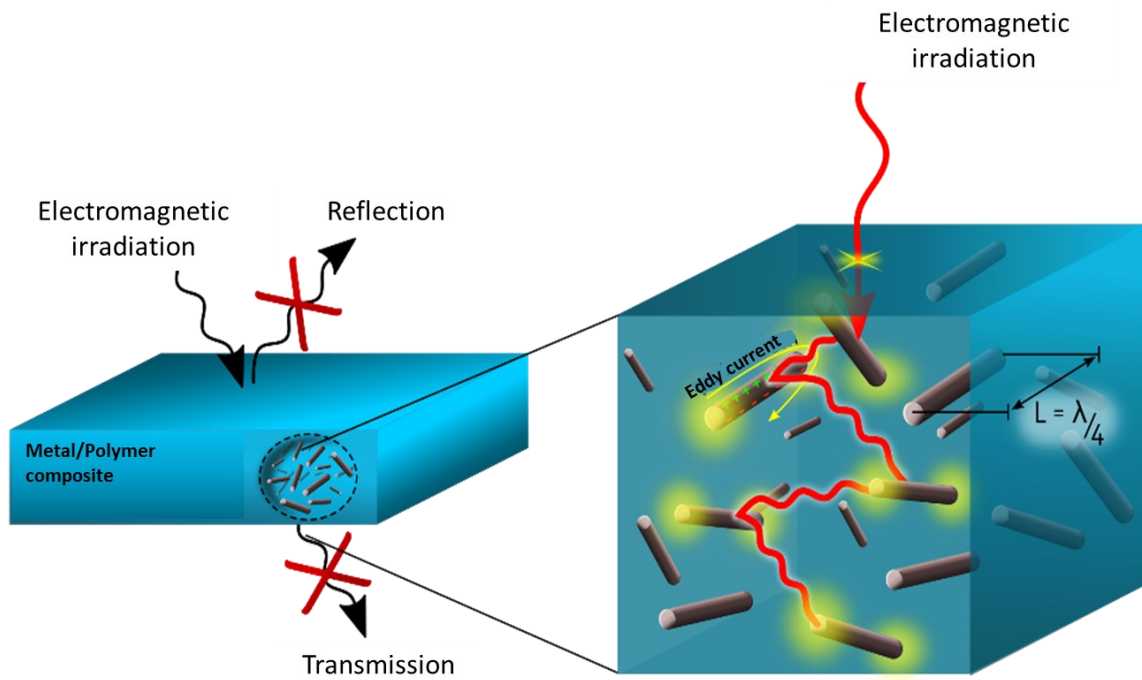
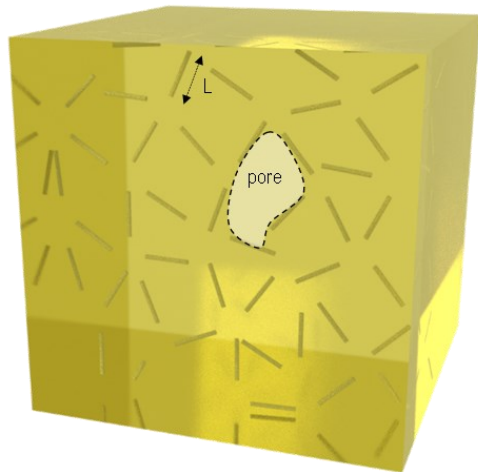


**Figure 1.** Shielding mechanism by multiple internal reflections

To effectively absorb electromagnetic radiation, the composite material must meet the following conditions: (i) the fibre length is greater than the wavelength divided by 4, (ii) the mesh size is in the 100  $\mu\text{m}$  range and has high conductivity in the radiation frequency range. These conditions are met if the metallic fibres are less than 5  $\mu\text{m}$  in diameter, a few millimeters in length and their distribution is homogeneous within the polymer matrix (Figure 2). Compared to the technical standard, where fine silver particles are introduced in high concentration into the polymer matrix (e.g. polyamide, polyacrylonitrile, Surlyn), fibre composites with fibre fillers have the advantage of a much lower percolation threshold (long-range bond formation in random systems) and a higher polymer content. The low concentration and high mechanical flexibility of the filler are important prerequisites for miniaturization of the shielding material.



Fiber length  $> 0.2-2 \text{ mm } (\lambda/4)$   
Fiber diameter  $< 10 \text{ }\mu\text{m}$   
 $100 \text{ }\mu\text{m} < \text{Pore size} < 1 \text{ mm } (\lambda/10)$

**Figure 2.** Requirements for composite materials for effective absorption of electromagnetic radiation.

Induction heating is a fast and convenient method of triggering self-healing properties in polymer composites. Induction heating (IH) is a non-invasive heating technology based on the induction of an alternating magnetic field in the medium to be heated.<sup>22</sup> When an object is placed in this field, two heating effects occur: hysteresis losses and eddy current losses. The first effect appears only in ferromagnetic materials, such as iron, nickel and cobalt, due to friction between the particles, when the material is continuously magnetized in different directions. This phenomenon is due to the motion of the near-wall domains, which prevail during high-frequency excitation or heating of ferromagnetic nano/microparticles. The higher frequency of magnetic oscillations leads to faster movement of the particles, which causes more friction and, therefore, more heat. The second effect is Joule heating, which occurs in any conductive material due to electric currents induced by a fluctuating magnetic field. Both effects lead to heating of the processed object, however Joule heating is generally the main source of heat in IH processes.

Herein, we describe self-healing ionomer (Surlyn PC2000) and metal fibres (CuSi<sub>4</sub> or Vitrovac) composites preparation by extrusion with subsequent injection moulding or hot pressing. Those materials can be used for EMI applications due to their ability for multiple reflections of absorbed

---

electromagnetic radiation. In contrast to conventional heating methods like flames and traditional furnace heating; induction, microwave, or irradiation heating provide rapid, clean, and accurate temperature regulation through a non-contact and effective approach. Materials that absorb more incident radiation can also be used for shielding electronic equipment and in stealth technology.<sup>23,24</sup>

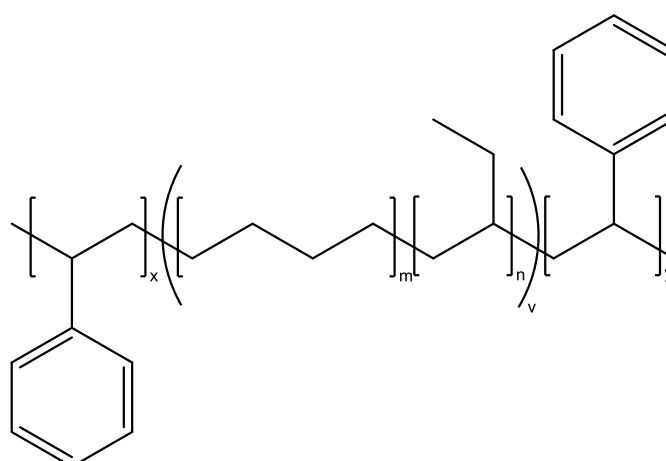
---

## 5.2. Results and discussion

### 5.2.1. Composite materials based on polymer matrices and fibre fillers of different chemical nature.

In this study, styrene-ethylene-butadiene-styrene (SEBS) or Surlyn PC2000 ionomer composites containing  $\text{CuSi}_4$  or Vitrovac (composition  $\text{Co}_{69}\text{Fe}_4\text{Mo}_3(\text{Nb},\text{Si},\text{B})_{\text{rest}}$ ) magnetic fibres, produced by horizontal spinning from the melt, were prepared.

The thermoplastic styrene elastomers SEBS is two-phase block copolymer with hard and soft segments (Scheme 1). The styrene end blocks provide thermoplastic properties and the butadiene intermediate blocks provide elastomeric properties. SEBS is a hydrogenated thermoplastic styrene elastomer with excellent mechanical properties, chemical and heat resistance, and is produced by hydrogenation of styrene and butadiene block copolymers.<sup>25</sup> SEBS-based composites have excellent elastomeric properties and a rubber-like appearance as well as excellent resistance to weathering, UV radiation and ozone, making them an ideal choice for outdoor applications with a long service life.



**Scheme 1.** Chemical Structure of SEBS.

---

SEBS is commercially available as a granulate and yields a strong material with high flexibility after thermal moulding or solution casting. The use of this polymer made it possible to determine the effective concentrations of the fibre filler to achieve effective heating under electromagnetic radiation, as well as the evaluation of the corrosion resistance.

SEBS/CuSi<sub>4</sub> composites (fibre content of 2.5, 5, 10, 20, 30, and 50 wt%) were prepared by extrusion of the matrix polymer with the metal fibres. A twin-screw microcompounder was used to mix the initial components, after which the resulting composite was extruded in filament form and pelleted.

The pelletized composite obtained by extrusion was then moulded by hot pressing into specimens 25 mm in diameter and 1.6 mm thick under pressure of 1.7 bar and temperature of 180 °C for 10 min. To prepare larger samples, a P200S-VAK press was used. In this case, the pressing was also carried out at the matrix polymer forming temperature (from 110 to 190 °C) and pressure of 30-50 bar for 20 min. To ensure a homogeneous fibres distribution, a hot-pressing method was developed to achieve uniform distribution of the fibre filler in the matrix polymer. For this purpose, the resulting granulate was moulded into 0.7 mm thick films by hot pressing, then divided into four equal parts and pressed again. The operation was repeated two more times until the optimal distribution of the metal fibres was achieved.

An alternative method of processing is injection moulding into specimens with an estimated length of 60 mm, width of 20 mm and thickness of 2 mm. Samples obtained by all methods are shown in Figure 3.

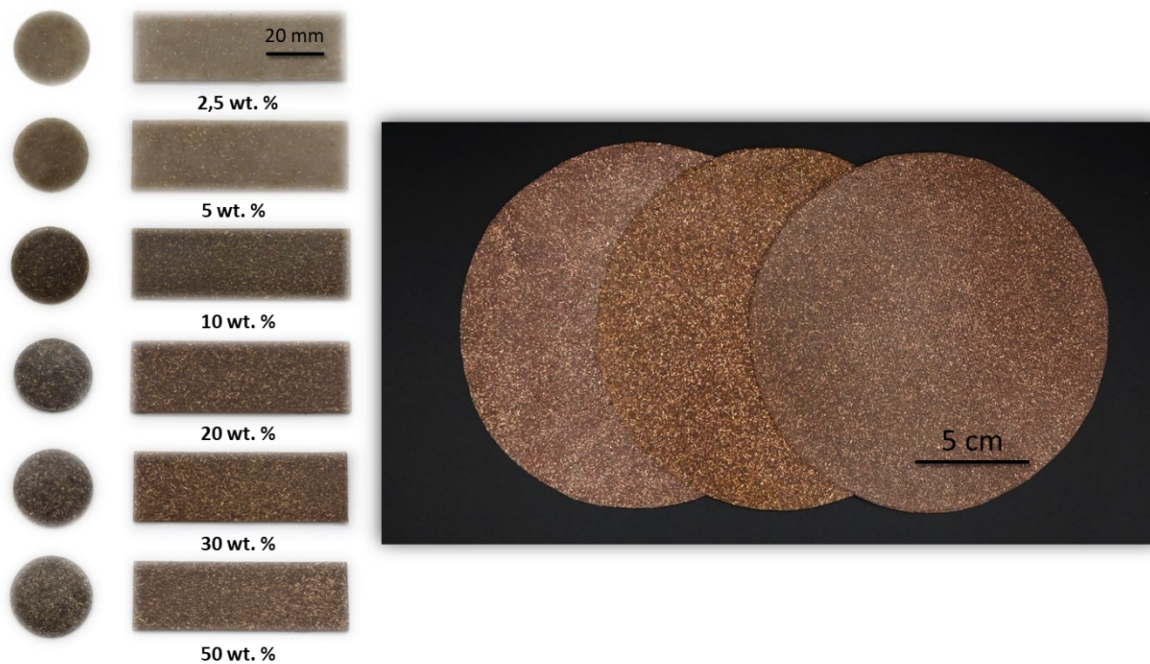


**Figure 3.** SEBS/CuSi<sub>4</sub> composites with different metal fibre content moulded by hot pressing or injection moulding from extruded granulate.

Surlyn PC2000/Metal fibres composites were prepared using a previously established technique by extrusion of the matrix polymer with pre-cut CuSi<sub>4</sub> fibres. The pelletized composite obtained by extrusion was then moulded by hot pressing (8 × 8 cm and 1.6 mm thick under pressure of 30 bar and temperature of 190 °C for 20 min) or by injection moulding (length of 60 mm, width of 20 mm and thickness of 2 mm). Samples obtained by this method are shown in Figure 4.

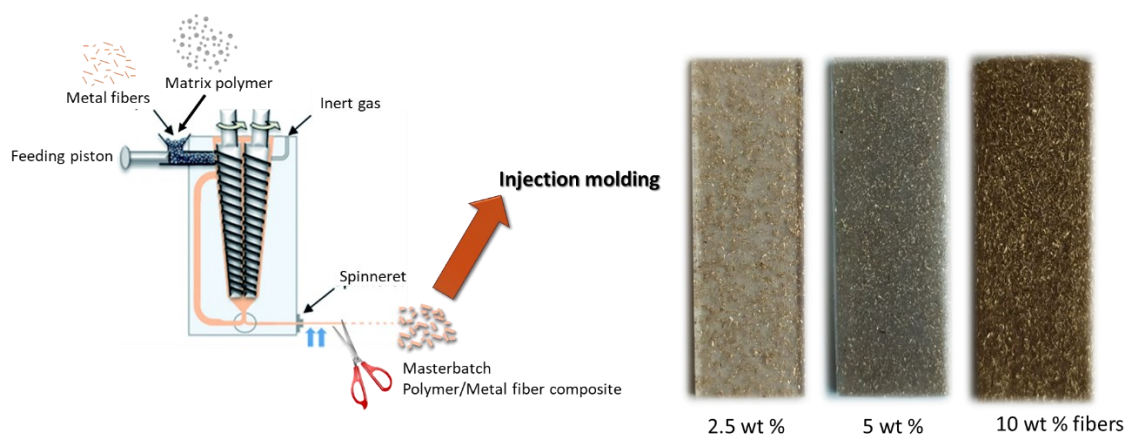


**Figure 4.** Surlyn PC2000/CuSi<sub>4</sub> composites with different concentrations of fibre filler produced by injection moulding.

Composites based on Surlyn PC2000 self-healing polymer and Vitrovac magnetic fibres (Co-Fe-B-Si-Ni-Nb) were also prepared by extrusion. Surlyn PC2000 and pre-cut Vitrovac ( $l \approx 2$  mm) were loaded into the microcompounder in a 95/5 or 75/25 ratio at a cylinder temperature of 200 °C in a nitrogen atmosphere. The resulting composite was then extruded in filament form, pelletized and moulded by hot pressing into 1.6 mm thick samples (Figure 5).

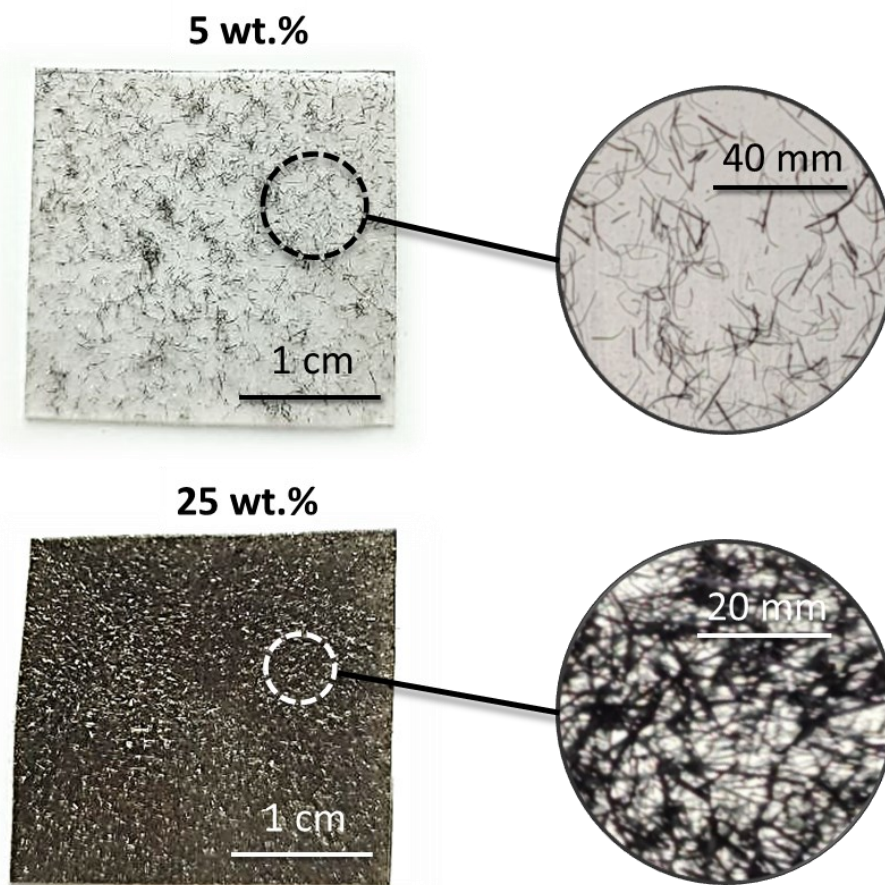


**Figure 5.** Obtained Surlyn/Vitrovac composites and optical images of the samples with light passing through.

### 5.2.2. Determination of effective concentrations and properties of the obtained samples

It was determined that the obtained samples had uniformly distributed metallic fibres with pore sizes of around 500  $\mu\text{m}$  between them (according to computer microtomography, Figure 6).

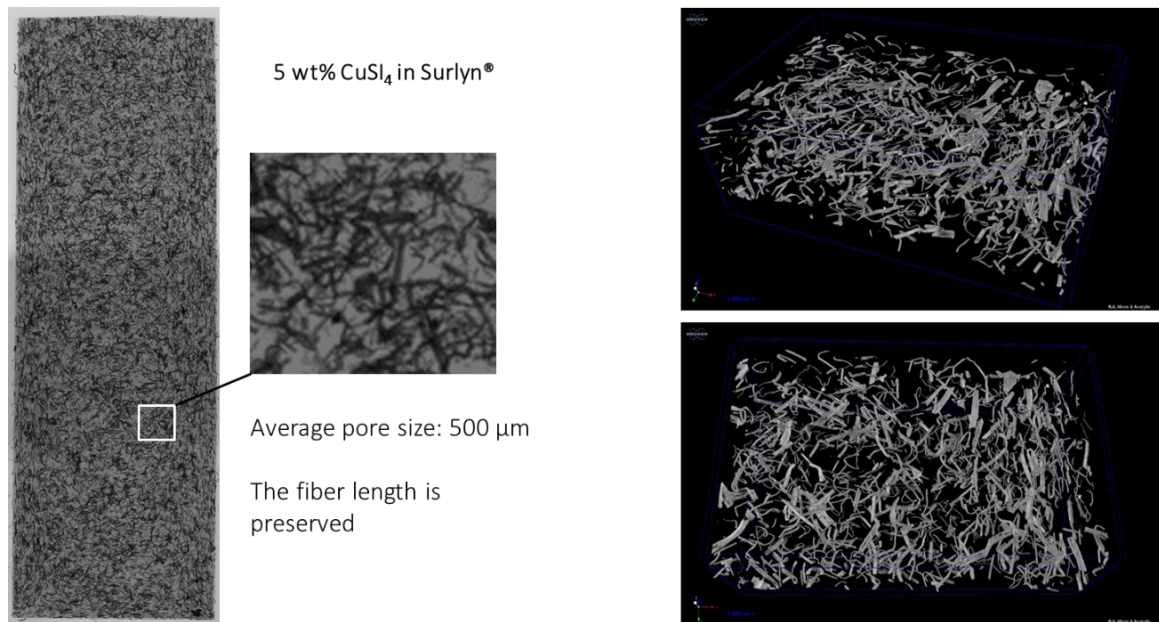


**Figure 6.** computer microtomography of Surlyn PC2000/ $\text{CuSi}_4$  samples obtained by injection moulding with 5 wt% concentration of copper fibres.

Additionally, micro CT scans of the Surlyn PC2000 samples obtained by hot pressing with different  $\text{CuSi}_4$  fibres content were made (Figure 7). It is evident that a homogeneous fibre distribution can be achieved with various concentrations of the metal filler.

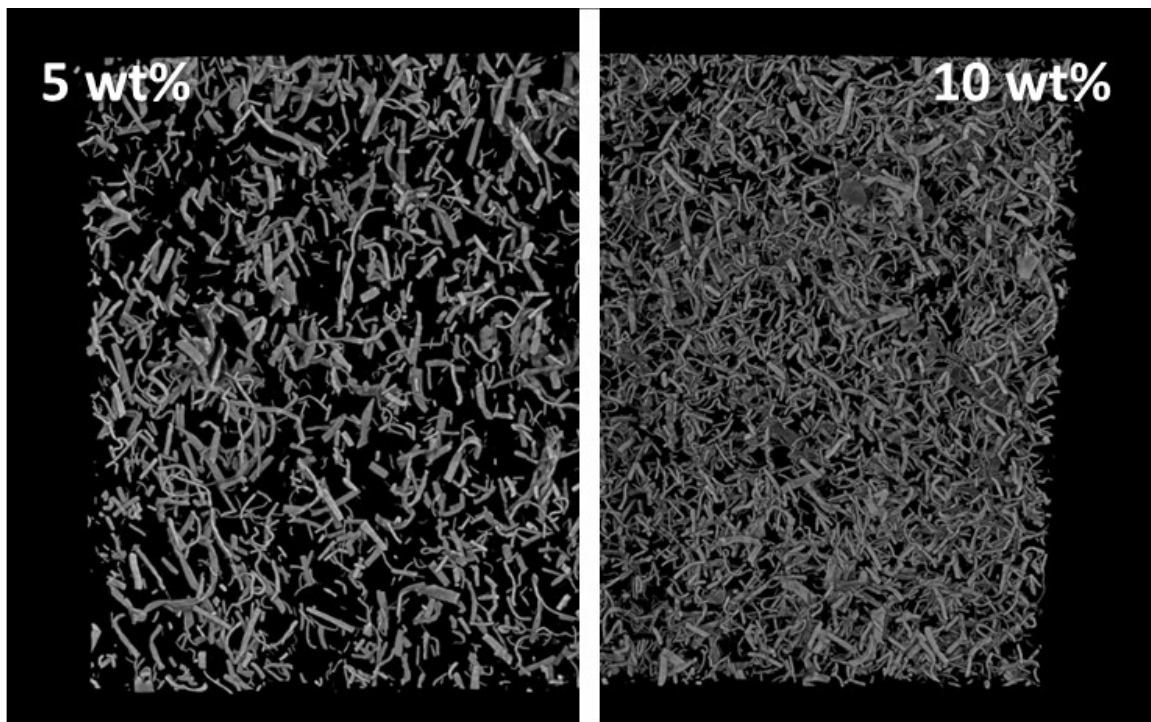


**Figure 7.** Computer microtomography of Surlyn PC2000/CuSi<sub>4</sub> samples obtained by hot pressing with 5 and 10 wt% concentration of copper fibres.

Electrical conductivity in an insulating polymer is achieved at a fibre concentration close to reaching the percolation threshold, at which there is an abrupt change in the electrical properties of the composite. To determine this percolation fibre concentration, electrical impedance measurements were performed.

The impedance in the range of 1 Hz - 8 MHz with an amplitude of 20 mV was measured across the thickness of the samples using a homemade measuring cell with disc electrodes made of stainless steel and  $D = 18$  mm. A 25  $\mu\text{m}$  thick Kapton film was placed on one of the electrodes as a dielectric barrier to eliminate the possibility of one highly conductive path in the material short-circuiting the electrodes. The results for the SEBS/CuSi<sub>4</sub> samples obtained by hot pressing (one time pressing) and injection moulding are shown in Figure 8 and 9, respectively.

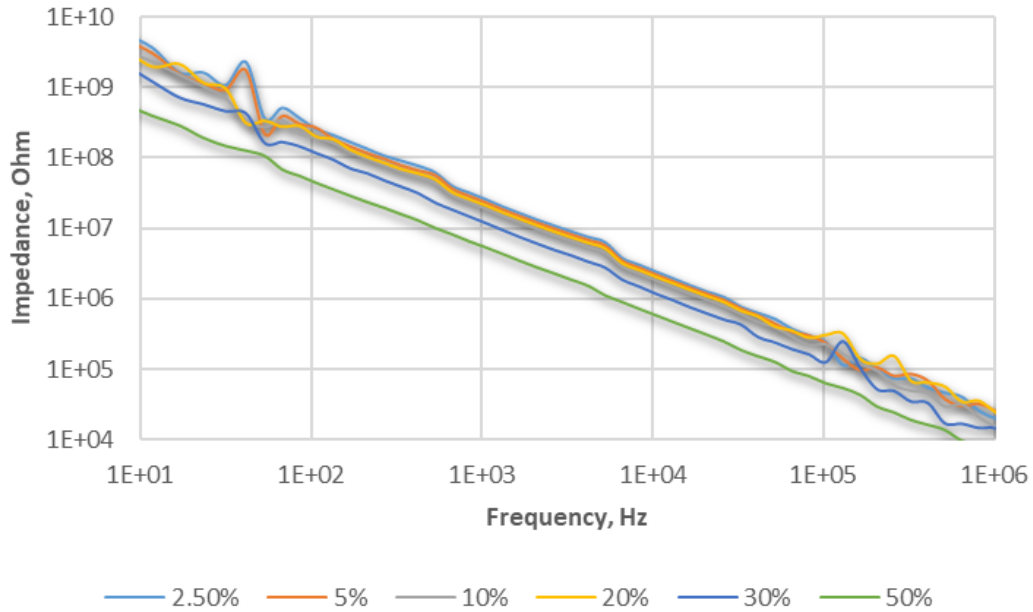


**Figure 8.** Impedance measurements of SEBS/CuSi<sub>4</sub> composites (fibre content 2.5, 5, 10, 20, 30 and 50 wt%) obtained by hot pressing.

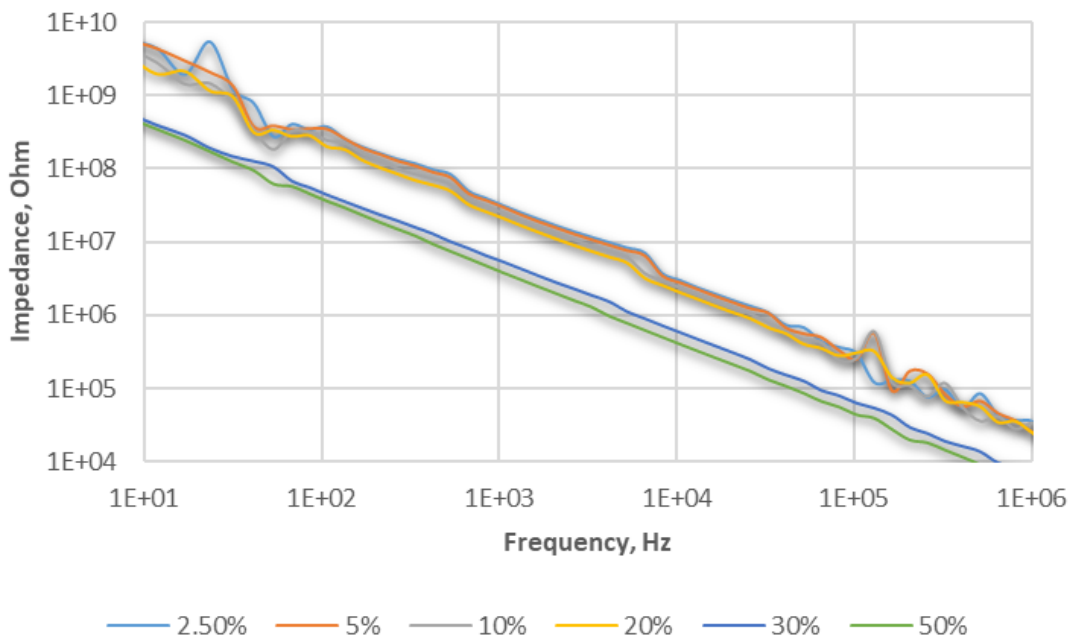


**Figure 9.** Impedance measurements of SEBS/CuSi<sub>4</sub> composites (fibre content 2.5, 5, 10, 20, 30 and 50 wt%) obtained by injection moulding.

Figures 8 and 9 show that the percolation threshold for injection moulded SEBS/CuSi<sub>4</sub> composites is observed with a content of 20 to 30 wt% metal fibres. For SEBS/CuSi<sub>4</sub> composites obtained by hot pressing, this threshold also lies

between 20 and 30 wt% of metallic fibres, but it is not as sharp, which can be explained by the lower homogeneity of the once hot-pressed samples compared to those obtained by injection moulding.

For the DC electrical conductivity study, 5 samples (10, 20, 30, 40, and 50 wt% fibre content) were prepared by mixing Surlyn PC2000 ethylene methacrylic acid ionomer and CuSi<sub>4</sub> fibres in a dry state followed by single hot pressing moulding into 25 mm diameter and 1 mm thick specimens.

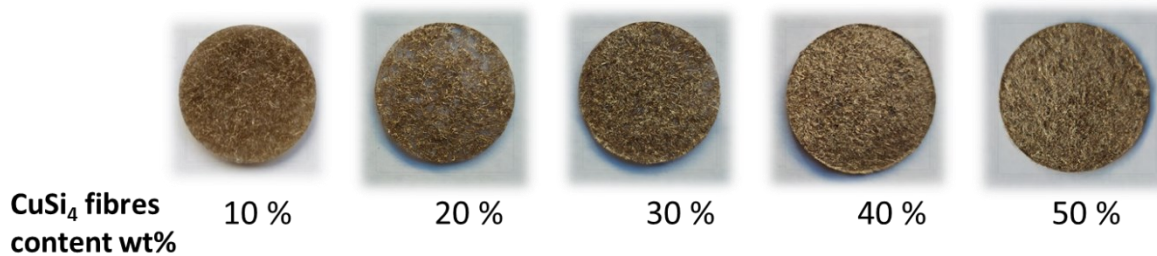
Electrical resistance was measured using a method with two points with a distance of 20 mm and the conductivity was calculated using the equation 1.

$$\sigma = \frac{\pi \cdot D \cdot t}{4 \cdot L \cdot R} \quad (1)$$

Here,  $R$  is the electrical resistance of a uniform specimen of the material,  $D$  is sample diameter,  $t$  – thickness and  $L$  – separation distance between electrodes. And conductivity,  $\sigma$ , is the inverse of resistivity. Figure 10 shows that the percolation threshold for this composite is between 20 and 30 wt% fibre content, which correlates with previous impedance measurements.

**Table 1:** DC conductivity measurements for Surlyn PC2000 ionomer/metal fibre composites

Fibre percentage in the sample	Measured Resistance ( $R$ , [M $\Omega$ ])	Conductivity ( $\sigma$ )	$\log_{10}(\sigma)$
10%	34	$2.8 \times 10^{-8}$ S/m	-7.54
20%	53	$1.9 \times 10^{-8}$ S/m	-7.73
30%	0.09	$1.12 \times 10^{-2}$ S/m	-1.95
40%	0.016	0.06 S/m	-1.2
50%	0.014	0.07 S/m	-1.14



## 2-electrodes electrical resistance measurements

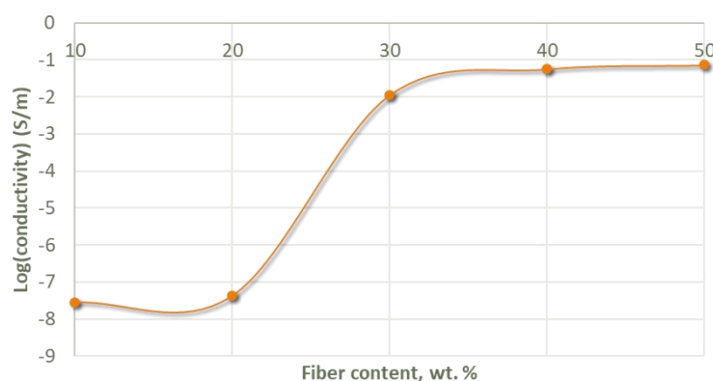


**Figure 10.** DC conductivity measurements for Surlyn PC2000 ionomer/metal fibre composites.

To assess the corrosion resistance of the obtained composites, the samples were kept in a 5 % aqueous solution of NaCl for 7 days at 50 °C. After treatment, no pitting, general corrosion or oxidation of the CuSi<sub>4</sub> fibres was visually observed. A comparison of the obtained composites before and after the corrosion resistance test is shown in Figure 11 (the composites with 2.5 and 50 wt% CuSi<sub>4</sub> fibres were chosen as examples). The samples were weighed before and after aging in water and the total water absorption was evaluated, which ranged from 0.2 to 0.5 wt%, indicating a high hydration resistance of the polymer composite.

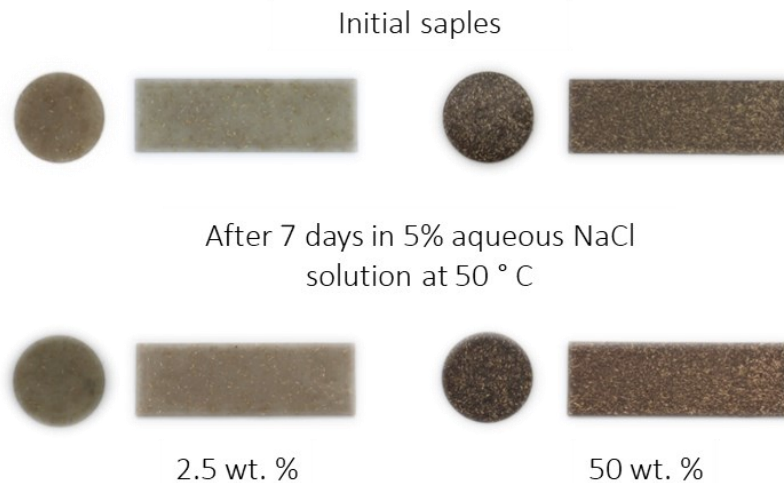


**Figure 11.** Composites SEBS/CuSi<sub>4</sub> with different content of metal fibres moulded by hot pressing or injection moulding from the extrusion granulate before and after exposure in 5% aqueous NaCl solution for 7 days at 50 °C.

Impedance measurements before and after the corrosion resistance test are shown in Figures 12 and 13. It is visible that the percolation threshold for SEBS/CuSi<sub>4</sub> composites remains between 30 and 20 wt% metal fibre content after soaking in water. The changes in frequency dependence of impedance are minimal and can be explained by method error.

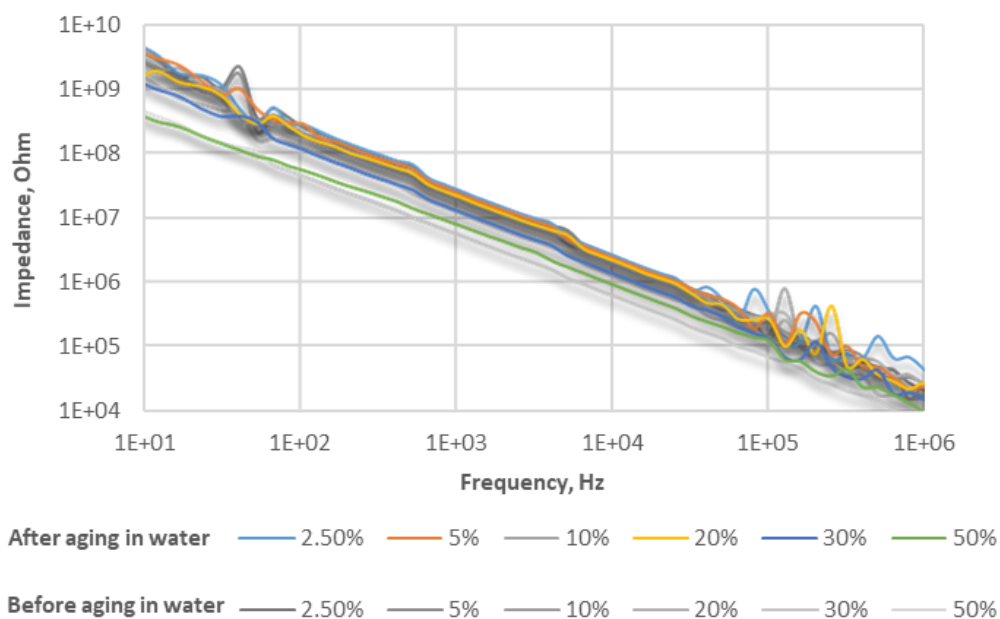


**Figure 12.** Impedance measurements of SEBS/CuSi<sub>4</sub> composites (fibre content 2.5, 5, 10, 20, 30 and 50 wt%) obtained by hot pressing after corrosion resistance test.

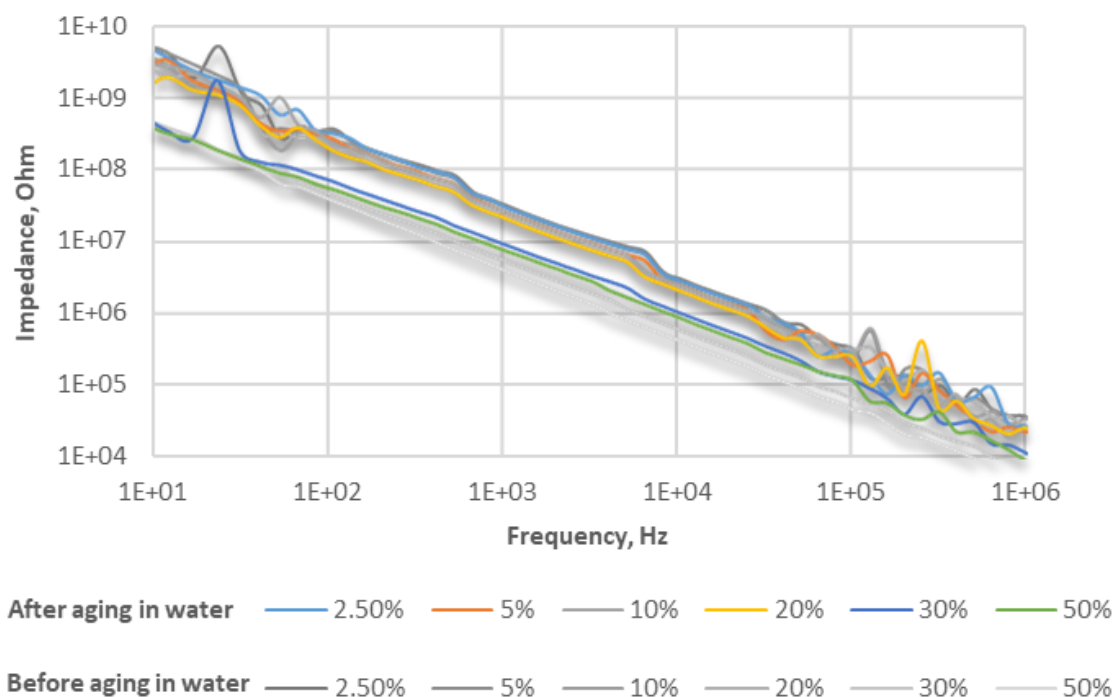


**Figure 13.** Impedance measurements of SEBS/CuSi<sub>4</sub> composites (2.5, 5, 10, 20, 30 and 50 wt% fibre content) obtained by hot pressing after corrosion resistance test.

### 5.2.3 Internal heating of polymer composites containing metal fibres and their self-healing properties

We investigated the efficiency of heating processes by using different type of electromagnetic energy input to self-healing compositions in form of induction. Self-healing tests of Surlyn PC2000/Vitrovac composites under the action of electromagnetic induction were carried out.

Heating experiments were carried out before the self-healing tests in alternating electromagnetic fields. Figure 14 illustrates the setup used for induction heating as well as thermal-coloured maps and measured temperatures for pure Surlyn PC2000 and its composites with Vitrovac magnetic fibres (5 and 10 wt%) 10 sec after beginning of the exposure with identical generator outputs ( $f = 1202$  kHz,  $P = 40$  %). The heat release during irradiation was monitored with a high-speed

thermal imaging camera and the corresponding temperature profiles were recorded (Figure 14).

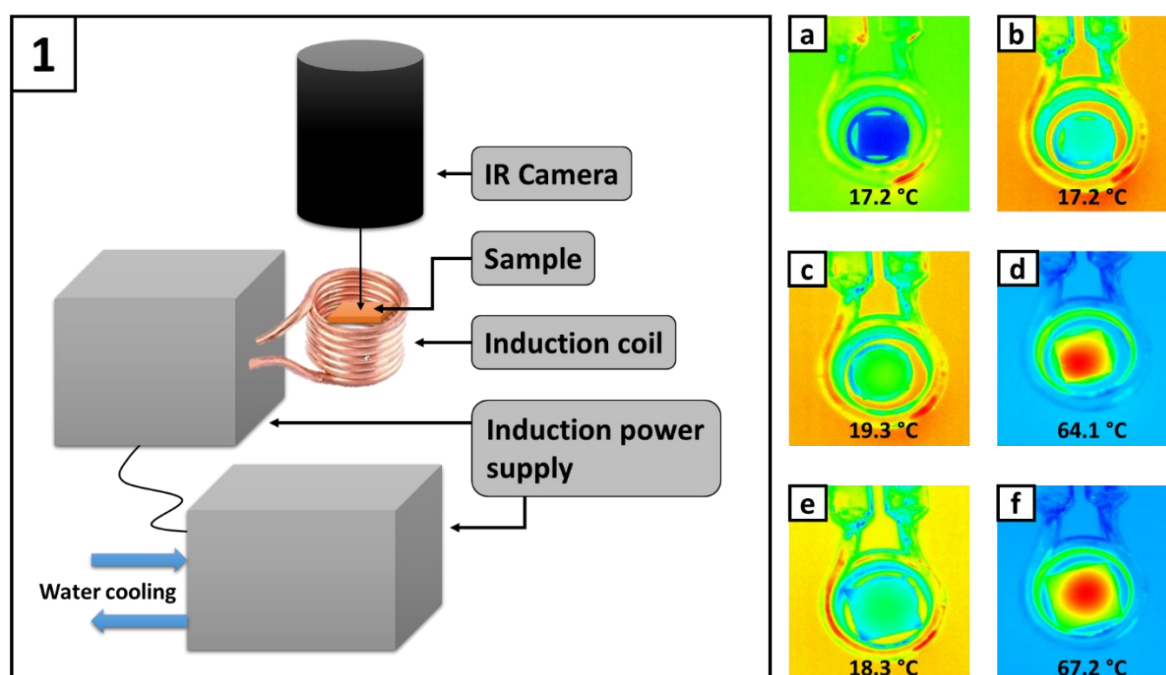


**Figure 14.** (1) Induction heating setup for heating of Surlyn PC2000/Vitrovac composites. Thermal colour map and corresponding temperature before (left) and after (right) exposure of pure Surlyn PC2000 (a, b) and its composites with Vitrovac fibres: 5 wt% (c, d) and 10 wt% (e, f).

As expected, the sample with pure Surlyn PC2000 shows no heating response under induction. However, when composite samples were irradiated using identical parameters, a rapid temperature increase was observed (average  $\Delta T = \sim 47$  °C). As would be predicted, the heating effectiveness increases along with the metal fibres content. For 5 wt% Vitrovac content temperature of the sample raises from 19.3 till 64.1 °C ( $\Delta T = 44.8$  °C), as for 10 wt% fibres  $\Delta T$  is equal 48.9 °C. The temperature stabilizes and an equilibrium is attained after 1 minute.

With an increase in applied power, a rapid rise in temperature is observed ( $> 120$  °C in 30 sec). However, successful healing occurs at the temperatures close to the melting temperature of the matrix polymer ( $\approx 100$  °C).<sup>26</sup> A temperature of approximately 100 °C, which is used in oven and IR radiation self-healing tests,

is attained using the induction heating device at 40 % power and 3 min of irradiation (Figure 15).

In addition, the healing of small scratches on the surface of the Surlyn PC2000/Vitrovac composites during induction heating ( $f = 1202$  kHz,  $P = 40$  %) has been studied.

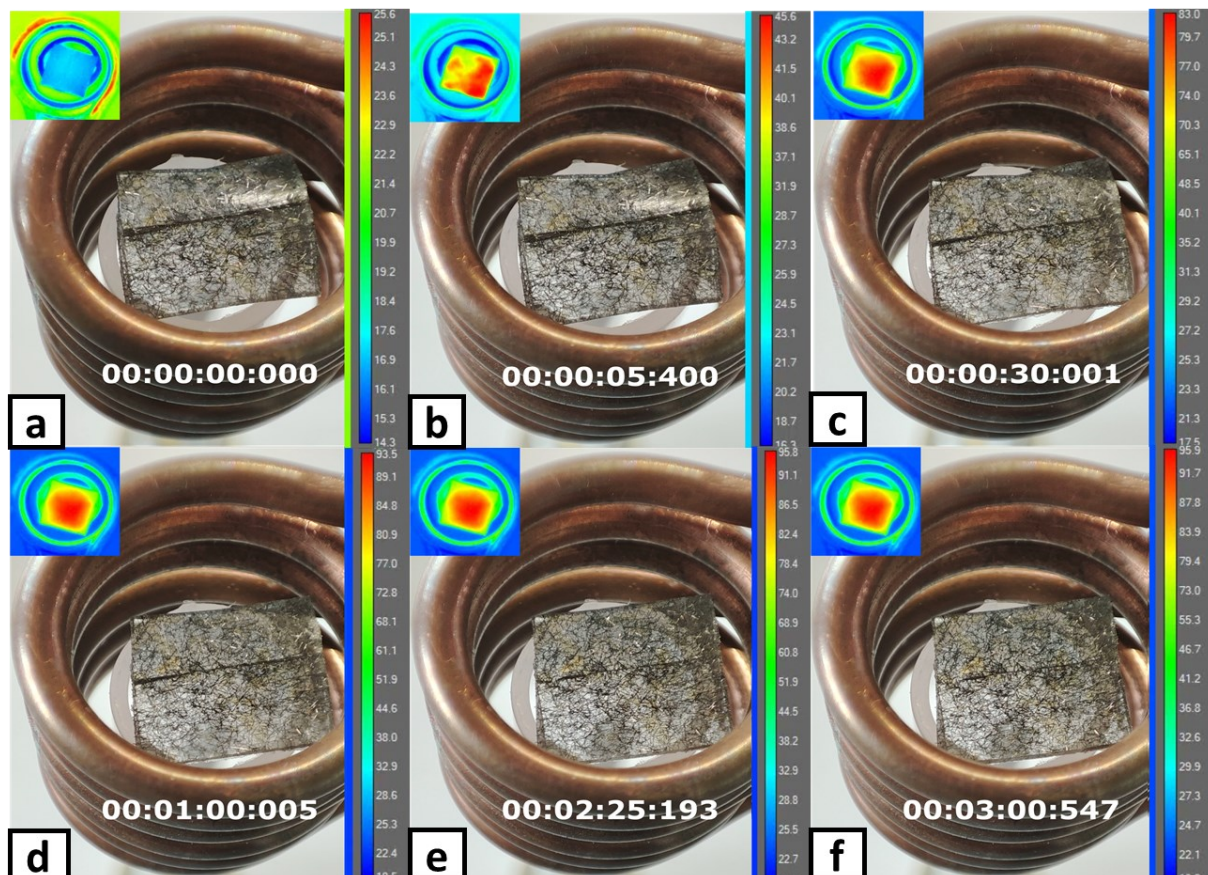


**Figure 15.** curing of shallow scratches on the surface of Surlyn PC2000/Vitrovac composite (5 wt%). Before inductive irradiation (a), after 5 s (b), 30 s (c), 1 (d), 2.25 (e) and 3 min (f).

Fine scratches 0.4 - 0.45 mm deep and 3 to 5 mm long were introduced to the surface of the composites with the help of a scalpel. After that, healing was performed during induction heating ( $f = 1202$  kHz,  $P = 40$  %) with a sample placed in the middle of the induction coil. Closure of the incisions was observed within 3 minutes after the start of the radiation. Figure 15 shows photographs of the Surlyn PC2000/Vitrovac sample with a fibre content of 5 wt% before the onset of induction (a). 5 seconds after the induction heating we initially observed an

inhomogeneous heat distribution with some overheated areas. (Figure 15b). However, after 30 seconds of irradiation, the temperature is visually homogeneous throughout the sample (Figure 15c). After 1 min, the temperature stabilizes and an equilibrium is attained ( $T \approx 93.5 \text{ }^\circ\text{C}$ ) (Figure 15d), while the closure of the incision is observed, and partially closed after 135 sec of irradiation (Figure 15e). The specimen was kept for an additional 35 seconds irradiated, reaching a temperature of  $95.9 \text{ }^\circ\text{C}$  (Figure 15f).

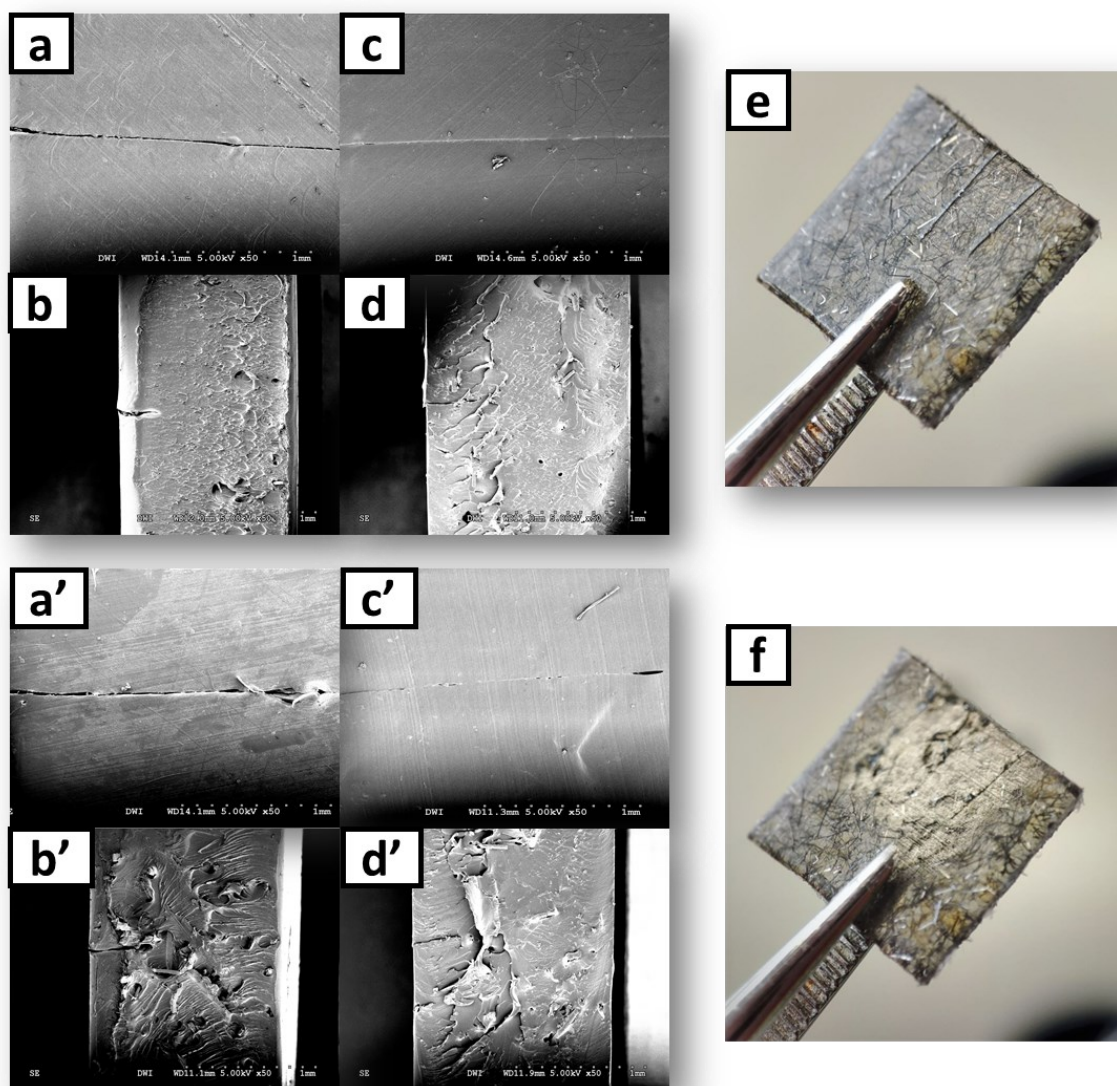


**Figure 16.** Study of healing process of Surlyn PC2000/Vitrovac (5 wt% fibres) (a-f) and Surlyn PC2000/Vitrovac (10 wt% fibres) (a'-d') composites under the influence of induction. Photographs of 10×10 mm sample (5 wt% fibres) before (e) and after (f) healing. Scanning electron microscopy of composites before (side view: b, b', top view: a, a') and after (side view: d, d', top view: c, c') damage healing.

---

Closure of the incisions was also recorded by scanning electron microscopy for both Surlyn PC2000/Vitroac 5 wt% and 10 wt% composites (Figure 16). As we can see from the microphotographs, cuts are still visible after healing, yet majorly reduced. Incompletion of the healing effect can be explained by inhomogeneities in heat distribution which can be reduced by increasing the diameter of the induction coil, or by reducing the size of incorporated metal fibres.

---

### 5.3. Conclusions

The production of composite materials based on Surlyn or SEBS polymers with CuSi<sub>4</sub> or Vitrovac fibres by extrusion followed by hot forming or injection moulding was studied. Hot pressing method was effectively improved by several cycles of pressing for better metal fibres distribution.

The effective concentrations and the percolation threshold of metal fibres were determined, and the high corrosion resistance of CuSi<sub>4</sub> in the resulting composite materials was shown.

The self-healing of the materials by induction heating in a short period of time was proven on the example of small surface scratches. Despite the incomplete healing of the cut after inductive heating, we observed major closing of the incision and a decrease of its visibility, which is sufficient for the surface restoration of the composite film, as well as prolonging of the service life of the product obtained from this type of material.

---

## 5.4. Supporting information

### Materials

The CuSi<sub>4</sub> fibres were produced by horizontal melt spinning and were kindly provided by Dr. Sebastian Weber and Louise Kaswurm, of the Max Planck Institute for Medical Research. The special alloys were produced by Wieland-Werke AG Vöhringen as raw materials. CuSi<sub>4</sub> stands for 4 wt% silicon in 96 wt% copper. The thickness and width of the fibres were determined by scanning electron microscopy (SEM). The fibres were cut to the desired/needed length using scissors.

The Vitrovac fibres were produced by vertical spinning from the melt and were kindly provided by Dr. Alexander Mikule (Max Planck Institute for Medical Research). Vitrovac is a specially developed material that forms an amorphous alloy when formed from the melt. Vitrovac alloy was provided by Vacuumschmelze GmbH & Co. KG Hanau with the nominal composition Co<sub>69</sub>Fe<sub>4</sub>Mo<sub>3</sub>(Nb,Si,B)<sub>rest</sub>.<sup>27</sup> The geometric dimensions were determined by SEM and the fibres were cut to the desired/needed length using scissors.

Surlyn PC2000s was used as received. Styrene-Ethylene-Butadiene-Styrene (SEBS) with a high butadiene fraction was provided by Freudenberg.

### Samples preparation

#### Typical procedure for the production of composites based on polymer matrix and metal fibres

A 15 mL twin-screw parallel rotation microcompounder with conical screws (DSM Xplore, The Netherlands) was used to produce polymer/metal fibre composites. The polymer matrix and pre-cut metal fibres (1 ~ 2 mm) were

---

simultaneously fed into the extruder at polymer processing temperature (210 to 230 °C). Mixing was carried out at a screw rotation speed of 40 rpm for 10 min in a nitrogen atmosphere. Then the obtained composites were either melted on a 5.5-mL casting machine (DSM Xplore) into samples with an estimated length of 60 mm, width of 20 mm and thickness of 2 mm under the following conditions: cylinder temperature 210 °C, mold temperature 60 °C, holding pressure 7 MPa, holding time 10 s, cooling time 20 s. Or the obtained extrudate was crushed and used for further moulding into discs with a diameter of 25 mm using a vacuum hot press with controlled temperature (MeltPrep GmbH, Gratz, Austria). Pressing was performed at the matrix polymer moulding temperature (from 110 to 190 °C) and pressure of 1.7 bar for 20 min. To prepare larger samples, a P200S-VAK press (Vogt Labormaschinen GmbH, Berlin, Germany) was used. In this case, the pressing was also carried out at the matrix polymer forming temperature (from 110 to 190 °C) and pressure of 30-50 bar for 20 min.

## **Characterization methods**

### **X-ray micro-CT**

Samples were imaged on a Bruker SkyScan 1272 high-resolution micro-CT (software version 1.1.19, Bruker microCT, Kontich, Belgium).

### **Electrical impedance**

Impedance in the range 1 Hz-8 MHz with an amplitude of 20 mV was measured using an electrochemical workstation IM6 (ZAHNER-elektrik GmbH & Co. KG). A home-made measuring cell with stainless steel disk electrodes  $D = 18$  mm was used for two-electrode impedance measurement along the thickness of the samples. As a dielectric barrier (DB), a 25  $\mu\text{m}$ -thick kapton film was placed on one of the electrodes to eliminate the situation when one highly conductive path in the material short-circuits the electrodes. The cell was connected to the IM6

---

with short cables from the IM6 kit; the IM6 was set to 4-electrode measurements to compensate for cable impedance.

### **Inductive heating**

To generate the external alternating magnetic fields either an high frequency generator 1997 1G 5/3000 or a TruHeat HF 5010, both from TRUMPF Hüttinger Elektronik GmbH + Co. KG (Freiburg, Germany) were used. Measurements were carried out with a 3-winded copper coil ( $d = 50$  mm) with water cooling at a constant frequency of  $f = 1202$  kHz and generator power  $P = 40$  % for the first system. Temperatures in the high frequency oven were measured with a Fotemp1 from Optocon (Dresden Germany) with a TS2 fiber optic temperature sensor. The whole sample is placed into the induction. Surlyn PC2000/Fibres composite films ( $1 \times 1$  cm, thickness  $\approx 2$  mm) were placed in the middle of the coil. An IR camera (FLIR<sup>®</sup> A655Sc) was used to record surface temperatures of the discs. The field heating was continued for 5 min, and results were averaged over three samples.

### **Scanning electron microscopy**

Scanning electron microscopy (SEM) was performed with a Hitachi S3000 N (Hitachi, Japan) with acceleration voltage of 5 kV and an amperage of  $\sim 60$   $\mu$ A. To improve the conductivity a 5 nm layer of gold/palladium (60:40) was sputter coated on the samples, using an ACE 600 sputter coater (Leica, Germany). Image analysis was performed with ImageJ analysis software. Fluorescence microscopy was performed with a Zeiss Axioplan 2 (Zeiss, Germany).

### **Healing tests**

A razor blade was used to introduce a dent 0.2 mm deep into Surlyn PC2000/NP composite films ( $1 \times 1$  cm, thickness  $\approx 2$  mm). Then the samples were heated for a short time using an induction power supply (power = 50 %). A thermal infrared

---

imaging camera FLIR<sup>®</sup> A655Sc was used to detect the temperature variation of the crack surface. The microscopy images of the cracks were taken with a scanning electron microscope (Hitachi S3000 N).

Two-point conductivity measurements were conducted using a Keithley 2400 SourceMeter (Keithley Instruments, USA) with an applied constant current of 1 mA. Discs samples with a diameter of 25 mm and thickness 1 mm were fabricated using a vacuum hot press with controlled temperature (MeltPrep GmbH, Gratz, Austria). Electrodes (1 mm diameter) were placed 20 mm apart on each sample. Measurements were performed at room temperature (25 °C), and the voltage drop across each sample was recorded. Conductivity was calculated using the formula  $\sigma = \frac{\pi \cdot D \cdot t}{4 \cdot L \cdot R}$ , where D is sample diameter, t – thickness and L – separation distance between electrodes.

---

## 5.5. Acknowledgements

This work was performed in collaboration with the Center for Chemical Polymer Technology CPT, which is supported by the EU and the federal state of North Rhine-Westphalia (grant EFRE 30 00883 02). We want to thank Dr. Sebastian Weber and Louise Kaswurm (Max Planck Institute for Medical Research), who kindly provided CuSi fibres. The Vitrovac fibres were kindly provided by Dr. Alexander Mikule (Max Planck Institute for Medical Research).

### Contributions to the Chapter

Stefan Herrmann helped with the induction heating experiments. Stefan Hauk, Rostislav Vinokur and Sven Buschmann supported with characterization experiments and preparation of composites. Karin Faensen performed micro CT measurements of the samples. Prof. Dr. Martin Möller and Prof. Dr. Joachim Spatz supervised this project.

Parts of this chapter were previously published as: **Selezneva E.V.**, Rahimi K., Rieder S., Spatz J., Möller M., Composite Material and Shielding Against Electromagnetic Radiation, U.S. Patent Application 20230292480, filed May 28, 2021, published September 14, 2023.

Some content has been adapted accordingly.

---

## 5.6. References

- [1] Zhang, R. H., Shi, X. T., Tang, L., *et al.* *Chinese J. Polym. Sci. (English Ed.)* **2020**.
- [2] Saba, N. & Jawaid, M. *J. Ind. Eng. Chem.* 67, 1–11 **2018**.
- [3] Lin, X. M. & Samia, A. C. S. *J. Magn. Magn. Mater.* **2006**.
- [4] Lin, N., Huang, J. & Dufresne, A. *Nanoscale* (2012).
- [5] Sorokin, V. V., Stepanov, G. V., Shamonin, M., *et al.* *Polymer (Guildf.)* **2015**.
- [6] Deng, L., Jia, W., Zheng, W., *et al.* *J. Ind. Eng. Chem.* **2018**.
- [7] Gorodov, V. V., Kostrov, S. A., Kamyshinskii, R. A., Kramarenko, E. Y. & Muzafarov, A. M. *Russ. Chem. Bull.* **2018**.
- [8] Arief, I. & Mukhopadhyay, P. K. *J. Magn. Magn. Mater.* **2017**.
- [9] Sun, C., Lee, J. S. H. & Zhang, M. *Advanced Drug Delivery Reviews* (2008).
- [10] Xie, Y., Kocaeffe, D., Chen, C. & Kocaeffe, Y. *Journal of Nanomaterials* (2016).
- [11] Adams, S. A., Hauser, J. L., Allen, A. C., *et al.* *ACS Appl. Nano Mater.* **2018**.
- [12] Lu, Q., Choi, K., Nam, J. Do & Choi, H. J. *Polymers (Basel)*. 13, 1–21 **2021**.
- [13] Eliasson, S., Berg, L. J. W., Wennhage, P., Hagnell, M. K. & Barsoum, Z. *Procedia Struct. Integr.* 38, 631–639 **2022**.
- [14] Kumar Banshiwal, J. & Nath Tripathi, D. *Funct. Mater.* **2019**.
- [15] Yuan, X. Y., Zou, L. L., Liao, C. C. & Dai, J. W. *Express Polym. Lett.* **2012**.
- [16] Wang, Y., Pham, D. T. & Ji, C. *Cogent Engineering* (2015).
- [17] Sandler, J. K. W., Kirk, J. E., Kinloch, I. A., Shaffer, M. S. P. & Windle, A. H. *Polymer (Guildf.)* **2003**.
- [18] Stauffer, D. & Aharony, A. *Introduction To Percolation Theory. Introduction To Percolation Theory* (2018).
- [19] Bilotti, E., Zhang, H., Deng, H., *et al.* *Compos. Sci. Technol.* **2013**.
- [20] Simon, R. M. *Polym. Plast. Technol. Eng.* **1981**.
- [21] Kenari, M. A. & Verma, D. *An introduction to self-healing of polymer composite materials and conventional repairing process. Sustainable Biopolymer Composites: Biocompatibility, Self-Healing, Modeling, Repair and Recyclability: A Volume in Woodhead Publishing Series in Composites Science and Engineering* (LTD, 2021).
- [22] Rudnev, V., Loveless, D. & Cook, R. L. *Handbook of Induction Heating, Second Edition. Boca Raton: CRC Press* (2018).
- [23] Abbas, S. M., Chandra, M., Verma, A., Chatterjee, R. & Goel, T. C. *Compos. Part A Appl. Sci. Manuf.* **2006**.
- [24] Gogoi, J. P., Bhattacharyya, N. S. & James Raju, K. C. *Compos. Part B Eng.* **2011**.
- [25] Wilkinson, P. J., Weaver, M. C., Kister, G. & Gill, P. P. *Propellants, Explos. Pyrotech.* **2022**.
- [26] Selezneva, E. V., Bakirov, A. V., Sedush, N. G., *et al.* *Macromolecules* **2021**.
- [27] Sekels GmbH, Broschüre Abschirmfolie VITROVAC 6025X. 2019.

---

## CONCLUSIONS

In conclusion, this doctoral thesis has provided a comprehensive examination of self-repair mechanisms within polymer composites. By strategically integrating diverse networks in the polymer material, we have successfully enabled autonomous healing processes driven by internal stress and activated through controlled temperature elevations. These temperature increases can be achieved through various means, including conventional heating, infrared irradiation, or induction.

The precise manipulation of temperature triggers has been achieved through the incorporation of different additives, such as nanoparticles and metal fibers, into the polymer matrix. Notably, even in the presence of considerable structural defects, our research has revealed a significant reduction or complete recovery of the damages.

Our investigations have shed light on the intricate dynamics of microscale healing, where ionic clusters undergo transformative reorganization during the heating and subsequent cooling phases. Furthermore, we have highlighted the pivotal role of crystallization in governing the material's relaxation behavior, with the promise of further improvement through tailored crystalline components and ionic aggregation within the polymer matrix.

In summary, this thesis presents a comprehensive exploration of how the varied bonding techniques and the strategic inclusion of specific additive components can substantially enhance the self-healing capabilities and overall durability of composite materials. These findings offer valuable insights into the advancement of materials science and engineering, with potential applications in numerous industries and technological domains.

---

# ACKNOWLEDGEMENTS

I would like to express my heartfelt gratitude to Prof. Dr. Martin Möller for his invaluable guidance and support throughout my PhD journey. His expertise and thoughtful mentorship have greatly enriched my research experience. The intriguing topic he provided, coupled with the freedom to explore it while offering his insightful counsel, has been fundamental to my growth as a scholar.

A big thanks also to Prof. Walter Richtering and Prof. Sonja Herres-Pawlis for being excellent co-examiners and to Prof. Jürgen Klankermayer for taking over the chair of the doctoral committee.

I am also deeply thankful to Xiaomin Zhu, Rostislav Vinokur, Khosrow Rahimi and Sjören Schweizerhof for their guidance and expertise, which have been instrumental during my thesis journey. Sincere thanks to Prof. Dan Demco, whose mentorship and assistance with crucial measurements have significantly contributed to my research and has been a rewarding and educational experience.

I extend my appreciation to the entire DWI Team for their support and assistance. Their collaborative spirit and willingness to help have played a vital role in my research endeavors.

I am grateful to my colleagues and lab mates - Philip, Ben, Sebastian, Denise, Onur, Oliver, Jan, Anton, Paskal, Maria, Milara, Deniz and Muen. Their camaraderie and shared passion for research have greatly enhanced my time in the lab and beyond. And a special word of thanks goes to Sebastian Weiß for his invaluable assistance in reviewing and refining this thesis! To my family – even when the world fell apart and we couldn't be together, your love and support reached me across every distance.

Finally, I must express my profound thanks to Alex – for being my anchor when things got overwhelming, my biggest cheerleader, and the heart I came home to at the end of every long day.

---

# RESUME

## PERSONAL INFORMATION

Elizaveta Selezneva  
Birthday: November 15, 1994  
Place of Birth: Moscow region  
Nationality: Russian

## Education

**2019 - 2022**

PhD, DWI Leibniz Institute For Interactive Materials  
Supervisor: Martin Möller

**2016 - 2018**

M.Sc. Polymer chemistry, MIREA - Russian Technological University  
GPA – 1.3

**2012 - 2016**

B.Sc. Polymer chemistry, MIREA - Russian Technological University  
GPA – 1.8

## Work experience

**2022 - present**

Chemist Product Developer, Adhesive technologies, Henkel | Düsseldorf, Germany

**2019 - 2022**

PhD student, DWI Leibniz Institute For Interactive Materials | Aachen, Germany

**2017 - 2019**

Researcher, Enikilopov Institute of Synthetic Polymeric Materials, Russian Academy of Sciences | Moscow, Russia

**2015 - 2017**

Student Researcher, Enikolopov Institute of Synthetic Polymeric Materials, Russian Academy of Sciences | Moscow, Russia

---

## Publications

**Selezneva E.V.**, Bakirov A.V., Sedush N.G., Bystrova A.V., Chvalun S.N., Demco D., Möller M., How Shape Memory Effects can Contribute to Improved Self-Healing Properties in Polymer Materials, *Macromolecules* **2021**, 54, 5, 2506–2517

**Selezneva E.V.**, Rahimi K., Rieder S., Spatz J., Möller M., Composite Material and Shielding Against Electromagnetic Radiation, U.S. Patent Application 20230292480, filed May 28, 2021, published September 14, 2023

**Selezneva E. V.**, Graf R., Bakirov A. V., Demco D. E., Chvalun S. N., Moeller M. Structure and Dynamics of Poly(Ethylene-Co Methacrylic Acid) Ionomer Blends with Rubbery EPDM. *Macromol. Rapid Commun.* **2023**, *Submitted*.

S. Schweizerhof, **E. Selezneva**, I. Georgius, M. Maaßen, M. v. Dongen, A. Mourran, A. Pich, M. Möller, “How to transcribe the enigma of the Lycurgus Cup to polymer films to earmark products against forgery”, **2023**, *in preparation*.

## Conference contribution

**Selezneva E.V.**, Bakirov A.V., Sedush N.G., Chvalun S.N., Demco D., Möller M., How Shape Memory Effects can Contribute to Improved Self-Healing Properties in Polymer Materials, *IUPAC-MACRO2020+ The 48th World Polymer Congress* May 16-20, **2021** Jeju, Korea